Max-Planck-Institut für Kolloid- und Grenzflächenforschung
Abteilung Kolloidchemie

Novel Surfactants for the Production of Functional Nanostructured Materials via the Ionic Self-Assembly (ISA) Route

**Neuartige Tenside für die Synthese Funktioneller
Nanostrukturierter Materialien durch
Ionische Selbsorganisation**

**Dissertation
zur Erlangung des akademischen Grades
"doctor rerum naturalium"
(Dr. rer. nat.)
in der Wissenschaftsdisziplin Physikalische Chemie**

**eingereicht an der
Mathematisch-Naturwissenschaftlichen Fakultät
der Universität Potsdam**

**von
Danielle Franke**
Geboren in Leeds, England, am 15. April, 1979

Potsdam, den 7. November 2005

A goal properly set is halfway reached

Abraham Lincoln (1809 - 1865)

TO MY PARENTS

ABSTRACT

In recent years, the aim of supramolecular syntheses is not only the creation of particular structures but also the introduction of specific functions in these supramolecules. The present work describes the use of the ionic self-assembly (ISA) route to generate nanostructured materials with integrated functionality. Since the ISA strategy has proved to be a facile method for the production of liquid-crystalline materials, we investigated the phase behaviour, physical properties and function of a variety of ISA materials comprising a perylene derivative as the employed oligoelectrolyte. Functionality was introduced into the materials through the use of functional surfactants.

In order to meet the requirements to produce functional ISA materials through the use of functional surfactants, we designed and synthesized pyrrole-derived monomers as surfactant building blocks. Owing to the presence of the pyrrole moiety, these surfactants are not only polymerizable but are also potentially conductive when polymerized. We adopted single-tailed and double-tailed N-substituted pyrrole monomers as target molecules. Since routine characterization analysis of the double-tailed pyrrole-containing surfactant indicated very interesting, complex phase behaviour, a comprehensive investigation of its interfacial properties and mesophase behavior was conducted. The synthesized pyrrole-derived surfactants were then employed in the synthesis of ISA complexes. The self-assembled materials were characterized and subsequently polymerized by both chemical and electrochemical methods. The changes in the structure and properties of the materials caused by the in-situ polymerization were addressed.

In the second part of this work, the motif investigated was a property rather than a function. Since chiral superstructures have obtained much attention during the last few years, we investigated the possibility of chiral ISA materials through the use of chiral surfactants. Thus, the work involved synthesis of novel chiral surfactants and their incorporation in ISA materials with the aim of obtaining ionically self-assembled chiral superstructures.

The results and insights presented here suggest that the presented synthesis strategy can be easily extended to incorporate any kind of charged tectonic unit with desired optical, electrical, or magnetic properties into supramolecular assemblies for practical applications.

Contents

1   INTRODUCTION

1.1   Supramolecular Chemistry: From Molecule to Material

In recent years, supramolecular chemistry has established itself as one of the most active fields of science and is becoming one of the primary frontiers of materials research.[1,2] The term 'supramolecular chemistry' was coined by Jean-Marie Lehn[3] and is the field where a variety of noncovalent forces and spatial fitting between molecular individuals play a role in the formation of the resulting materials (chemistry beyond the molecule). The characteristic feature is that molecules (hosts) are designed for their ability to interact with themselves or with target molecules (guests) to form large aggregates with well-defined structures, in which the individual components are connected through noncovalent bonds.

Thus, supramolecular chemistry allows the construction of large architectures of highly organized modules whilst minimising time-consuming covalent synthesis. Furthermore, since noncovalent bonds are formed spontaneously and reversibly under conditions of thermodynamic equilibrium, supramolecular systems have the in-built capability for error correction not normally available to fully covalent systems. In the search for supramolecular functional materials, the aim is that the molecular information encoded within the structure of the building blocks (also termed tectons), induces controlled organization. Ideally, specific functions should then be a direct result of the formed structure.[4,5] In order to achieve this goal, several noncovalent bonding strategies are available.

1.1.1   Noncovalent Bonding Strategies

The noncovalent bonding strategies available for the design and synthesis of supramolecular architectures include H-bonding,[6a] metal-coordination,[6b] charge-assisted H-bonding[6c] and Ionic Self-Assembly (ISA).[6d] The ionic self-assembly (ISA) process uses electrostatic interactions between charged surfactants and oppositely charged oligoelectrolytic species as the primary interaction. Other noncovalent interactions such as hydrogen-bonding, π-π and hydrophobic interactions can be utilized as secondary motifs to promote self-

organization.[7] This supramolecular approach, where ionic interactions act as the primary construction motif to assemble tectons into nanostructures, makes use of the strongest type of noncovalent interaction available. This allows for unambiguous stoichiometry and is in stark contrast to the hydrogen bonding approach where the resulting supramolecular assemblies are less well-defined.[8] The strong interactions involved in the ISA strategy, however, may be considered to be disadvantageous due to possible hindrance of the thermodynamic reversibility.

In the ISA process, binding between charged surfactants and oppositely charged tectons takes place though a highly cooperative process of charge neutralization.[7] This neutralization process (also called complex formation), well-known from polyelectrolyte-surfactant complexes,[9] occurs above the so-called critical aggregation concentration (cac), well below the critical micelle concentration (cmc) of the respective surfactant.[10] The van der Waals interactions contributed by the alkyl tails of the surfactants is found to be an important factor in ensuring phase separation on a molecular scale and thus, the formation of well-organized architectures (Figure 1).[11]
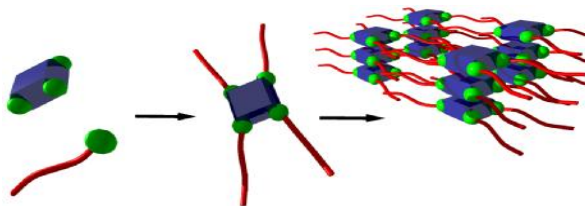
Figure 1: Schematic diagram of the ISA process involving charged surfactants and conjugated oligoelectrolytes. Due to the amphiphilicity of the surfactant, the π systems, ionic sites and hydrophobic tails are expected to demix into three subphases.

It has been found that a general trend exists for the influence of the surfactant structure (i.e. tail length, tail number and number of branches) on the properties of the resulting ISA materials.[11] Short single-tailed surfactants present a borderline case between a simple counterion-exchange process and the formation of supramolecular materials. An increase in the tail length of the surfactant leads to the formation of crystalline materials. Further increase in tail length and number leads to the formation of soft organized materials,

i.e. liquid-crystalline materials.[11] Both thermotropic[12,13,14] and lyotropic[13,15] liquid-crystalline ISA materials have been observed. Thus, owing to the wide range of charged tectons available, ISA presents a facile route for the production of an extensive variety of supramolecular materials. By careful choice of both moieties involved in complex formation, assemblies with widely varying material properties can be produced e.g. crystalline[7] and soft[11] (liquid-crystalline or amorphous) structures, or even organogels.[16] The use of functional moieties should also lead to functionality in the resulting material. Hence, one of the main attractive features of the ISA approach is that it is possible to add functionality into a nanostructured material in a very straightforward and facile manner.

1.1.2 Towards Functional Materials

In recent years, the aim of supramolecular syntheses is not only the creation of a particular structure but also the introduction of specific chemical functions in these supramolecules. Hydrogen-bonded nanotubes based on cyclic peptides composed of D α- and L α-amino acids, have shown in-vivo antibacterial efficiency.[5] This may well be related to the ability of these nanotubes to form transmembrane channels, increasing the permeability of the bacterial membrane. These nanotubes may also act as channels for K^+, Na^+, glucose or glutamate ions in lipid bilayer membranes, similar to naturally occurring channel-forming proteins. Functional hydrogen-bonded low molecular gelators based on a chiroptical switch have also been reported.[17] These materials allow for photocontrol of chirality on the molecular as well as the supramolecular level. Such structures should facilitate the design of 'smart' functional materials, which respond to external stimuli by subtle structural reorganization at the molecular level leading to significant changes in their macroscopic properties. Tunable chiral materials have also been observed for superstructures self-assembled through π-π interactions.[18] Since chiral superstructures have obtained much attention during the last few years, we have decided to investigate the possibility of chiral ISA materials through the use of chiral surfactants. Thus, this work involves synthesis of novel chiral surfactants and their incorporation in ISA materials with the aim of obtaining ionically self-assembled chiral superstructures.

Recent studies in the field of ISA have led to materials showing switchable,[14,19] luminescent[15] and reversibly switchable[19] conducting properties. In these studies, the oligoelectrolyte is responsible for the observed functionality. Thus, the surfactants typically employed are commercially available saturated hydrocarbon derivatives. The surfactants are used to direct self-organization through hydrophobic interactions and result in soft materials. Surfactants, however, may also act as "intelligent/functional" organic moieties within the materials. The use of functional surfactants in the synthesis of ISA materials has been investigated to a much lesser extent.[15,20]

In order to meet the requirements to produce functional materials through the use of functional surfactants, a double-tailed, unsaturated phosphate surfactant was employed to preserve the lamellar phase structure of a polyelectrolyte-surfmer complex through a dithiol-polyaddition strategy.[20] This surfactant, however, possesses no further functionality except for its ability to polymerize. Monomers that, after polymerisation, will yield conducting polymers, present a route to develop the concept of a combination of polymerisability and function in one step. This concept, together with supramolecular synthesis by ionic self-assembly, provides a strategy towards supramolecular functional materials. We have therefore designed and synthesized truly functional surfactants as building blocks for use in ISA materials. The surfactants are pyrrole-derived monomers, which, on incorporation in ISA structures, can be polymerized yielding supramolecular functional materials.

1.2 Conducting polymers

Intrinsically conducting polymers (ICPs) are an exciting class of electronic materials, owing to their potential of combining the electrical and optical properties of metals or semiconductors with the attractive mechanical properties and processing advantages of polymers.[21] Thus, these materials are beginning to find applications in electrical displays,[22] sensors,[23] electromagnetic shielding,[24] rechargeable batteries,[25] and molecular electronics.[26] Although large-scale interest in conducting polymers is a relatively recent occurrence, interest in conductive polymers began at the end of the 1970's, when it was found that the electrical

conductivity of polyacetylene, a semi-conductor in the pure state, could be increased by over eleven orders of magnitude by treatment with oxidizing agents such as iodine.[27] Although interesting as a model system, the unstable polyacetylene was never a candidate for applications. In the two decades following the discovery of conducting polymers, chemists have made great strides in perfecting simple and inexpensive ways to synthesize more stable conducting polymers, such as polyaniline, poly(vinylpyridine), polythiophene and polypyrrole. Since extensive investigations have been conducted on polypyrrole and its derivatives, this polymer will be discussed in the following sections.

1.2.1 Polypyrrole

Electrodeposition of free standing films of polypyrrole from organic media[28] opened the way to intensive research into polyheterocyclic and polyaromatic conducting polymers.[29] The electrochemical oxidation of the resonance-stabilized aromatic molecules has become one of the principal methods for the synthesis of conjugated, electronically conducting polymers (see section 1.2.3.2). Since the first reports on the oxidation of pyrrole, many other aromatic systems have been found to undergo electropolymerization to produce conducting polymers (Table 1). These include thiophene,[30,31] furan,[31] aniline,[32] indole[31] and paraphenylene[33] as well as many substituted multi-ring and polynuclear aromatic hydrocarbon systems. All the resulting polymers have a conjugated backbone, which is required for electroactivity. Much interest has focussed on pyrrole-based polymers because the substitution chemistry of the monomers is particularly versatile and their chemical or electrochemical polymerization is generally facile in a range of solvents.[34] Polypyrroles exhibit a wide range of surface conductivities ($10^{-3} < \sigma < 100$ S cm^{-1}) depending on several synthesis parameters including the substitution pattern of the monomer, the nature of the dopant counterion and the polymerization temperature.
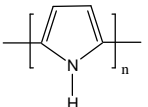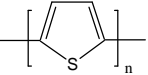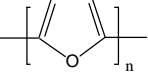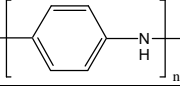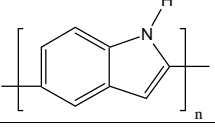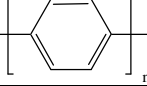
Polymer	Structure
Polypyrrole	
Polythiophene	
Polyfuran	
Polyaniline	
Polyindole	
Polyparaphenylene	

Table 1: Names and idealized structures of the most widely studied conducting polymers.

1.2.2 Mechanisms of Conduction

The mechanisms for electronic conductivity and the nature of charge carriers in conjugated polymers are still a subject of debate. A brief summary of the various theoretical models for the electronic conductivity of conjugated polymers, using polyacetylene and polypyrrole as examples is given below.

Polyacetylene is a linear polymer and, if all bond lengths were equal, each carbon atom would contribute a single electron to the π-band (Chart 1a). Thus, based upon this structure, since the electrons could move only along the chain, polyacetylene would be a one-dimensional (1D) metal. However, neutral polyacetylene is found to be a semiconductor with an energy gap of approximately 1.5eV. This is because such a 1D metal structure is unstable with respect to a dimerization distortion. The phenomenon of such structure instability in a 1D electronic system was theoretically predicted by Peierls in 1955 and is consequently termed the Peierls Instability.[35] According to his assumption, a simple 1D lattice consisting of

atoms with one electron per lattice unit and equal distances between the neighboring atoms $((CH)_x$, a delocalized system) can be distorted and transformed into a lattice with alternating short (or double) bonds and long (or single) bonds, $(—CH=CH)_n$, thereby lowering the energy of the system. Thus, a one-dimensional (or low-dimensional) metal with a half-filled band is structurally unstable against lattice modulation and distortion leading to the opening of a dielectric gap causing the transition of the metal state to a semiconductor or dielectric state. Clearly, by symmetry, one could interchange the double bonds and single bonds without changing the energy (Chart 1b and c). Thus there are two lowest-energy states, having two distinct bonding structures. This twofold degeneracy leads to the existence of structural defects within polymer chains (Chart 1). At the defect site, a single unpaired electron (radical) exists, although the overall charge remains zero, creating a new energy level at mid-gap (a non-bonding orbital). This neutral defect state, known as a 'soliton' is singly occupied, possessing a spin of ½, and is delocalized over about fifteen carbon atoms.[36]
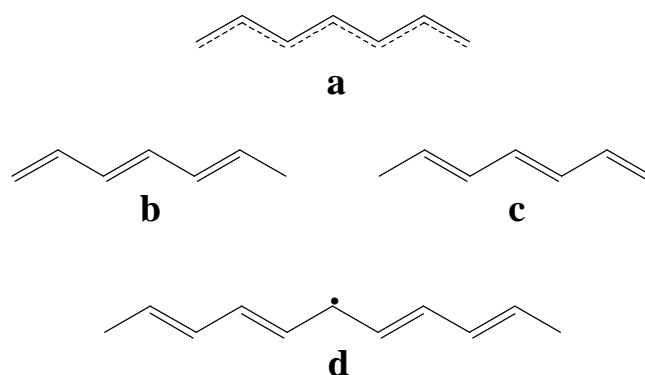
Chart 1: Polyacetylene: undimerized structure (a), two degenerate states (b and c) and a soliton defect boundary where bond alternation is reversed (d).

Oxidation (Scheme 1) or reduction of a neutral soliton yields a charged soliton. Thus, the soliton energy level can accommodate 0, 1 or 2 electrons giving the unusual property of separating spin and charge, with neutral solitons possessing spin but no charge and charged solitons having no spin. In a doped polymer, charge is located in the non-bonding orbital which operates as the HOMO for charge removal and the LUMO for charge injection. Since a defect can occur anywhere along the chain, there is translational symmetry in the system, providing mobility of the soliton along the chain, offering a mechanism for electronic conductivity.
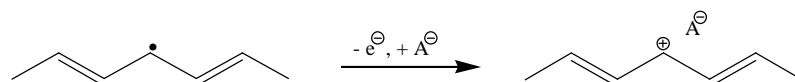
Scheme 1: Oxidation of a neutral soliton to give rise to a positively charged soliton.

Two neutral solitons usually recombine eliminating structural defects, although single solitons can arise on chains with imperfections.[37] In contrast, charged solitons repel each other and lead to isolated charged defects.[36] A neutral soliton and a charged one, however, can achieve a minimum energy configuration by pairing to produce a delocalized radical ion (Scheme 2a represents the case for a radical cation). This radical ion is viewed as a polaron,[38] in that it represents a charged and paramagnetic defect in the $(—CH=CH)_n$ lattice and gives rise to two states in the band gap, a bonding and an antibonding orbital. When two polarons are formed on a chain (Scheme 2b), radical recombination occurs to yield two charged carriers (Scheme 2c).
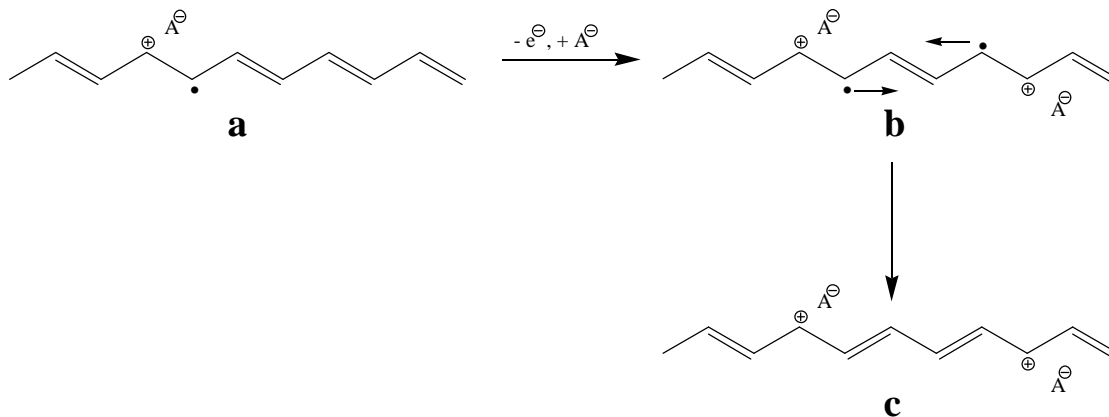
Scheme 2: Oxidation of a chain containing a polaron defect (a) to give rise to a chain with two polaron defects (b). Radical recombination of (b) yields a chain with two charged carriers (c).

These charged sites on the polymer backbone must be charge compensated and, during the doping process, counterions penetrate the polymer matrix for this purpose. If the doping is carried out chemically, then dopant ions are generated from the oxidizing/reducing agent and if the doping is carried out electrochemically, an electrolyte ion is incorporated as the dopant ion. Metallic polymers are, therefore, salts. The doping terminology of conductive polymers should be distinguished from its conventional use in semi-conductor physics since considerably higher concentrations of dopant are employed in the former, typically up to 33 mole% per repeat unit of the chain backbone.[39] The electrical conductivity results from the mobility of the charge carriers on the polymer chain, not the dopant ions. Consequently, doped conjugated polymers are good conductors for two reasons:[21]

1. Doping introduces carriers into the electronic structure. Since every repeat unit is a potential redox site, conjugated polymers can be doped n-type (reduced) or p-type (oxidized) to a relatively high density of charge carriers.

2. The attraction of an electron in one repeat unit to the nuclei in the neighbouring units leads to carrier delocalization along the polymer chain and to charge mobility, which is extended in three dimensions through interchain electron transfer.

(E)-Polyacetylene is the only conjugated polymer to possess a degenerate ground-state. All other conjugated polymers possess non-degenerate ground states and this affects the nature of the charges they can support.[40] In such polymers, where two non-degenerate regions are separated by a topological defect, the formation of single solitons is energetically unfavourable[36] and paired sites are formed. This is the case for polypyrrole which, in the neutral state, can be represented either as the aromatic (Chart 2a) or the quinoid (Chart 2b) structure, the latter possessing the higher energy configuration. Two neutral radicals on a single chain will recombine to eliminate the structural defect,[36] although if one is charged, a polaron is formed which is delocalized over about four rings (Chart 2c). In contrast to polyacetylene, when both defects are charged, they are predicted to pair up to form a 'bipolaron'[36] consisting of a doubly charged defect with no spin (Chart 2d) and extending over a similar number of rings to the polaron. The presence of charge carriers within the polymer chains are responsible for electrical conductivity; thus the polymer structures shown in Chart 2c and d represent the conducting states of the polymer.
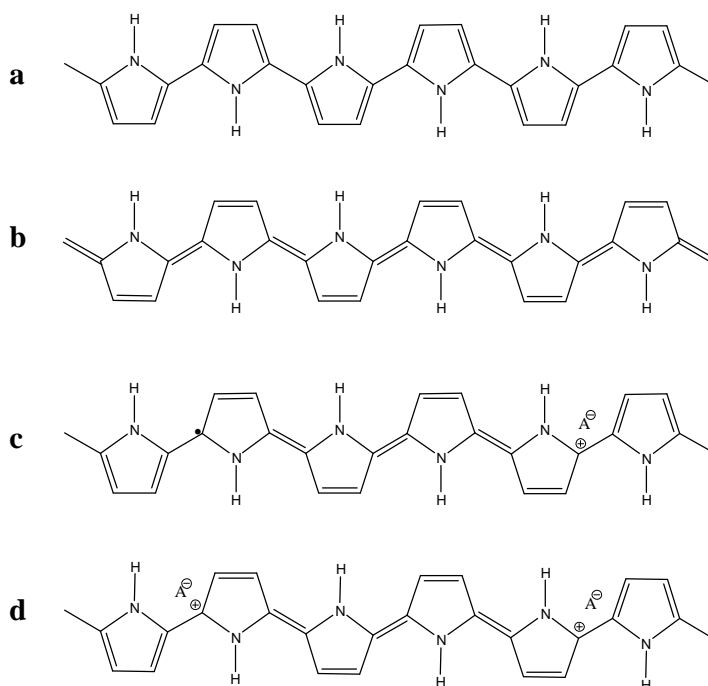
Chart 2: Possible structures of polypyrrole showing the non-degenerate aromatic (a) and quinoid (b) configurations; a polaron defect (c) and a bipolaron defect (d).

Although these charge carriers are responsible for electrical conductivity in conjugated polymers, many structural imperfections are present in all polymers. Thus, when discussing mechanisms of bulk conductivity, these defects need to be considered. Conductivity is not only a result of charge transfer along the chain, but is also due to electron hopping between chains (in 3 dimensions) and between different conjugated segments of the same chain. In addition to these effects, which act at the molecular level, bulk conductivity values are also dominated by electron transfer between grain boundaries and variations in morphology.[41] Thus, the bulk conductivity of a conjugated polymer may be described by the following equation:[42]

$$\sigma = \sum [(n_i\ Z_i\ e\ v_i)/E] \tag{1}$$

where σ = conductivity (S cm^{-1}); n_i = number of charges carried by each type, i; Z_i = carrier type; e = electronic charge (1.60 x 10^{-19} C); v_i = drift velocity of electron (cm s^{-1}); E = electric field (V cm^{-1}).

Typical values for the bulk conductivity of some conducting polymers are shown in Figure 2.
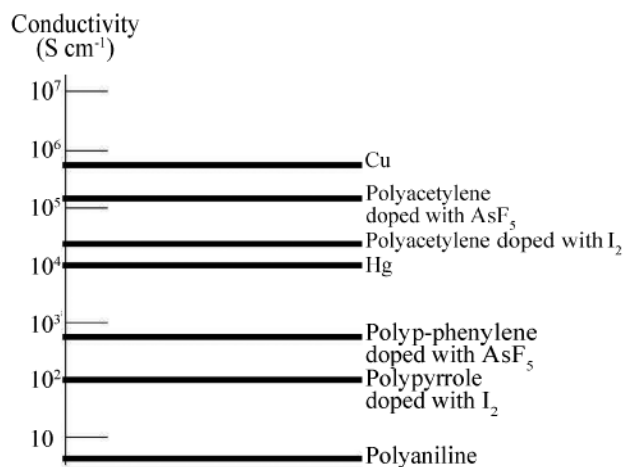
Figure 2: Diagram locating the conductivity of some metals and conducting polymers (adapted from reference 43).

1.2.3 Synthesis of Conducting Polymers

Conducting polymers can be synthesized via chemical or electrochemical routes, although the former has now been largely superceded by electrochemical methods. However, many polymers, most notably polyacetylene, are still only accessible via chemical synthesis.

1.2.3.1   Chemical Synthesis

A large number of conducting polymers can be synthesized via catalytic oxidation. However, control over polymer morphology is extremely limited, purification can be problematic and processing is virtually impossible. Furthermore, although complete doping to the highest concentrations yields reasonably high quality materials, attempts to obtain intermediate doping levels often result in inhomogeneous doping.[21] Nevertheless, this method is still used and, in an effort to reduce its disadvantages, several alternative synthetic routes have been developed, which involve soluble precursor polymers (see section 1.2.4).

1.2.3.2   Electrochemical Synthesis

Electrochemical synthesis of conducting polymers offers many advantages over chemical synthesis,[44] including the in-situ deposition of the polymer at the electrode surface, and hence the control of thickness and morphology as well as the elimination of processing problems. Furthermore, the polymers are simultaneously oxidized to their doped conducting forms during polymer growth. In electrochemical doping, the electrode supplies the redox charge to the conducting polymer, while ions diffuse into (or out of) the polymer structure from the nearby electrolyte to compensate the electronic charge.   The doping level is controlled by the applied voltage. This is in stark contrast to chemical synthesis of polymers where control of doping is difficult.   Thus, electrochemical doping at any level can be achieved by setting the electrochemical cell at a fixed applied voltage and simply allowing the system to come to electrochemical equilibrium (as indicated by the current through the cell going to zero).   A schematic diagram of the generally accepted mechanism for electropolymerization of five-membered heterocycles[45] is shown in Scheme 3.
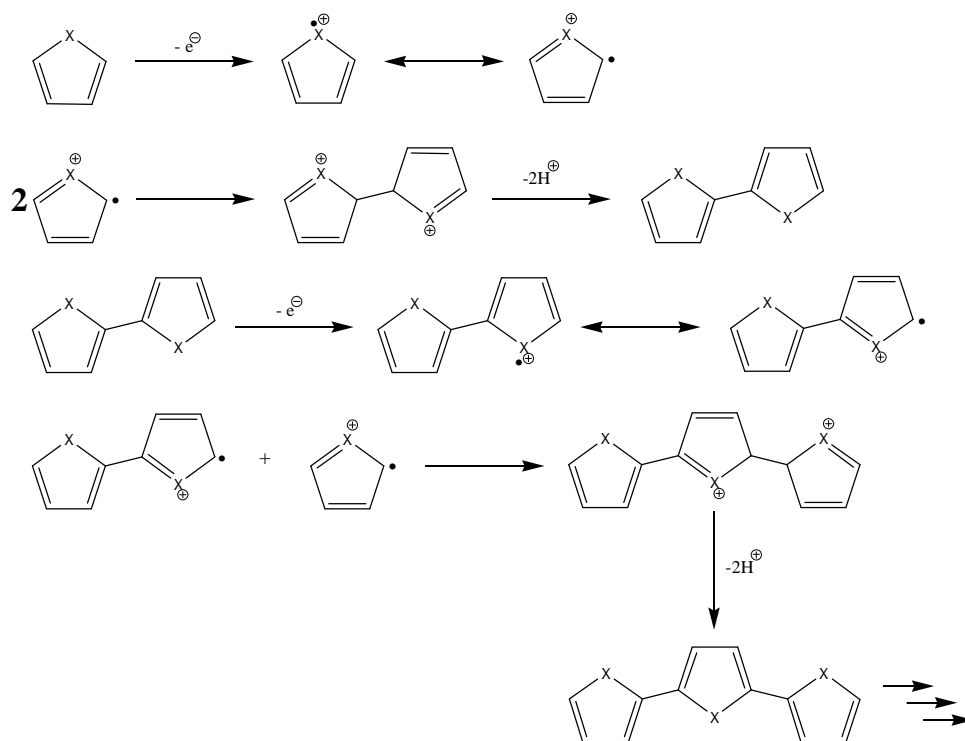
Scheme 3: Proposed mechanism for the electrochemical polymerization of aromatic five-membered heterocycles where X = NH, S or O.

The initial electrochemical step is a one electron oxidation of the monomer to yield its radical cation. A high concentration of this species is maintained at the anode surface because the rate of electron transfer greatly exceeds the monomer diffusion rate to the electrode surface. The second step, a chemical reaction, involves the spin-pairing of two radical cations to form a dimeric dication, which subsequently undergoes the loss of two protons and re-aromatizes to form the dimer. Aromatization is the driving force of the chemical step. Coupling occurs primarily through the α-carbons of the heterocyclic ring since these are the positions of highest unpaired electron π-spin density and, hence, reactivity. At the applied potential, the dimer exists in a radical cation form and, because it is more easily oxidized than the monomer, it undergoes further coupling reactions with other radical cations. This electropolymerization mechanism, according to the general scheme, continues until the oligomer becomes insoluble in the electrolytic medium and precipitates onto the anode surface.[46] Of importance to note is that this mechanism for electropolymerization is greatly simplified, with the nature of the rate limiting step and the exact role of the oligomers in the initial deposition step remaining unresolved.[40]

Non α-α' linkages (e.g. α-β' and β-β' linkages) can occur to variable extents, causing a decrease in the planarity of the backbone and thus a reduction in film conductivity.[47] Such linkages are more profound in the later stages of electropolymerization where the unpaired electron π-spin density of the β-carbon of the oligomer approaches that of the α-carbon.[48] Since conjugated oligomers are oxidized at less positive potentials than their corresponding monomer, polymer oxidation occurs concurrently with electrodeposition. Typically, one electron is removed from the polymeric backbone for every three-four monomer units to form polar structures, responsible for inherent conductivity (see section 1.2.2 on mechanisms of conduction). Conductive polymers can be cycled between the oxidized conducting state and the neutral insulating state,[30a] this process being controlled by the diffusion of counterions into, and out of, the film.[45]

1.2.4 Substituted Heterocycles

Pyrrole and thiophenes substituted at the β-position(s) and also the N-position can undergo polymerization to produce conducting polymers, since the α-positions remain available for monomer coupling.40 Substitution at both β-positions is expected to provide an improvement in the conductivity of the polymers by drastically reducing defect formation during polymerization, through hindrance of β-β' and α-β' linkages.[49] Studies, however, have shown that the conductivity of the polymeric products formed from β-substituted pyrroles and thiophenes is highly dependent on the substituent, with some reactions producing conducting polymers and others, insulating layers.34[50] This behaviour has been attributed to electronic and steric factors that affect the planarity, and thus conductivity, of the polymer chains.[51] N-substituted monomers generally exhibit lower conductivity than their β-substituted counterparts.[52] However, substitution at the N-site is more versatile and the synthetic chemistry is easier. Also, N-substituted heterocycles are symmetric molecules and their symmetry is more conducive to the formation of ordered phases, and thus to polymers having regular structures. This is in contrast to the irregular polymeric structures obtained on polymerization of β-substituted monomers.

1.2.5 Soluble conducting pyrrole-based polymers

In general, polypyrrole polymerized either electrochemically or chemically is known to be insoluble and infusible due to strong inter- and intra-molecular interactions and cross-linkings.[53] The poor processability of polypyrrole has limited its applications. The first reports on soluble conducting polymers appeared in the early 90's, where polyaniline doped with dodecylbenzene sulphonic acid (DBSA) was found to be soluble in common nonpolar or weakly polar solvents.[54] The protonic acid, with its large size, reduces the inter- and intra-molecular interactions of the polymer chains by being incorporated in it as a dopant, improving solubility in organic solvents. Since then, much effort has been directed towards synthesis of soluble polypyrrole and pyrrole-based monomers both through the use of relatively large dopant counterions[55] and β-subsituted precursors.[56] Thus, β-subsituted polypyrroles (especially those with alkyl and alkoxy moieties) not only allow for potential conductivity enhancement (see section 1.2.4) but also allow for solubility in various common

organic solvents, considerably aiding processability and characterization of these electroactive materials.

1.2.6 Polymerization in Organized Media

Initial studies on conducting polymers generally involved materials with amorphous structure and, thus, isotropic properties, since no or little steric regulation of the polymerization process was involved. When cast from solution as thin films, the polymers remain largely a tangle of chains. Transport along the ideal linear chain can proceed no farther than the length of the fully extended chain; then the charge must hop to another chain. In recent years, considerable research efforts have focused on methods to obtain structurally ordered conducting polymers in the expectation that high conductivities will be obtained through the linear alignment of the polymer chains in the solid-state.[57] Attempts to impart directional asymmetry to the structure of conducting polyheterocycles include:

1. Polymerization in restricted geometries e.g. in block copolymers[58] (Figure 3), zeolites[59] and layered inorganic solids;[60] this structural control method makes use of host templates of the appropriate size scale and topology and involves restricted growth of the π-conjugated polymer nanostructures (spheres, wires, sheets) within the confined spaces afforded by the host structure.
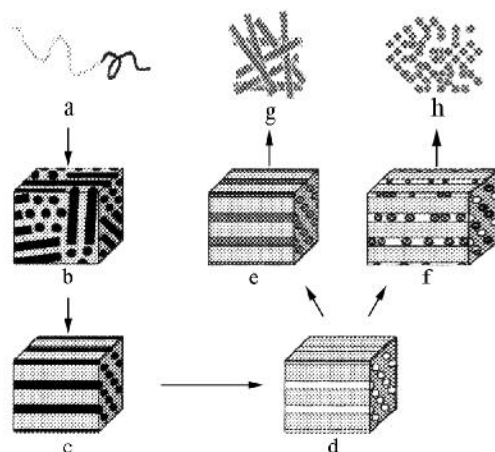
Figure 3: Pathway to nanostructured materials: (a) diblock copolymer chain; (b) polygranular cylindrical morphology; (c) macroscopically aligned cylindrical morphology achieved by flow orientation; (d) removal of minor component to yield nanoporous template; (e) and (f) preparation of nanowires and nanoparticles, respectively within template; (g) and (h) removal of template to obtain nanostructured material (taken from reference 58a).

2. Polymerization in the presence of bulky counterions;[19,61] such counterions, commonly surfactants, not only act as the dopants but also serve to control the resulting polymer structure. An example is the use of β-naphthalene sulphonic acid (β-NSA) in the polymerization of polypyrrole[55c,62] to form micro/nanoscale tubules or fibres in the bulk.

3. Stretch orientation of the polymers;[63]

4. Polymerization in oriented liquid crystals of heterocyclic monomers; this method involves either use of the liquid crystal phase of an appropriate monomer as a template for the polymerization[64] or, alternatively, use of a side group liquid crystal polymer (SGLCP).[34,50,65] SGLCPs consist of three structural components: a conducting polymer backbone, a mesogenic group and connecting these, an alkyl spacer. A range of polymer backbones have been incorporated into these structures, most notably polypyrrole. A variety of liquid crystal phases have been observed including nematic,[50,65,66] smectic and chiral nematic.[66m]

1.3 Objectives

The use of oppositely charged tectons in ionic self-assembly (ISA) not only provides the possibility for facile synthesis of self-organizing materials, but also the chance to use this method as a toolbox for the production of a variety of functional materials. The self-assembly of small functional molecules into supramolecular structures comprises a powerful approach towards the development of new materials and devices of nanoscale dimensions.

The aim of this investigation is to prepare supramolecular systems with an integrated functionality. In this view point, basic supramolecular concepts are applied for noncovalent synthesis of supramolecular entities, with the ultimate objective being the introduction of functions in such ordered structures. Since the ISA strategy has proved to be a facile and viable method for the production of liquid-crystalline materials, we continue our investigations into the phase behaviour and physical properties of a variety of materials, comprising a perylenediimide derivative as the employed oligoelectrolyte. Functionality is introduced into the materials through the use of functional surfactants.

In Chapter 3.1, the synthesis and phase characterization of functional pyrrole-containing surfactants is presented. Owing to the presence of the pyrrole moiety, these surfactants are not only polymerizable but are also potentially conductive when polymerized. We adopted N-substituted pyrroles as target molecules. Although polymers derived from such pyrroles generally exhibit lower conductivity than those derived from monomers substituted at the β-position, the synthesis of N-substituted monomers is considerably easier and the symmetry of the resultant species is more conducive to the formation of ordered phases. These synthesized pyrrole-derived surfactants are then employed in the synthesis of ISA complexes. Through the presence of a polymerizable moiety within the surfactant molecule, a polymerization reaction within confined geometry is performed by both chemical and electrochemical methods. Molecular self-assembly is expected to pre-organize the monomers so that polymerization within the assembly will afford a highly ordered polymer. This could lead to new architectures and enhanced optical and electrooptical properties of devices.

In Chapter 3.2, the motif investigated is a property rather than a function, i.e. the influence of chirality, originating from the surfactants employed in the synthesis of the ISA materials, on the supramolecular organisation of the resulting complexes. Chirality can perhaps be seen as a second order source of stored structural information that is available for exploitation in the synthesis of ISA materials. Although chirality is not a true function, the aim is to investigate whether chiral surfactants acts as structure-inducing moieties within the ISA complexes, enabling the induction of chirality within the superstructures. Few publications report on perylene diimide assemblies that exhibit chirality. These investigations address self-assembly of perylene tectons which are intrinsically chiral,[67,68] or hydrogen-bonded aggregates of perylenes with chiral tectons.[8,68,69] The ISA method does away with the tedious synthetic operations required for synthesis of chiral perylenes and, compared with the hydrogen-bonding approach, makes use of stronger interactions between the binding partners allowing for better-defined assemblies.

Thus, this thesis addresses investigations into the use of functional surfactants in nanostructured ISA materials. The novel ISA complexes are characterized by a variety of techniques including thermal analysis, absorption and circular dichroism spectroscopy, optical polarization microscopy and X-ray scattering.

2   CHARACTERIZATION METHODS

2.1 X-ray Diffraction

X-ray diffraction (XRD) is one of the most powerful techniques for revealing the internal structure of materials. When the radiation wavelength is of the order of the intermolecular spacing, the electromagnetic radiation interacts with the inhomogeneous but periodical electron density distribution, within the material leading to a characteristic diffraction pattern.[70] X-ray diffraction patterns can give readily interpretable information about the relative molecular positions, the presence of long-range positional order, the quality of the preferred orientation with respect to an external axis and details of crystal structure and perfection.   One of the central relations of crystal diffraction is the well-known Bragg equation,[71] which reduces the diffraction to reflection of X-rays on one set of crystal planes (Figure 4). Positive interference only occurs if the phase shift of the two rays is a multiple of the wavelength and since this shift calculates to 2d sin θ, the Bragg equation is:

nλ = 2d sinθ (2)

where n is the 'order' of the diffraction, λ is the wavelength, d is the distance between successive planes and θ is the angle of the incident beam with the planes.
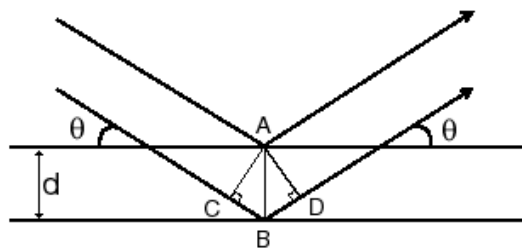

Figure 4: Scattering and diffraction of a coherent beam of X-rays from parallel planes of atoms spaced at a distance, d, apart. The diffraction condition is that of coherence of the diffracted beam. The path lengths of the two rays shown differ by the distance CBD, which must be equal to an integral number of the wavelength for the scattered rays at the angle, θ, to be in phase with each other.

The Bragg equation underlies the fact that the beam is diffracted through a defined angle by interacting with a set of standing waves in electron density i.e. the planes. The position of a refection results from the respective distance of the repeat units, the d-spacing, which depends solely on the geometry of the sample's unit cell. The geometric restrictions of the Bragg relationship mean that a monochromatic beam directed at a perfect single crystal in an arbitrary orientation is unlikely to produce any diffracted beams at all. However, if the sample consists of many crystals in all possible orientations a sufficient proportion will be correctly oriented to diffract. The relative intensity of the signals depends on the type of atoms in the crystal and their location on the unit cell.

A useful construction for helping in the interpretation of X-ray diffraction patterns is the following equation which introduces the scattering vector, *s*

$$s = 1/d = 2/\lambda\ \sin\theta \tag{3}$$

The set-up for the measurement of powders is rather straight forward. The X-rays are produced in a vacuum X-ray tube (Figure 5) that contains essentially two electrodes: an anode commonly made of copper, and a cathode, usually a tungsten filament, as electron source. The cathode is heated to emit electrons and when a high voltage is applied between the electrodes, streams of electrons (cathode rays) are accelerated from the cathode to the anode and induce the emission of X-ray radiation from the anode. Very often the set-up is such that the anode is constantly rotated preventing it from overheating and thus ensuring a constant flux of X-rays. Due to their small wavelength, X-rays cannot be focussed by lenses but only by slits, causing a great loss in intensity. Soller slits lead to irradiation with minimized lateral divergence. The scattered irradiation is again narrowed by slits and eventually enters the detector.
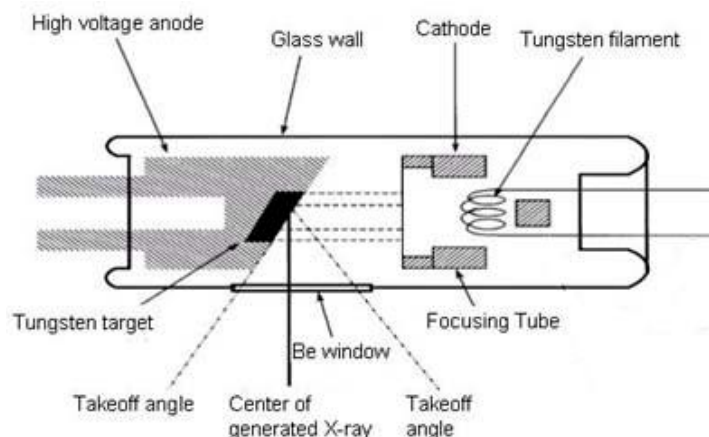
Figure 5: Schematic diagram of an X-ray tube. Electrons from the heated filament cathode are accelerated to a high velocity with a high-voltage field causing them to collide with a target, the anode plate. Electrons focused on the anode collide with and accelerate other electrons, ions and nuclei within the anode material and about 1% of the energy is generated as X-Ray photons.

X-ray techniques are usually categorized into wide angle X-ray scattering (WAXS) and small angle X-ray scattering (SAXS). Since the larger the diffraction angle, the smaller the length scale probed, WAXS is used to determine crystal structure on the atomic length scale while SAXS is used to explore microstructure on the colloidal length scale. Thus, WAXS routinely covers the angular range 7-60°, providing information about the atomic distribution in the length scale of 0.1 - 0.6 nm and SAXS occurs at low scattering angles (1-10°), covering the range 0.4 - 4.4 nm. SAXS measurements are technically challenging because of the small angular separation of the direct beam and the scattered beam. Large specimen-to-detector distances (0.5 m - 10 m) and high quality collimating optics are used to achieve good signal-to-noise ratio in the SAXS measurement. Small and wide-angle X-ray scattering is a useful and complementary method for determining the size, size distribution and structure of a wide range of disordered (non-crystalline or semi-crystalline) materials including polymers, liquid crystals, oils and suspensions.

2.2 Circular Dichroism

Circular dichroism (CD) spectroscopy is an optical technique that measures the difference in absorbance of right- and left-circularly polarized light, which arises due to structural asymmetry. Thus, this technique allows the detection and quantization of the chirality of molecular structures. It also provides information about the secondary and tertiary structures of many materials including biopolymers, proteins and DNA.[72]

Plane polarized light is the sum of left- and right-circularly polarized light (Figure 6a). When the plane polarized light is passed through a birefringent plate, the light is split into two plane-polarized beams oscillating along different axes. When one of the beams is retarded by 90° (using a quarter-wave retarder) then the two beams, which are now 90° out of phase, are added together resulting in circularly polarized light of one direction. By inverting the two axes such that the alternate beam is retarded, circularly polarized light of the other direction is generated. When plane polarized light passes through an optically active substance, the left- and right-circularly polarized components of the plane polarized light are absorbed by different amounts (Figure 6b). When these components are recombined they appear as elliptically polarized light (Figure 6c).
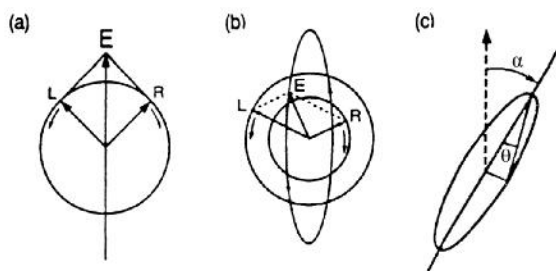

Figure 6: a) Plane-polarized light resolved into two circularly polarized components, R and L. As long as the intensities of the two circularly polarized components remain the same, their resultant will lie in a plane and oscillate in magnitude; b) If the right-circularly polarized component is absorbed more (less intense) than the left-circularly polarized component, the electric vector of the light will follow an elliptical path corresponding to elliptically polarized light; c) The major and minor axis of the ellipse form a triangle and the angel opposite to the minor axis, θ, is the ellipticity. The major axis of the ellipse has been rotated through the angle, α, corresponding to the optical rotation.

A schematic diagram of the CD setup is shown in Figure 7. A periodic variation in the polarization of the light beam is induced by the polarization modulator through all ellipticities from left-circular through elliptical, unchanged linear and elliptical to right-circular. This polarized light passes through the sample to a photomultiplier detector. If the sample is not optically active, the light beam does not vary through this cycle. With the introduction of an optically active sample, a preferential absorption is seen during one of the polarization periods and the intensity of the transmitted light now varies during the modulation cycle. The variation is directly related to the circular dichroism of the sample at that wavelength. Successive detection of the ellipticity, θ (in millidegrees), is determined for the difference of the absorption coefficients of left- and right-circularly polarized light at various wavelengths and leads to the generation of a CD spectrum.
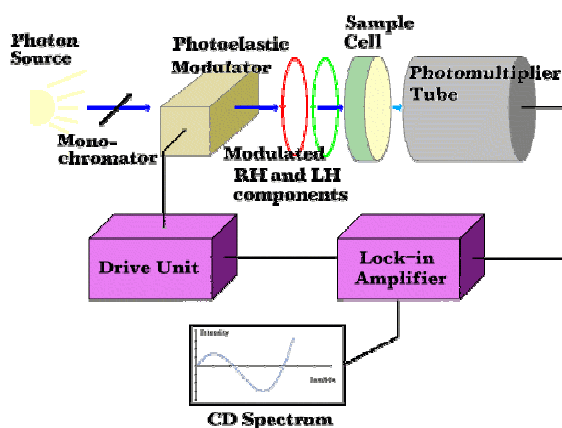

Figure 7: Schematic diagram of the CD setup. The polarization modulator induces a periodic variation in the polarization of the light beam. A preferential absorption of circularly polarized light of one direction occurs by the optically active sample at various wavelengths and leads to the generation of a CD spectrum.

The difference between absorbance of left-circularly polarized and right-circularly polarized light, ΔA, can be expressed as:

$$\Delta A = (\varepsilon_L - \varepsilon_R) \, C \, l \qquad\qquad (4)$$

where ε_L and ε_R are the molar extinction coefficients for left- and right-circularly polarized light, respectively (L mol^{-1} cm^{-1}), C is the molar concentration (mol L^{-1}) and l is path length (cm).

Although ΔA is usually measured, measurements are generally reported in ellipticity, θ (mdeg)

$$\theta = 32980 \times \Delta A \tag{5}$$

The molar ellipticity, $[\theta]$ (deg cm^2 dmol^{-1}) is given by:

$$[\theta] = (\theta M) / (10,000 \times c\ l) \tag{6}$$

where M is molecular weight (g mol^{-1}), c is concentration (g ml^{-1}) and l is the cell path (cm)

Since:

$$C = (1000 \times c) / M \tag{7}$$

where C is the molar concentration (mol L^{-1}), it follows that:

$$[\theta] = \theta / 10 \times C\ l \tag{8}$$

In the CD spectrum, positive or negative circular dichroism is observed as a function of the wavelength, depending on which of the two circularly polarized components is absorbed stronger. The positive and negative displacement from zero of the rotation of plane polarized light and the change of circularly polarized light into elliptically polarized light in the vicinity of the absorption band of the substance is termed the Cotton Effect. A right optical rotation leads to a positive Cotton effect and a left rotation, to a negative Cotton effect.

The ultraviolet CD spectrum of proteins can predict important characteristics of their secondary structure. Three types of conformations are commonly observed: α-helix, β-sheet and random coil and each gives rise to a characteristic shape and magnitude of the CD signal (Figure 8).
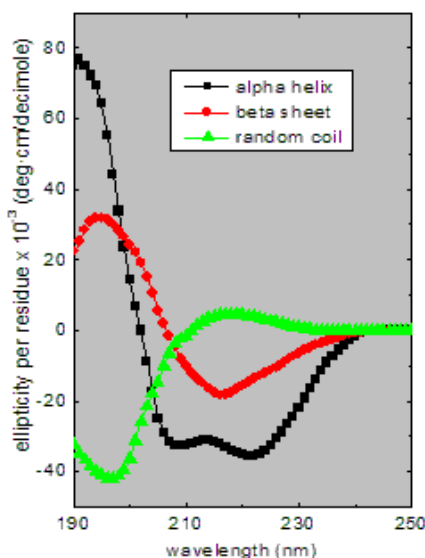

Figure 8: CD spectra for polylysine in the α-helix, β-sheet and random coil conformations.

The approximate fraction of each secondary structure type that is present in any protein can thus be determined by analyzing its far-UV CD spectrum as a sum of fractional multiples of such reference spectra for each structural type. CD cannot, in general, give information of where, for example, the detected alpha helices are located within the molecule, nor can it predict how many there are. Despite this, CD is a valuable tool, especially for showing changes in conformation. It can, for instance, be used to study how the secondary structure of a molecule changes as a function of temperature or concentration of denaturing agents. In this way, it can reveal important thermodynamic information about the molecule that cannot otherwise be easily obtained.

2.3 Polarized Light Microscopy

Polarized light microscopy is a technique that exploits optical properties of anisotropic materials to reveal detailed information about the structure and composition of materials.[73] Anisotropic materials have crystallographically distinct axes and interact with light in a manner that is dependent upon the orientation of the crystalline lattice with respect to the incident light. Thus, polarized microscopy is an invaluable tool in the investigation of liquid crystalline materials.

In a polarizing microscope there are two polarizing filters - the polarizer and analyser (Figure 9). When both are in the optical path, their permitted vibration directions are positioned at right angles to each other. In this configuration, the polarizer and analyzer are said to be crossed, and since no light passes through the system a dark field of view results.

When light enters a non-equivalent axis in an anisotropic crystal, it is refracted into two rays (an ordinary and extraordinary ray) each polarized with the vibration directions oriented at right angles to one another, as illustrated in Figure 9. The velocities of these components are different and vary with the propagation direction through the specimen. This phenomenon, where the sample exhibits distinctive refractive indices, is termed birefringence and is observed in all anisotropic materials. After exiting the specimen, the light components become out of phase, but are recombined with constructive and destructive interference when they pass through the analyzer.
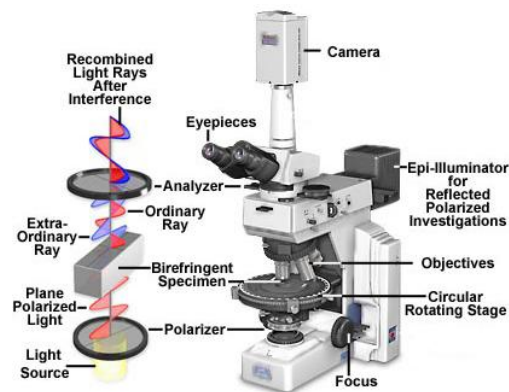

Figure 9: A polarized light microscope showing the main components. When light enters a non-equivalent axis in an anisotropic crystal, it is refracted into two rays (an ordinary and extraordinary ray) each polarized with the vibration directions oriented at right angles to one another.

The visibility of a birefringent material between crossed-polars will oscillate between bright and dark four times, in 90° intervals over a range of 360° on rotation of the sample with respect to the polarizer (Figure 10). When the anisotropic birefringent material has its long (optical) axis oriented parallel to the direction of the polarizer, the polarized light impacts the specimen with a vibration direction parallel to the optical axis. As a result the specimen will appear isotropic (dark or extinct, Figure 10a).

When the optical axis of the material is positioned at an angle, α, with respect to the polarizer, a portion of the light received through the polarizer is passed on to the analyzer (Figure 10b). Quantification of the amount of light passing through the analyzer is accomplished by dropping projections of the vectors of both the ordinary (o) ray and extraordinary (e) ray onto the axis of the polarizer (P). This method assumes the arbitrary value of 1 for the intensities of both rays. The contributions from the polarizer for o and e are projected onto the analyzer axis (A) as the absolute value R. When R has a positive value, some of the light from the polarizer has passed through the analyzer and the birefringent material displays an intermediate degree of brightness. The maximum brightness for a birefringent material occurs when the optical axis of the material is oriented at a 45° angle to both the polarizer and analyzer (Figure 10c).
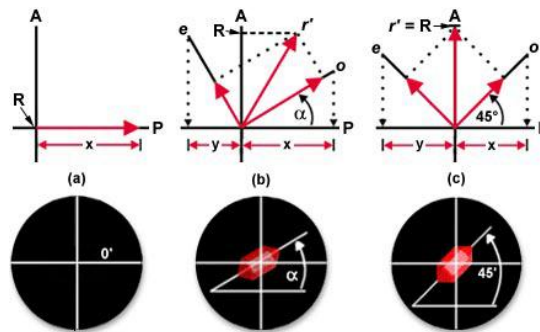

Figure 10: A birefringent material between crossed polars. a) the optical axis of the material is oriented parallel to the direction of the polarizer (P) and results in the material being totally extinct. b) The optical axis of the material is positioned at an angle, α, with respect to P. Projections of the vectors of the ordinary (o) and extraordinary (e) rays gives the contributions from the polarizer for o and e, illustrated by x and y. These produce the resultant r', projected onto the analyzer axis (A) as the absolute value, R. c) The optical axis of the material is positioned at a 45° angle with respect to P. This computes the maximum possible contribution to light passed to the analyzer.

Thus, when the orientation of the birefringent material is altered, incident light rays will be resolved by the specimen into ordinary and extraordinary components, which are then united in the analyzer to yield interference patterns. The technique of polarizing microscopy exploits the interference of the split light rays to extract information about these materials.

3   RESULTS AND DISCUSSION

3.1 Pyrrole-based surfactants

3.1.1 Synthesis

In order to pursue the goal of 'real' functional self-assembled materials, we have synthesized two pyrrole-containing surfactants. Due to the presence of the pyrrole moiety, these surfactants are not only polymerizable but also potentially conductive when polymerized. Synthesis of the double-tailed surfactant, Dodecyl-dimethyl-(2-pyrrol-1-yl-ethyl)-ammonium tosylate (**4**), and the single-tailed surfactant, Triethyl-(12-pyrrol-1-yl-dodecyl)-ammonium bromide (**6**) are shown in Scheme 4 and Scheme 5, respectively (for details see section 5.2.2.1).
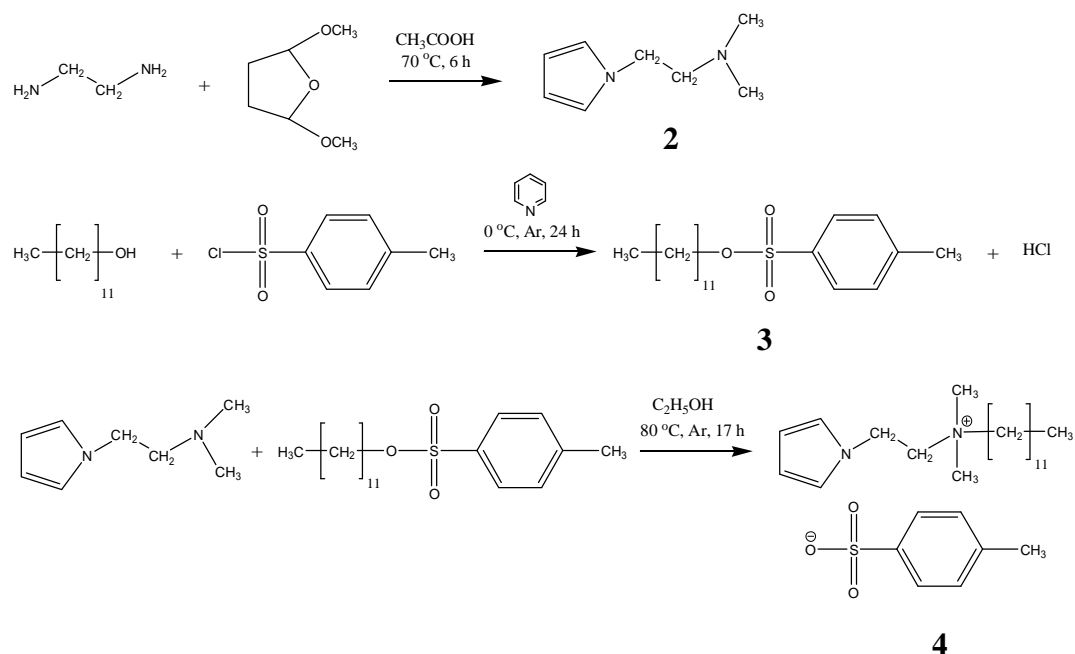
Scheme 4: Synthesis of the double-tailed pyrrole-based surfactant, Dodecyl-dimethyl-(2-pyrrol-1-yl-ethyl)-ammonium tosylate (4).
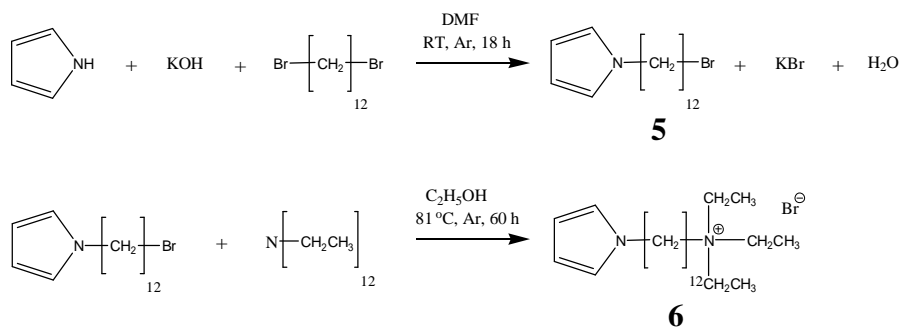
Scheme 5: Synthesis of the single-tailed pyrrole-based surfactant, Triethyl-(12-pyrrol-1-yl-dodecyl)-ammonium bromide (6).

3.1.1.1   Phase Characterization of Double-tailed surfactant

Since routine characterization analysis of the double-tailed pyrrole-containing surfactant (**4**) indicated a very interesting, complex phase behaviour, we decided to conduct a comprehensive investigation on the properties of this surfactant. The importance of this investigation is based on the desire to integrate the system within self-assembled structures to obtain conducting materials. While similar surfactants have already been used in recent studies for the fabrication of polymer-inorganic mesostructures, only a few studies have addressed the fundamentals of surfactant and mesophase properties. The present work shows, for the first time, a complete characterization of this type of surfactant, especially its concentration-dependent phase behavior in water. Aggregation properties have already been well-documented[74,75,76] but it is, to the best of our knowledge, the first investigation which addresses the propensity of a pyrrole-containing surfactant to form mesophases.

3.1.1.1.1   Solid-state Properties

The thermal properties of surfactant **4** were investigated by thermogravimetric analysis (TGA) and differential scanning calorimetry (DSC). TGA analysis reveals that the degradation temperature is above 225 $^{\circ}$C (Figure 11a). DSC analysis shows an endothermic transition at $\approx$ 109 $^{\circ}$C on the heating curve. This transition is reversible, appearing as a peak on the cooling curve at $\approx$ 72 $^{\circ}$C (Figure 11b).

a)

b)

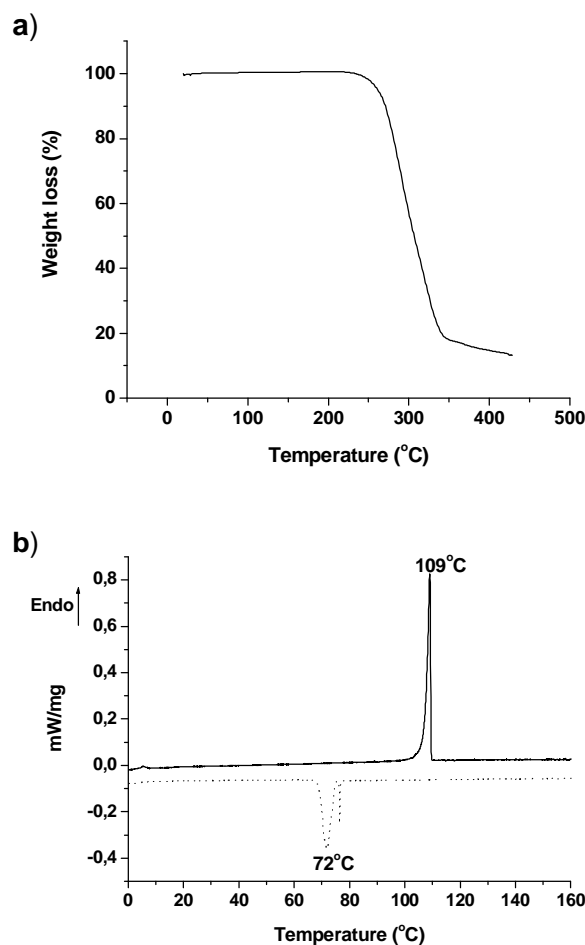**Figure 11: a) TGA plot of surfactant 4 performed at a heating rate of 20 K min^{-1}; b) DSC plot of surfactant 4 performed at a heating/cooling rate of 1 K min^{-1} (solid line - 2nd heating curve; dashed line – 1st cooling curve).**

The temperature-dependent phase transition of **4** observed with DSC was confirmed by polarized light microscopy (PLM) and wide-angle x-ray scattering (WAXS). The melted (isotropic) surfactant forms, upon rapid cooling from 105 ^{o}C, a birefringent phase at 75 ^{o}C. This phase persists on a further heating cycle up to 106 ^{o}C. This is in agreement with the DSC data, in the range of temperature precision of each technique. The reappearance of the birefringent phase upon cooling is slightly shifted to 71 ^{o}C, where this birefringent phase now coexists with an isotropic phase (Figure 12a). If left to equilibrate for a short time, two types of solids grow in the isotropic phase, as clearly shown in Figure 12b. The "fan-like" solid may be a different polymorph of the initial crystallites of **4**. Upon remelting of the solid and

then fast cooling, a glassy liquid forms at 72 °C (Figure 12c). A mesophase in the shape of spherulites -or maltese crosses- occurs at 65 °C upon fast cooling (Figure 12d).
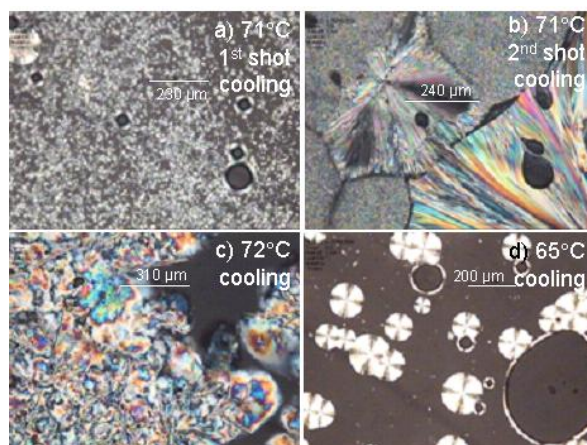

Figure 12: Optical micrographs of surfactant 4 at various temperatures, with no water. The solid was first melted and then cooled very rapidly at a rate of 60 K min^{-1}. Pictures were taken upon cooling only. Micrographs *a* and *b*, taken at the same temperature (71 °C) but one after the other, show two solids (*b*) growing from the isotropic region that coexists with a birefringent mesophase (*a*). Micrograph *c*, taken at 72 °C upon another melting and cooling cycle, is typical of a glassy liquid. Upon further cooling, spherulites appear in the isotropic region at 65 °C.

These phase transitions are also supported by WAXS measurements (Figure 13a). At RT, the diffractogram shows multiple sharp reflections implying a highly crystalline material. A broad peak is observed at 120 °C resulting from the liquid-like arrangement of the surfactant molecules. After cooling to 60 °C, the diffractogram exhibits a pattern similar to that observed at RT. The WAXS diffractograms obtained after cooling from the melt at different rates (rapid cooling at 60 K min^{-1}; slow cooling at 1 K min^{-1}) were also similar to the RT diffractogram run before heating the sample.

Room temperature SAXS analysis of surfactant **4** (both before and after annealing of the sample at 150 °C for 30 mins) shows that long-range nanometer order is present. The well-developed scattering peaks are easily indexed to a lamellar phase with a d-spacing of 3.13 nm (indicated by the arrows in Figure 13b).
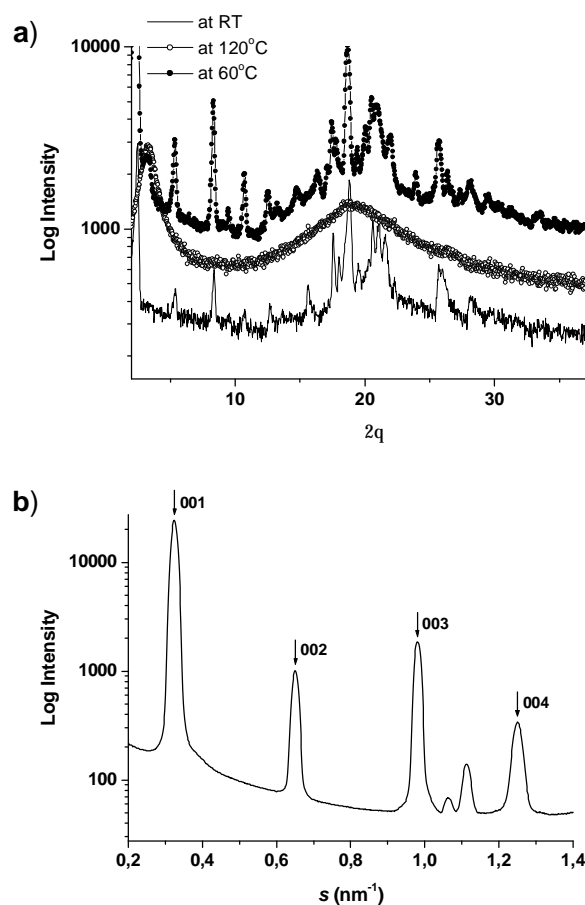
Figure 13: a) Temperature-dependent WAXS of surfactant 4 performed at a heating/cooling rate of 10 K min^{-1} (solid line-at RT; open circles - at 120 °C; closed circles - at 60 °C after heating to 120 °C); b) SAXS of surfactant 4 after annealing at 150 °C for 30 mins.

Using Tanford's fomula,[77] the maximum length of a C_{12} alkyl chain is 1.66 nm. Thus, in the absence of interdigitation, the thickness of the lamella is, at least, 1.668 x 2 = 3.336 nm. The obtained value for the d-spacing shows that interdigitation of the alkyl chains occurs within the system. The lamellar structure observed by the SAXS measurements is also corroborated by the observation of Maltese crosses with PLM during recrystallization of **4**, upon cooling from the isotropic melt (Figure 12d).

3.1.1.1.2   Micellization in Water

The critical micelle concentration (cmc) of **4** was determined by potentiometric and isothermal titration calorimetry (ITC) measurements, and further supported by surface tension measurements. The measurements were performed at 40 ^{o}C to ensure complete solubility of the surfactant (lyotropic investigations, discussed in section 3.1.1.1.3, show that T_{krafft} of **4** is ≈ 27 ^{o}C). However, this caused some experimental problems in the case of the surface tension measurements. Surface tension measurements at higher temperatures (in this case, at 40 ^{o}C) could only be performed on concentrated solutions of the surfactant in back-titration mode. This however caused changes in the concentration of the titrated solution due to evaporation from the titration vessel. This has led to severe experimental difficulties in determining the correct cmc value using this technique, and therefore only serves to corroborate the values found from potentiometric and ITC titrations.

Since potentiometry using surfactant-selective electrodes is a suitable method for cmc determination,[78] the cmc value of surfactant **4** was substantiated by potentiometric measurements. When below the cmc, an increase in surfactant concentration results in an increase in the activity of free surfactant and this causes a quasi-Nerstian increase in the electrical potential. Above the cmc, however, the activity of free surfactant molecules remains constant. Thus, the curve of the electrode response shows an angular discontinuity corresponding to the cmc of the surfactant. The potentiometric curve obtained for **4** at 40 ^{o}C in 10^{-2} M NaOTs electrolyte is shown in Figure 14, and the cmc is 0.9($\pm$0.1) x 10^{-3} M under the specified conditions (initial slope of the curve = 62.2 mV). The use of sodium tosylate electrolyte as the measurement medium allows the activity of the counterions and, thus the activity of the surfactant ions, to remain relatively constant above the cmc; when pure water is used as the medium, the activity of the surfactant ions decreases after the cmc resulting in a negative slope.[78,79]
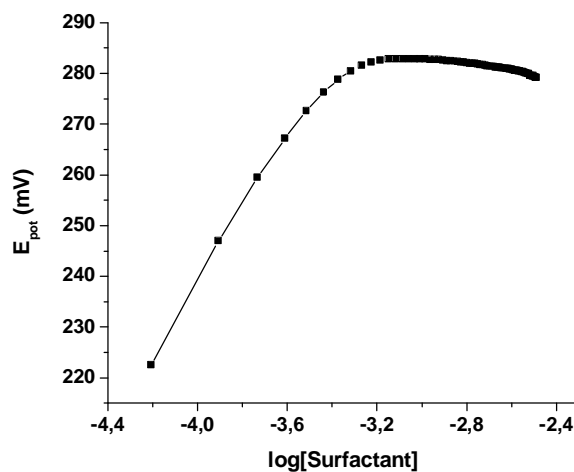
Figure 14: Electrical potential as a function of the concentration of surfactant 4 at 40 ^{o}C (in 10^{-2} M NaOTs electrolyte).

The cmc of **4** at 40 ^{o}C was further confirmed by isothermal titration calorimetry (ITC). The titration curve obtained from dilution of a micellar surfactant solution at 40 ^{o}C is shown in 5a. During the first injections, the concentration within the sample cell is below the cmc. Here, the large enthalpic change that occurs with each injection results from the demicellization process and dilution of the resulting monomers. These injections produced positive peaks, characteristic of an endothermic process. A plot of the integrated heat normalized by the number of moles of **4** injected into the working cell is shown in Figure 15b. The curve is extrapolated to two different states: the monomer state at low surfactant concentrations and the micellar state at higher concentrations. The decrease in the heat at a mean concentration of 0.84 mM indicates that the cmc in the sample cell has been reached. If more micellar solution is added, demicellization does not take place and the only heat that is measured is caused by the dilution of micelles. The cmc corresponds, therefore, to the concentration where the first derivative of the curve in Figure 15b displays a minimum (Figure 15c). The enthalpy of demicellization, $\Delta H_{demicellization}$, is equal to the difference between the two extrapolated lines in Figure 15b, and is approximately -2.83 kJ mol^{-1}.
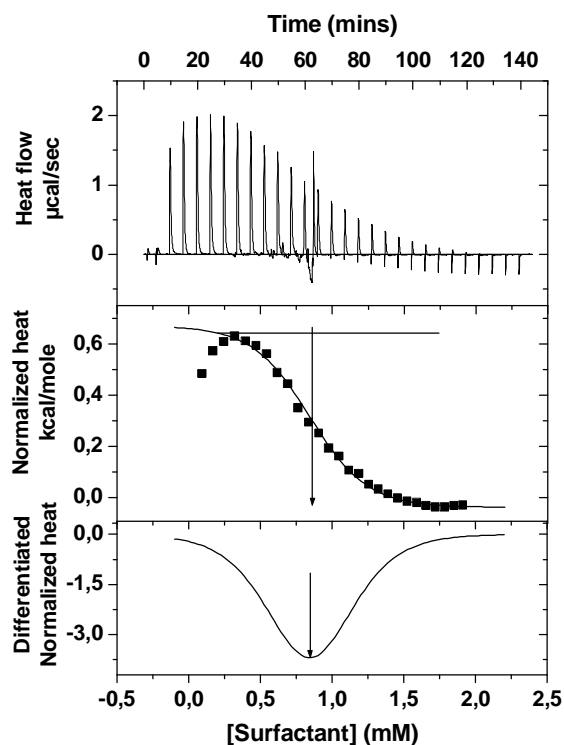
Figure 15: Titration of 10 µL aliquots of an 11 mM solution of surfactant 4 in 10^{-2} M NaOTs electrolyte to the sample cell filled with 1.442ml of the electrolyte at 40 °C; a) Calorimetric data (heat flow against time); b) Normalized heat (obtained by integration of peaks in upper curve) vs. total concentration in the sample cell (the enthalpy of demicellization is represented by the length of arrow); c) First derivative of curve b calculated numerically from interpolated values (the cmc is defined as the concentration where this curve has a minimum).

The plot of surface tension against surfactant concentration is depicted in Figure 16. Initially, the concentration was above the cmc so, with decreasing surfactant concentration, the surface tension did not change considerably until the cmc was reached. Constant values could not be obtained in this region of the plot because of changes in the concentration of the surfactant solution due to evaporation. Below the cmc, the surface tension increased with decreasing surfactant concentration. The cmc is taken as the concentration where the surface tension changes its trend and is found to be 1.0×10^{-3} M at 40 °C. The surface tension measurement was carried out in pure water since it is known that an irregular significant drop in the corresponding curve is observed in the presence of sodium tosylate electrolyte.[75]
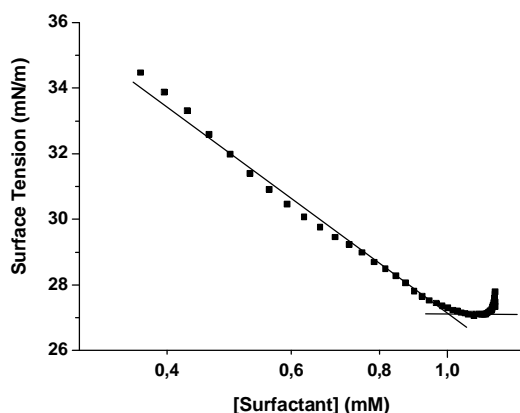
Figure 16: Surface tension as a function of the concentration of surfactant 4 at 40 ^{o}C. The cmc is taken as the concentration where the surface tension changes its trend.

The minimum interfacial area a_{min} per surfactant molecule could be deduced from the surface tension experiment by means of the Gibbs adsorption equation[78] and was found to be 129 $\mathring{A}^2$ molecule^{-1} (see Appendix, Equations 1-3).   However, due to the mentioned problems, the value obtained here can only be seen as an estimate. When compared to a_{min} values of usual n-alkyltrimethylammonium cationic surfactants,[80] the a_{min} value of **4** (129$\mathring{A}^2$ molecule^{-1}) is expectedly large. The value lies between those found for the two surfactants with referenced cmc's that differ from **4$^+$** by the counterion (Table 2, entries 2 and 3).[76] Investigation of micelle formation using a fluorescence probe (e.g. pyrene)[81] was not attempted since this method was found to be unsuccessful for a similar surfactant (namely, a single-tailed pyrrole-containing surfactant having tosylate as the counterion - Table 2, entry 4).[75] The failure of the pyrene probe experiment has been attributed to a strong quenching of the probe fluorescence by the pyrrole moieties and tosylate anions when the concentration of surfactant reached the cmc.

It is evident that the cmc values obtained by the three different methods are in excellent agreement with each other. Thus, the cmc of **4** at 40 ^{o}C can be stated as 0.9 ($\pm$0.1) mM. The cmc values of the double-tailed pyrrole-containing surfactant, but with counterions other than the tosylate anion, have been found to be much higher than the cmc found in this investigation. The two cationic surfactants identical to **4$^+$** with referenced cmcs are the nitrate and bromide forms (Table 2, entries 2 and 3). The cmc values of the nitrate form (at 45 ^{o}C)

and bromide form (at 50 ^{o}C) are found to be approximately 4 mM.[76] The significantly lower cmc of our surfactant may partially result from the decreased temperature at which the cmc measurement was performed but certainly also results from an increased hydrophobic character of surfactant **4** attributed to the aromatic counterion, a factor known to strongly lower the cmc.[82,83]

Furthermore, substitution of the N-ethylpyrrole group and two methyl groups attached to the nitrogen cation in surfactant **4** with ethyl groups and positioning of the pyrrole ring at the end of the long alkyl chain, to give the single-tailed pyrrole surfactant (Table 2, entry 4) induces a considerable increase in the cmc.[75,76] This phenomenon is the consequence of a large decrease in the headgroup hydrophobicity. Thus, the considerably low cmc value of **4** is attributed to (a) the relatively hydrophobic headgroup, which incorporates the aromatic pyrrole moiety and (b) the aromatic counterion.
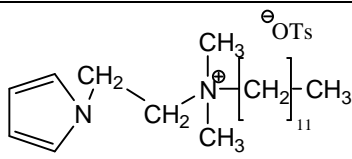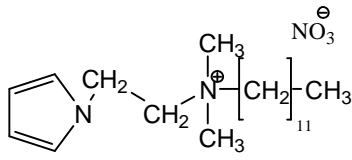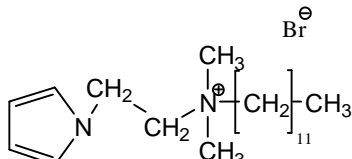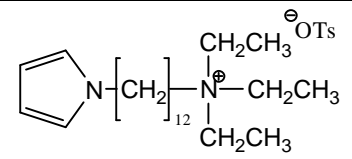
Entry	Surfactant	cmc (mM)	a_{min} (Å^{2}molecule^{-1})	Temperature (^{o}C)
1		0.9($\pm$0.1)	129	40
2[i]		3.5($\pm$0.5)	87	45
3[i]		4.0($\pm$1.0)	176	50
4[ii]		4.4($\pm$1.0)	92	25

Table 2: Values of the cmc and a$_{min}$ at specific temperatures for a variety of pyrrole-containing surfactants; TsO^{-} represents the tosylate anion.

i Data from reference 76; values obtained using the surface tension method.

ii Data from references 75 and 76; values obtained using the surface tension method.

Light scattering experiments were performed at various temperatures (25, 30, 40, 50 and 55 $^{\circ}$C) on solutions of **4** in water below (6.3 x 10^{-6} M) and above (1.24 x 10^{-3} M) the found cmc. Measurements at 25 $^{\circ}$C did not yield any results due to the formation of turbid solutions, and confirmed the Krafft temperature. As expected, no aggregates were observed in the investigation of the 6.3 x 10^{-6} M solution (below the cmc) at any of the other chosen temperatures. In the case of the 1.24 x 10^{-3} M solution (above the cmc), the presence of large aggregates was detected (the mean radius decreased from approximately 400 nm to 100 nm with a temperature increase from 30 $^{\circ}$C to 55 $^{\circ}$C, Appendix, Figure 1). This suggests that a dilute solution of **4** above the cmc is within the L_2 dispersion region (see below). Coche-Guérente et al. have already reported aggregates with a mean diameter of 205 nm in a C-12 single-tailed pyrrole-containing surfactant, with BF_4^- as the counterion.[74]

3.1.1.1.3   Lyotropic Behaviour

The lyotropic behavior of surfactant **4** in water was initially investigated by optical light microscopy, using a penetration scan. This is a very useful technique, which gives a rapid and general view of the liquid-crystalline behavior of a surfactant.[84,85,86] A small amount of the solid surfactant is placed on a heating stage and compressed between a slide and cover slip. Either the original powder can be employed (as here), or the surfactant is melted, allowed to cool and then used. A drop of water, introduced using a pipette, contacts the surfactant and forms a distinct surfactant/water interface. The solvent slowly diffuses into the sample setting up a concentration gradient. Mesophases are formed in distinct bands as a function of surfactant concentration and temperature and are identifiable by their optical textures and viscosities.

At 25 $^{\circ}$C, upon addition of water to **4**, only an isotropic dilute surfactant solution in contact with the crystalline solid is observed. As the temperature increases by a few degrees (26-27 $^{\circ}$C), a lamellar phase starts to form in the crystal region (Figure 17a, taken at 28 $^{\circ}$C, just after the formation of the lamellar phase) characterized by (i) its birefringent texture when viewed under polarized light, (ii) its medium/low viscosity allowing trapped air bubbles to appear spherical, and (iii) the presence of myelins[87] (Figure 17b). This implies a Krafft

temperature of about 27 °C and is in disagreement with the previous work of Labbé et al., where they state a much higher Krafft temperature of 90 °C.74

The L_α phase shows different types of alignment under the microscope. The director (major axis) alignment is either (i) non-perpendicular to the surface of the glass slide causing the sample to appear birefringent (the optical axis of the L_α phase does not lie in the plane of polarization of the incident light ray) or (ii) perpendicular to the glass slide with the optical axis of the mesophase being in the plane of the polarized light beam, causing the sample to appear black under cross polars (i.e. homeotropically oriented). Along this axis, the lamellar phase appears to be isotropic. This is clearly visible in Figure 17d, e and g, where the L_α phase changes its alignment around the air bubbles, going from being homeotropically oriented to showing birefringence. This is confirmed by the appearance of birefringence upon shearing an aligned sample.
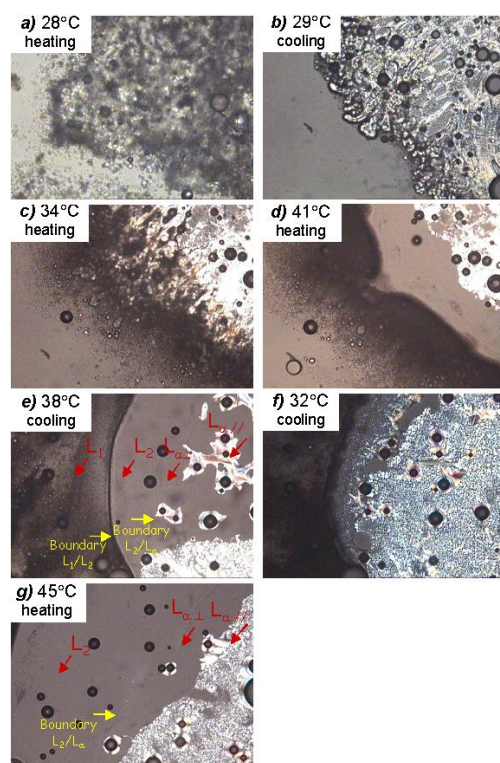

Figure 17: Optical micrographs of surfactant 4 upon addition of water using the penetration scan technique (Magnification ´ 100). A lamellar phase, L_a, starts to form at 27 °C (*a* and *b*). This phase remains in contact with the micellar solution, L_1, until the temperature is 32 °C when another liquid phase appears, an L_2 phase (*c* and, more clearly, *d* and *e*). The L_a has homeotropic orientation at the boundary with the L_2 region: L_a becomes birefringent around air bubbles where it aligns differently (*e* and *g*).

A new phase with low viscosity, appearing black between the crossed polars, starts to form at 32 ^{o}C between the L_1 and L_α regions. This is a second isotropic liquid, labeled L_2 (Figure 17c, d and e). Whilst L_2 is often used to denote the oil phase where an oil and an aqueous phase coexist in the presence of a surfactant[88,89,] here it simply indicates the presence of a second isotropic phase, probably micellar, not fully miscible with water. As the temperature is increased, the lamellar phase is sequentially replaced by the L_2 phase (Figure 17f and g) and disappears at 75 ^{o}C.

The appearance of a second aqueous micellar liquid phase in surfactant water systems is not novel: one common example is the clouding of poly-oxyethylene non-ionic surfactants on heating (a lower consolute temperature).[90,91] Less well known is the frequent observation of "clouding" in zwitterionic surfactants. Systems showing "clouding" above[92] or below[93] a critical temperature are both known. Simplistically, zwitterionic surfactants could be regarded as an ionic surfactant with 100% counterion binding. Thus, one might expect "clouding" in ionic surfactants with hydrophobic counterions. In fact "clouding" is known to occur for the long chain members of an ionic surfactant series, the alkyl-tributylammonium bromides alone with water[94] (a lower consolute loop). The large, partly hydrophobic, headgroup is likely to play an important role. However, in the case here, it is likely that the separation of L_2 is simply because there are no long-range repulsion forces between micelles. Then, only a weak attraction between micelles is required for phase separation. An additional consideration arises from the various micelle shapes that can occur (spheres, rods, discs). The size of the inter-micellar attraction decreases (cloud region decreasing) in the sequence disc > rod > sphere.[91] Since the mesophase is lamellar, the micelles in the most dilute L_2 region are likely to be discs - having the strongest attractions for a given potential. The attractive force is likely to arise from correlations between charges in adjacent micelles, as proposed for zwitterionic surfactants.[95] The observation of "clouding" in this system above the Krafft temperature is fully supported by the light scattering evidence.

In order to obtain a more quantitative phase diagram of **4** in water, samples with surfactant weight fractions of 45, 50, 60, 70, 80 and 90 wt% ($\pm$3 wt%) were investigated by x-ray diffraction at room temperature and 50 $^{\circ}$C. No interference maxima appear in the SAXS patterns recorded for samples up to 60 wt% surfactant, regardless of the temperature. Therefore, it seems that these samples cover the liquid region (L_1 or L_2) that extends up to at least 60 wt% of **4** in water. From 70 wt% onwards, the samples exhibit higher viscosities, although they can still flow easily. The SAXS analysis of the 70 % and 80 % surfactant weight fraction show one interference maximum at $s = 0.35$ nm^{-1} corresponding to a d-spacing of ca. 3.0 nm (data not shown). The interference maximum at ca. $s = 0.35$ nm^{-1} is quite broad, and only at rather high concentrations (beyond 80% surfactant weight fraction) does an additional broad shoulder (s = 0.6-0.7 nm^{-1}) appear, which may be interpreted as a diffuse second order interference maximum. Therefore, the SAXS data does not allow for an unambiguous determination of the nature of the mesophase. While an accurate structural model could not be obtained from the SAXS data, an estimate for the size of the constituting objects was attempted through the use of a basic model involving only a few parameters.

The SAXS data of the mesophases $\geq$70 wt% of surfactant **4** were evaluated in terms of a model of spherical micelles of radius R with a finite distribution of radii (with variance σ_R). Their mutual arrangement was described by a structure factor derived from a hard-sphere potential (Percus-Yevick, "PY", approach).[96] This structure factor is suitable to model "liquid-like" arrangements of objects and is determined only by two physical parameters: the PY radius, R_{PY}, corresponding to the average distance between the spherical objects and the volume fraction, ϕ.

Analysis of the 90 wt% of surfactant **4** sample at RT is shown in Figure 18 as a representative example (similar results were obtained for 70 wt% of surfactant **4** at 50 $^{\circ}$C). It is evident that, although the approach is able to model the data qualitatively with respect to the overall shape, it is unable to account for the SAXS behavior, especially at small scattering vectors. The analysis provides the following: R = 1.7 nm, σ_R = 0.13 nm, R_{PY} = 3.2 nm and ϕ = 0.7; however these values possess a significant variance (certainly of the order of 20-30%), due to the limited quality of the fitting. Despite the inferior quality of the fitting, the analysis

suggests an average object size of *ca.* 3.4 nm, which is in agreement with the model of a micellar L_2 phase, and excludes the possibility of a purely molecular dispersion.
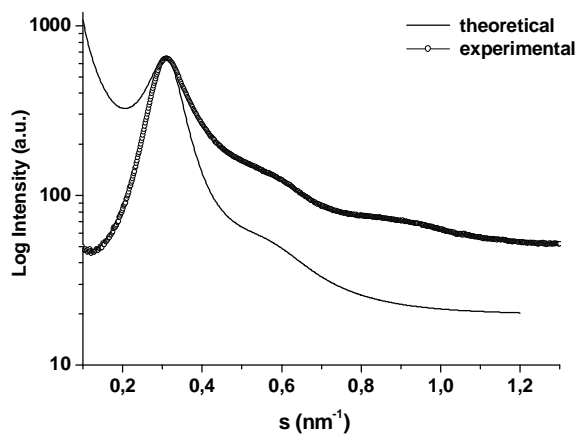

Figure 18: SAXS data (open circles) and modeling (solid line) for 90 wt% of surfactant 4 in water at RT.

The SAXS data also provides an indication that the phase transition from the liquid to the mesophase (L_2/L_α phases) occurs either below 45 wt% or above 90 wt%, since no typical lamellar diffraction pattern is observed in this range of concentration at RT or at 50 ^{o}C. To determine whether the L_α phase occurs at lower concentrations than 45 wt%, or higher than 90 wt%, an investigation was conducted by polarized optical microscopy, so as to establish the occurrence of a L_2 phase at the interface L_α/solid. Indeed, it is not uncommon to find L_2 phases both at higher and lower concentrations than the L_α mesophase and has been reported for poly-oxyethylene non-ionic surfactants with short EO chains.[90,91]

In a new penetration scan experiment, water was added to the solid surfactant at 83 ^{o}C. Upon addition of water, the L_2 phase forms between the L_1 and the solid surfactant, as clearly shown in Figure 19a. Upon cooling, the lamellar phase starts to form at 75 ^{o}C ($\pm$0.5 ^{o}C) and is in contact with the crystals (sequence is crystal-L_α-L_2-L_1).
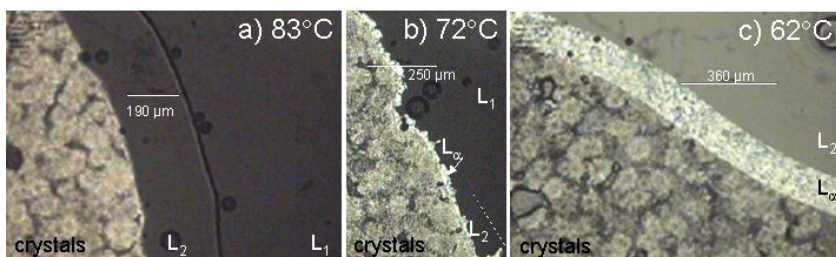
Figure 19: Optical micrographs of surfactant 4 after addition of water using the penetration scan technique. Micrograph *a* shows the occurrence of the L_2 phase in contact with the crystals at 83 °C. Upon cooling, a lamellar phase appears (Micrograph *b* at 72 °C). Thus, the sequence of phases from left to right at 72 °C is crystal/ L_a/L_2/L_1. On cooling the lamellar region extends (Micrograph c at 62 °C). No L_2 phase is observed at the boundary with the solid surfactant.

Careful observation of the crystal/lamellar interface does not show the presence of an L_2 phase (that is, the sequence is not crystal-L_2-L_α-L_2-L_1). This set of results indicates that there cannot be an L_α phase below 45 wt%, and can therefore only occur at concentrations higher than 90 wt% of surfactant **4** in water; these results indicate that the surfactant under study here forms a mesophase only at very high concentrations. Samples from 70 wt% onwards were also investigated by optical microscopy to provide further information on the mesophases formed at RT and 50 °C; all were found to be isotropic between cross polarizers, providing further support of the presence of the L_2 phase at these high concentrations. This outcome is of particular importance especially when this surfactant is to be utilized as a template for self-assembly processes.

3.1.2 Complexation with perylene oligoelectrolyte

The ISA materials were prepared by mixing aqueous 1 %wt solutions of the anionic perylene derivative (**1**) with a solution of either the double-tailed pyrrole-containing surfactant (**4**) or the single-tailed pyrrole-containing surfactant (**6**) yielding complexes **7** and **8**, respectively (Chart 3 - for details see section 5.2.3). Complex **7** is dark purple (similar to the starting dye material), whereas complex **8** is bright red, denoting a difference in the packing of the perylene cores within this complex compared with the pure dye. Both complexes are soluble in chloroform. These self-assemblies were produced with the aim of subsequently

performing a polymerization reaction within confined geometry. This would result in a freezing-in of the structures and would, ideally, lead to conductivity within the materials.
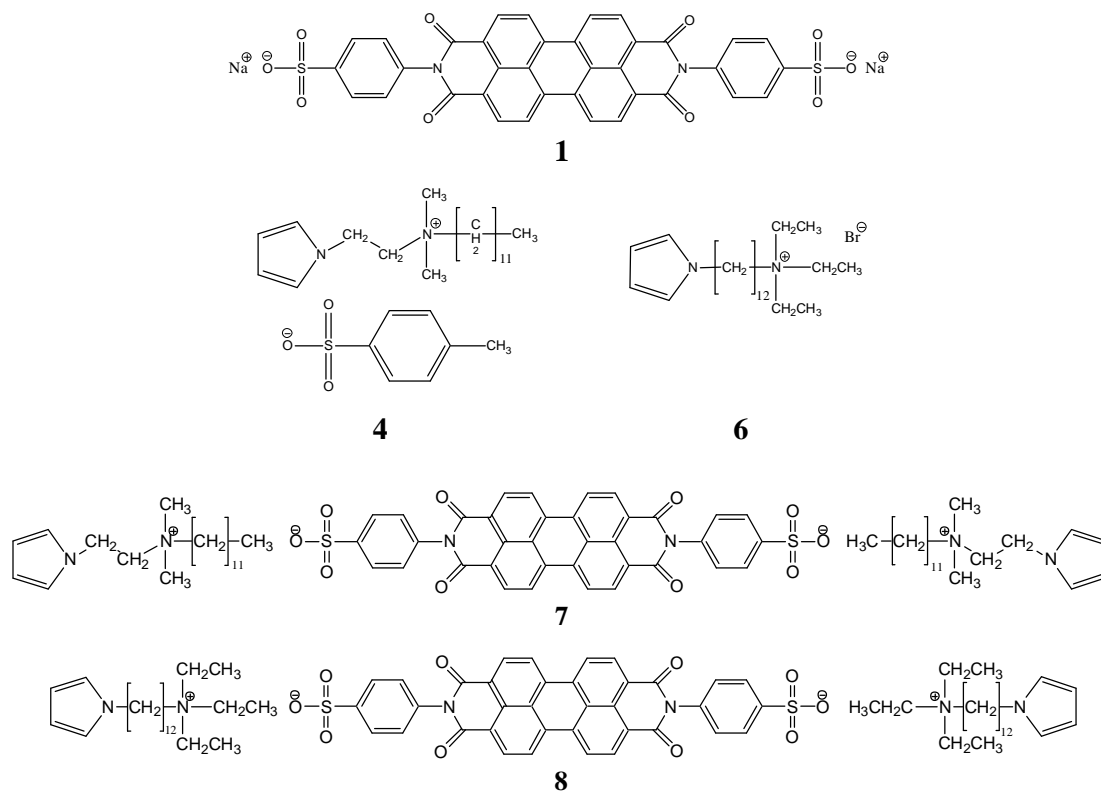

Chart 3: Anionic perylene derivative, N,N'-bis(4-benzenesulphonic acid) perylene-3,4:9,10-tetracarboxyldiimide sodium salt (1); double-tailed pyrrole-containing surfactant, dodecyl-dimethyl-(2-pyrrol-1-yl-ethyl)-ammonium tosylate (4); single-tailed pyrrole-containing surfactant, triethyl-(12-pyrrol-1-yl-dodecyl)-ammonium bromide (6); resulting complexes (7) and (8).

3.1.3 Material Characterization

Thermogravimetric analysis (TGA) revealed that complex **7** degrades above 220 ^{o}C and complex **8,** above 200 ^{o}C. Differential scanning calorimetry (DSC) showed the absence of phase transitions between -80 ^{o}C and 200 or 220 ^{o}C, respectively, for both investigated complexes.

The RT wide-angle X-ray scattering diffractogram of complex **7** (Figure 20a, solid line) is characterized by a diffuse halo at a d-spacing of ca. 0.49 nm, attributed to the liquid-crystalline arrangement of the surfactant alkyl tails. The use of a double-tailed surfactant leads to a large volume fraction of the alkyl tails, lowering possibilities for crystalline packing and therefore exhibiting liquid crystallinity at ambient temperature. The peak at a d-spacing of 0.34 nm is assigned to the regular stacking of the perylene tectonic units. The latter is a typical feature often observed in columnar mesophases arising due to regular π-π stacking of the discotic mesogens.[97,98] X-ray scattering of the material at RT after annealing at 100 $^{\circ}$C for 30 mins resulted in a similar diffractogram (Figure 20a, closed circles) indicating that the material was already in a thermodynamic equilibrium state before annealing, and no structural rearrangement occurred.

The RT X-ray diffractogram of complex **8** exhibited a multitude of relatively sharp peaks, indicating a crystalline structure at this temperature (Figure 20b, solid line). In contrast to complex **7**, annealing at 100 $^{\circ}$C for 30 mins resulted in a structural organization, namely the transformation from a crystalline to a liquid-crystalline material (Figure 20b, closed circles). After annealing, a broad halo originating from the liquid-crystalline arrangement of the surfactant tails is observed at a d-spacing of ca. 0.50 nm. A very weak signal arising from the stacking of the perylene units appeared at a d-spacing of ca. 0.34 nm. This peak is significantly less pronounced than the corresponding peak for complex **7**, indicating that the perylene packing is much weaker in this complex. The structural changes that occur after annealing of the sample implies either that on heating, a metastable state is reached, which then prevails on cooling or that at RT initially the state is metastable and, on heating, a stable state is achieved.
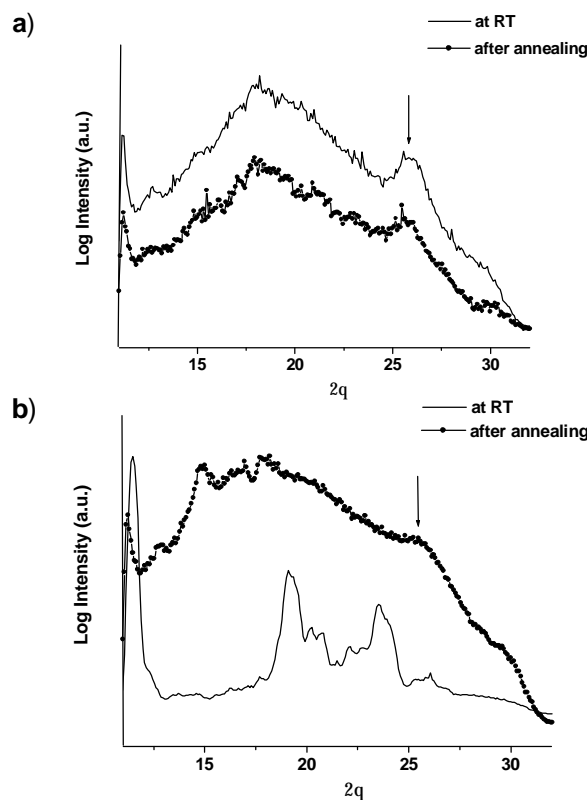
Figure 20: WAXS diffractograms of complex 7 (a) and complex 8 (b) (solid line - at RT; closed circles - at RT after annealing at 100 °C for 30 mins). The arrows indicate the peaks arising from the stacking of the perylene units.

In order to determine the mesoscopic arrangement of the materials, SAXS measurements were performed on the complexes at RT before and after annealing at 100 °C for 30 mins (Figure 21). In the case of complex **7** (Figure 21a) the SAXS diffractograms before and after annealing are practically identical and corroborate the data obtained by WAXS measurements. The occurrence of the narrow reflections present in the small-angle region indicates that the system exhibits a high degree of long-range order. The signals appear at s values of 0.30 nm^{-1}, 0.35 nm^{-1}, 0.46 nm^{-1}, 0.61 nm^{-1}, 0.70 nm^{-1} and 0.92 nm^{-1} and correspond to Bragg spacings of 3.3 nm, 2.9 nm, 2.2 nm, 1.6 nm, 1.4 nm and 1.1 nm. The position ratio of the reflections agreeably coincides with the lattice model for a columnar phase with a 2D orthorhombic structure having dimensions of 3.3 nm and 2.9nm.

In the case of complex **8** (Figure 21b), the RT SAXS diffractogram exhibits only one sharp scattering peak at $s = 0.41$ nm^{-1}, corresponding to a Bragg spacing of 2.4 nm. Due to the absence of a series of reflections, a particular mesophase cannot be assigned to the diffractogram. After annealing of the sample, the diffractogram also exhibits a single peak. This peak, however, is broader than that observed at RT before annealing and appears at approximately 0.27 nm^{-1}, corresponding to a Bragg spacing of 3.7 nm. Although this does not allow for identification of the nature of the mesophase, it indicates that subsequent cooling after annealing, which causes a transformation from the crystalline to a liquid-crystalline phase (as observed from WAXS measurements), results in an increase in the dimensions of the lattice.
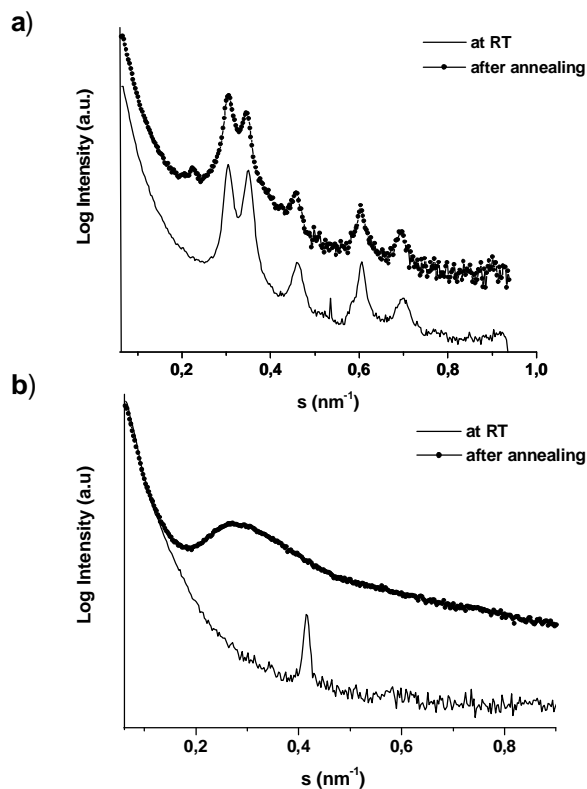

Figure 21: SAXS diffractograms of complex 7 (a) and complex 8 (b) (solid line - at RT; closed circles - at RT after annealing at 100 °C for 30 mins).

Solution ^{1}H NMR and ^{13}C NMR analysis of the complexes in CDCl$_3$ resulted in the appearance of very broad peaks in the spectra, due to the large size and thus, low mobility, of the molecules. As a result, solid-state Cross-Polarization (CP) ^{13}C NMR spectroscopy was performed on the complexes.

The solid-state CP ^{13}C NMR spectrum of complex **7**, annealed at 100 ^{o}C for 30 mins (Figure 22b) exhibits sharp peaks in the range of 5-35 ppm, arising from the carbon atoms of the surfactant alkyl chain together with a broad peak in the range of 115-140 ppm. This broad peak arises mainly from the carbon atoms in the dye phase but also masks the carbon nuclei of the pyrrole rings. The broadness of the aromatic peak in the spectrum of complex **7** is similar to that of the pure perylene dye (Figure 22a) and indicates that the dye phase exhibits low mobility and thus strong packing, corroborating the data obtained by WAXS measurements. The sharp peaks in the spectrum of complex **7,** assigned to the surfactant alkyl carbons, indicate a relatively high mobility of the surfactant phase.

In the spectrum of complex **8**, annealed at 100 ^{o}C for 30 mins (Figure 22c), the signal arising from the dye carbon atoms is more defined than for complex **7** (Figure 22b or the pure dye (Figure 22a), showing that the dye phase exhibits a higher mobility, i.e. a lower degree of packing, and is in agreement with the data obtained by both WAXS and SAXS measurements. The sharp peaks in the spectrum of complex **8,** assigned to the surfactant alkyl carbons, indicate a relatively high mobility of the surfactant phase.
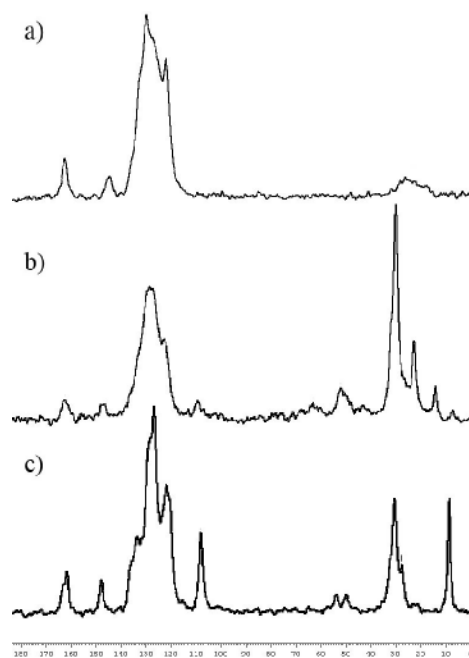
Figure 22: Solid-state CP ^{13}C NMR spectra of the pure perylene dye, 1 (a) and the annealed pyrrole-containing complexes, 7 (b) and 8 (c).

IR spectroscopy was also used in the characterization of complexes **7** and **8**. The spectra of the complexes are very similar and exhibit peaks that arise both from the dye and the corresponding surfactant. The FTIR spectrum of complex **8** is shown as a representative example in Figure 23. The absorptions at 2920 cm^{-1} and 2851 cm^{-1} arise from the surfactant aliphatic CH$_2$ asymmetric stretch, υ_{as}(CH$_2$), and CH$_2$ symmetric stretch, υ_s(CH$_2$), respectively. These FTIR vibrational frequencies are sensitive to the conformation of the alkyl chains and hence can be used as practical indicators of the degree of order within the surfactant phase.[99] When the alkyl chains are highly ordered (all-trans conformation), the bands appear near 2920 and 2850 cm^{-1}, respectively. However, when the alkyl chains are highly disordered, the frequencies tend to shift upwards to ca. 2928 and 2856 cm^{-1}. In the FTIR spectra of the complexes, the positions of these peaks at 2920 and 2851 cm^{-1} indicate that the arrangement of hydrocarbon chains is well ordered (but not necessarily crystalline). RT WAXS analyses (discussed above) showed sharp reflections indicating a crystalline structure only in the case of complex **8**; no sharp reflections were observed for complex **7**. In the WAXS of complex **7**, a broad reflection centred at 0.49 nm corresponding to the lateral packing of the alkyl chains

was observed and is indicative of loosely packed alkyl chains. Thus, the positions of the alkyl stretching vibrations in the IR spectra imply few gauche defects in the complexes.

The peaks appearing in the region of 1450-1420 cm^{-1} arise from C-H bending vibrations of the methyl and methylene groups in the aliphatic component of the complex. The minor peaks appearing above 3000 cm^{-1} result from aromatic C-H stretching of the dye and heteroaromatic C-H stretching of the pyrrole ring. The strong, sharp peak at 1595 cm^{-1} is attributed to the C-C aromatic stretch, whereas the strong peaks at 1714 cm^{-1} and 1671 cm^{-1} result from stretching of the C=O bonds and are characteristic of aromatic imides bonded to two aromatic rings. The absorptions in the region of 900-675 cm^{-1} result from the aromatic C-H out-of-plane bending, absorptions that are most characteristic of polynuclear aromatic moieties. These absorptions are in agreement with the corresponding referenced absorptions.[100] In the IR spectra of the complexes, vibrations arising from the perylene core differ slightly in comparison to the IR spectrum of the pure dye (Appendix, Figure 7). This is expected, for complexation of the dye with the surfactants results in a change of the environment in close proximity of the perylene core.
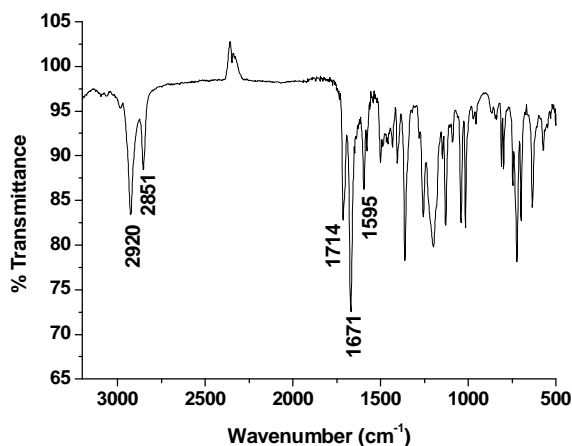

Figure 23: FTIR spectrum of complex 8, resulting from complexation of the perylene dye (1) and the singly-charged pyrrole-based surfactant, triethyl-(12-pyrrol-1-yl-dodecyl)-ammonium bromide (6).

3.1.4 Polymerization

3.1.4.1   Chemical polymerization

The pyrrole-containing complexes, **7** and **8**, were chemically polymerized using FeCl$_3$ as oxidant and HCl as dopant to yield products **9** and **10** respectively (Chart 4 - for details see section 5.2.4.1).
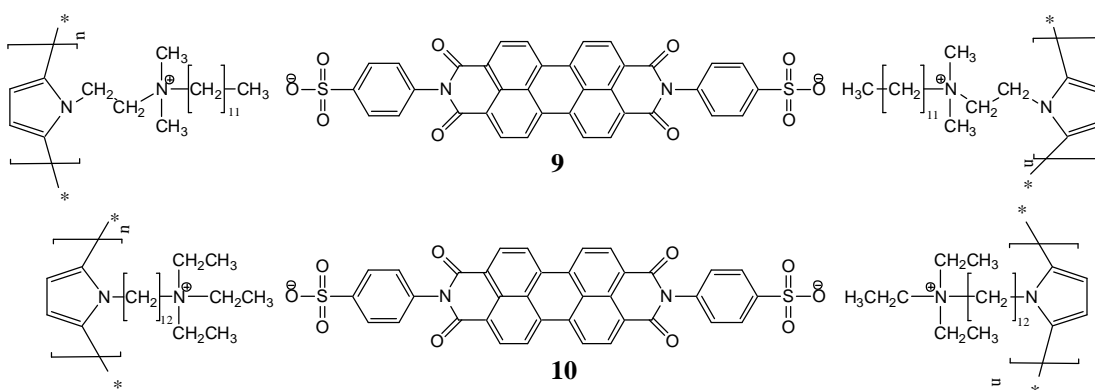

Chart 4: Complexes 9 and 10 resulting from polymerization of the surfactant phase in complexes 7 and 8, respectively.

In contrast to **8**, product **10** exhibits a dark purple colour (Figure 24) and is insoluble in chloroform. Further efforts to identify a solvent for product **10** led to the finding that it is insoluble in common organic solvents. In general, polypyrrole is known to be insoluble and infusible due to strong inter- and intra-molecular interactions and cross-linkings.[53] These changes seem to indicate that polymerization was successful. On polymerization of complex **7** to complex **9**, the dark purple colour is retained and the product exhibits partial solubility in chloroform.
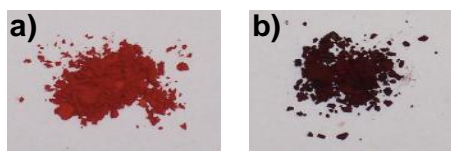
Figure 24: (a) Complex 8 resulting from complexation of the perylene dye (1) and the singly-charged pyrrole-based surfactant, triethyl-(12-pyrrol-1-yl-dodecyl)-ammonium bromide (6); (b) product 10, obtained after treatment of complex 8 with FeCl$_3$ and HCl.

Thermogravimetric analysis (TGA) revealed that **10** exhibits an increased thermal stability compared with the corresponding non-polymerized complex (**8**) (Figure 25). The TGA trace of **9**, however, showed no change in the thermal decomposition curve compared to the non-polymerized material (**7**). Differential scanning calorimetry (DSC) showed the absence of phase transitions between 0 ^{o}C and 200 ^{o}C for both polymerized complexes.
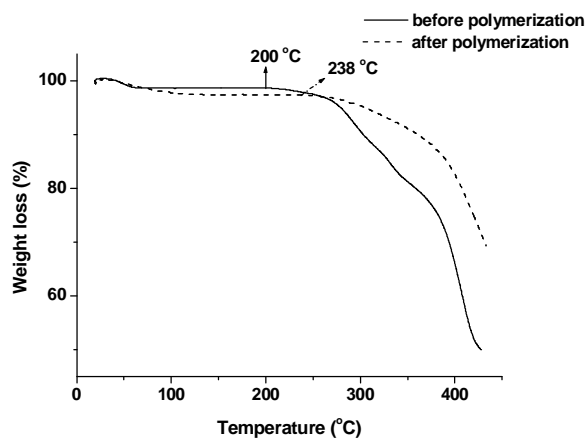

Figure 25: TGA plot of complex 8 (before polymerization – solid line) and the corresponding polymerized material, complex 10 (after polymerization – dashed line) performed at a heating rate of 20 K min^{-1}. The plot shows that the thermal stability of the material increases on polymerization by approximately 38 ^{o}C.

The RT WAXS diffractograms of the polymerized complexes are depicted in Figure 26. In the case of complex **9** (Figure 26a), the peak arising from the regular π-π stacking of the perylene cores appears at a Bragg spacing of 0.34 nm. Both the shape and position of this peak are similar to those found for the corresponding non-polymerized complex, **7** (Figure 20a). The diffuse halo attributed to the liquid crystallinity of the surfactant tails, however, is

much broader (FWHM = 7.6) than for the non-polymerized complex (FWHM = 6.0), indicating an increase in the disorder of the surfactant phase on attempted polymerization.

The RT WAXS diffractogram of product **10** (Figure 26b) shows significant differences to the corresponding non-polymerized, annealed complex, **8** (Figure 20b). A broad peak appears at ca. 0.60 nm (peak A) together with a notably strong peak at ca. 0.36 nm (peak B). Peak B appears at the position normally assigned to the regular π-π stacking of the perylene cores and, thus, suggests that polymerization effects a significant improvement in the perylene stacking.[iii] However, this peak may also arise due to the scattering from pyrrole chains at interplanar spacings close to the van der Waals distance for aromatic groups, as has been previously observed for a poly(pyrrolylium tosylate) polymer.[101] The diffractogram of the polymerized single-tailed surfactant (Appendix, Figure 2), however, only exhibits a broad peak centred at ca. 0.49 nm, assigned to the distance between the alkyl chains, and does not exhibit a peak at 0.36 nm. Thus, in the diffractogram of product **10**, peak B most likely arises from the stacking of the perylene cores. Peak A at a d-spacing of 0.60 nm is assigned to the distance between the surfactant alkyl chains and is larger than that found in the corresponding non-polymerized complex (ca. 0.50 nm). This indicates that the distance between surfactant tectons in the complex increases on polymerization. The distance between the alkyl chains in the polymerized complex is also larger than that found for the polymerized surfactant (Appendix, Figure 2), implying that the polymer produced within confined geometry of the complex has a different structural organization compared to the surfactant polymer.

---

iii Efforts to observe the change in perylene packing on polymerization with UV-Vis spectroscopy were met without success: solid-state measurements gave broad, undefined peaks due to high absorbance of the material, and measurements in solution could not be performed since product **10** was insoluble in all common solvents.
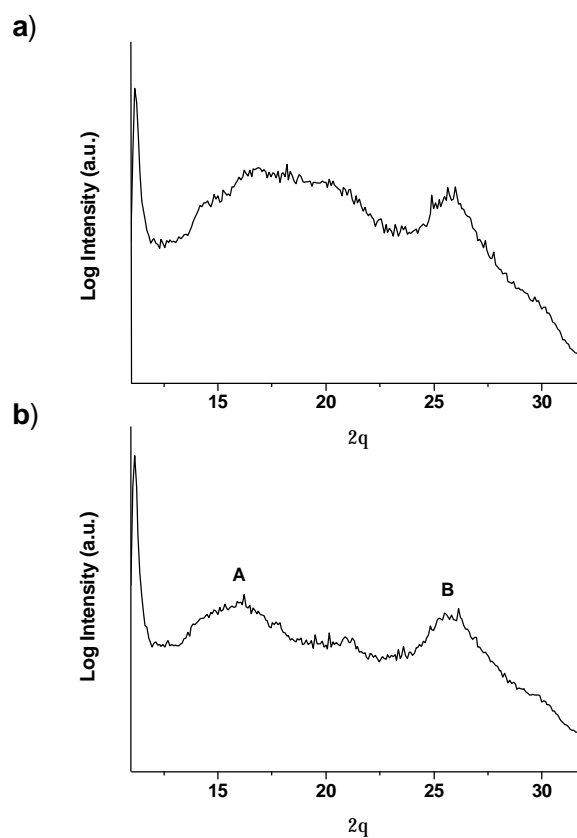
Figure 26: RT WAXS diffractograms of complex 9 (a) and complex 10 (b) obtained after chemical polymerization of complexes 7 and 8, respectively.

The SAXS diffractograms of the polymerized complexes, **9** and **10** (Figure 27) show significant differences compared with the diffractograms of the corresponding non-polymerized complexes (Figure 21). In the case of **9**, the main reflections appear at s values of 0.23 nm^{-1} and 0.30 nm^{-1}, corresponding to Bragg spacings of 4.3 nm and 3.3 nm. Minor peaks are also visible at Bragg spacings of 2.9 nm, 2.2 nm, 1.6 nm and 1.4 nm. The reflection pattern indicates preservation of the columnar phase, observed in the corresponding non-polymerized complex. However, before polymerization, the main peaks appeared at Bragg spacings of 3.3 nm and 2.9 nm, indicating that the dimensions of the lattice increase on polymerization. Also, the peaks are significantly broader than in the case of the non-polymerized complex showing that polymerization effects an increase in the disorder of the phase. Thus, attempted polymerization within the complex leads to the formation of a 1:1 copy of the template, however, with an increased degree of disorder.

In the case of product **10**, the SAXS diffractogram does not exhibit any peaks (Figure 27b) showing that a loss in the long-range order occurs on polymerization. The absence of long-range order is also observed for the polymerized surfactant as well as polypyrrole, synthesised under the same polymerization conditions as for the complexes.
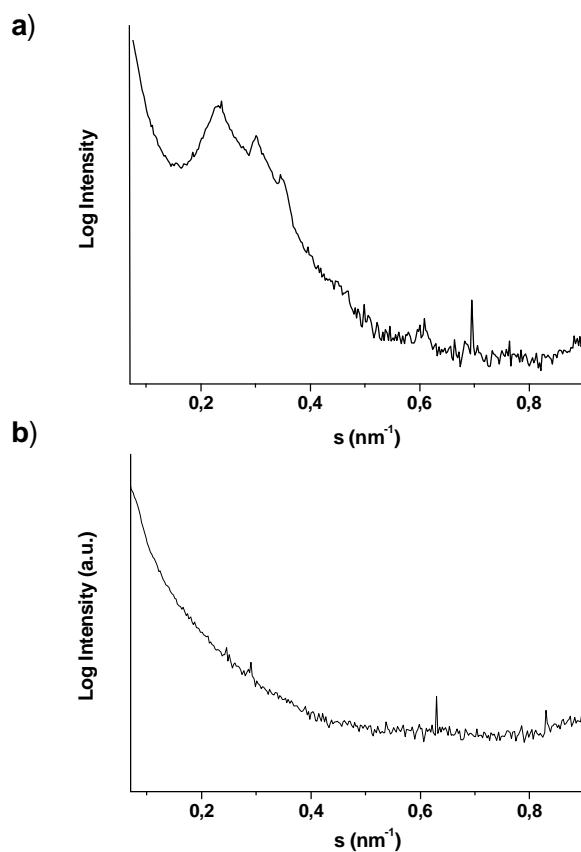

Figure 27: RT SAXS diffractograms of complex 9 (a) and complex 10 (b) obtained after chemical polymerization of complexes 7 and 8, respectively.

The solid-state CP ^{13}C NMR spectra of the polymerized complexes, **9** and **10,** are shown in Figure 28. The spectrum of product **9** (Figure 28a) is similar to that of the corresponding non-polymerized complex (Figure 22b) exhibiting sharp peaks between 5-35 ppm, arising from the surfactant alkyl carbons, and a broad peak between 115-140 ppm, assigned to the aromatic carbons of the dye and pyrrole rings. The sharp peaks in the spectrum of complex **9** assigned to the surfactant alkyl carbons indicate a relatively high mobility of the surfactant phase. The main surfactant peak in the spectrum of complex **9**,

however, is slightly broader (FWHM = 4.2 ppm) than that found in the spectrum of the non-polymerized complex (FWHM = 2.2 ppm), indicating a reduced mobility of the molecules on polymerization. The sharp nature of the surfactant peaks on polymerization can be explained in view of the fact that the pyrrole ring is positioned at the end of the short tail of the double-tailed surfactant and the long C_{12} chain is still relatively free to move after polymerization.

In the spectrum of product **10** (Figure 28b), the signal arising from the aromatic carbons is less defined than for the corresponding non-polymerized complex (Figure 22c) signifying that polymerization results in a decrease of the dye mobility. This is in agreement with the WAXS measurements, which show an improvement in the packing of the perylene cores on polymerization. The signals arising from the surfactant alkyl carbons show considerable differences to those in the non-polymerized complex. On polymerisation, the signals at around 7 ppm and 29 ppm vary significantly in intensity. Also, the peak at 29 ppm is much broader in the spectrum of complex **9** (FWHM = 7.4 ppm) than in the non-polymerized complex (FWHM = 2.2 ppm), indicating a reduction in the mobility of the surfactant phase on polymerization.
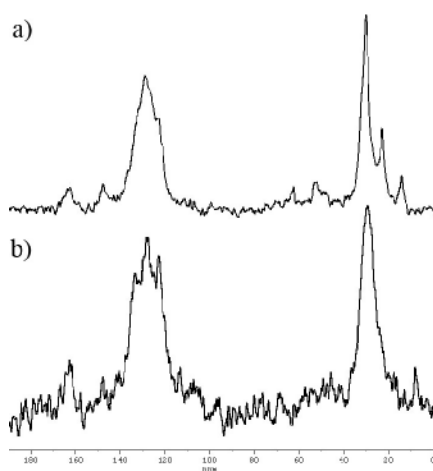

Figure 28: Solid-state CP ^{13}C NMR spectra of the polymerized complexes 9 (a) and 10 (b).

Figure 29 depicts the IR spectra of the polymerized materials in comparison to the corresponding non-polymerized complexes. The most evident change occurs in the region of 1051-1301 cm^{-1} (indicated by the arrows in Figure 29). The changes in the IR spectra on polymerization of the complexes are expected to be due to characteristic vibrations of polypyyrole.
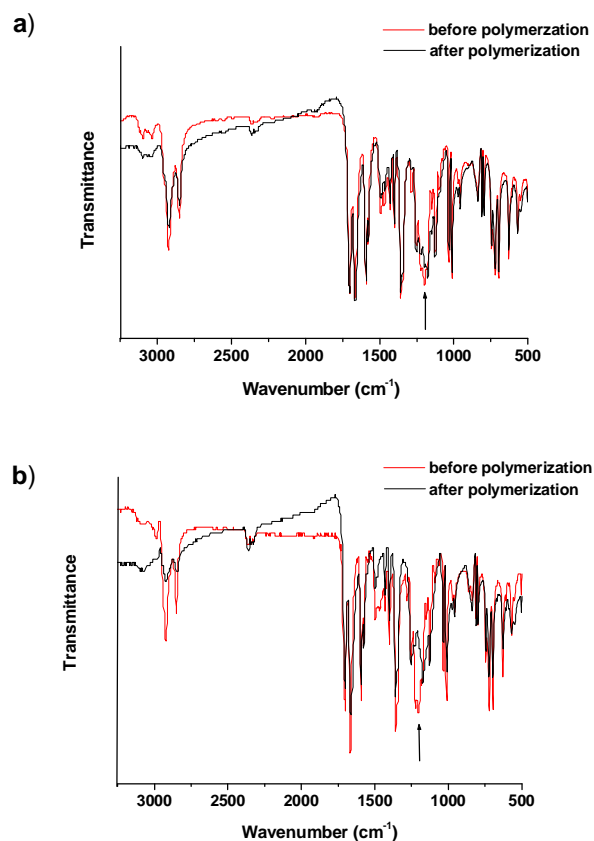

Figure 29: IR spectra (KBr discs) of a) complex 7 (red line) and the corresponding polymerized material, 9 (black line); b) complex 8 (red line) and the corresponding polymerized material, 10 (black line). The arrows indicate the region where the most evident change occurs in the spectra.

The IR spectrum of polypyrrole, polymerized under the same conditions as the complexes, is shown in Figure 30. Polypyrrole exhibits the characteristic bipolaron bands at 1190 cm^{-1} and 920 cm^{-1}.[61b,103] The peak at 1551 cm^{-1} is associated with the ring stretching

vibration of polypyrrole[102] whereas the peaks at 1039 cm^{-1} and 1297 cm^{-1} are attributed to C-H deformation and C-N stretching, respectively.[61b,62c,103] Since the vibrations arising from polypyrrole occur in the region where the complexes exhibit a multitude of strong peaks, it is likely that the polypyrrole peaks are masked in the spectra of the polymerized complexes. The strongest peak in the spectrum of polypyrrole is that at 1190 cm^{-1} and occurs at that position where a change in the IR vibrations is observed on polymerization of the complexes (indicated by the arrows in Figure 29). This change can therefore be assigned to deformation vibrations of the pyrrole rings, that occur on polymerization.[103,104]
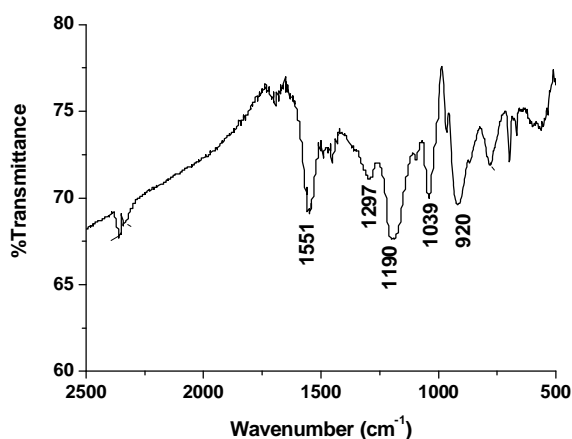

Figure 30: IR spectrum (KBr disc) of polypyrrole.

Since masking of the polypyrrole vibrations occurs by the peaks arising from the complexes, the IR changes that occur on polymerization of the single-tailed pyrrole-containing surfactant were investigated (Figure 31). Polymerization of the surfactant could be verified spectroscopically: after polymerization, the IR absorption band at 750 cm^{-1} in the spectrum of the surfactant is absent in the spectrum of the polymerized surfactant (indicated by the dashed arrow in Figure 31). This band is assigned to the C-H out-of-plane bending at the 2- and 5-position of the pyrrole ring. The disappearance of this band in the IR spectrum of the polymerized surfactant confirms α-α coupling of the pyrrole units in the polymer material. The use of this method as a proof of polymerization has been reported previously.[65a,105] A significant change also occurs in the region of 1051-1234 cm^{-1} (indicated by the solid arrow in Figure 31). A change in this IR region was also observed in the spectra of the complexes on polymerization. The variations in this region are associated with the deformation vibrations of the polypyrrole rings and are, therefore, a supportive evidence of the synthesis of

polypyrrole. In contrast to the spectrum of polypyrrole there is no peak at 1551 cm^{-1} in the spectrum of the polymerized surfactant. Instead there is a sharp peak at 1690 cm^{-1}. This absorption is assigned to the ring stretching vibrations of the pyrrole ring. The shift of this peak compared to that in pure polypyrrole is expected, for the band pattern and relative intensities of this vibration depend on the ring substitution pattern and the nature of the substituents.[100]
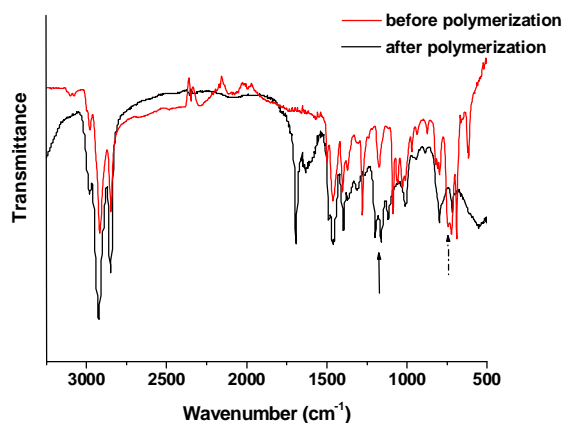

Figure 31: IR spectra (KBr discs) of the single-tailed pyrrole-containing surfactant before (red line) and after (black line) polymerization. The solid arrow indicates the region associated with the ring deformation of polypyrrole; the dashed arrow indicates the vibration assigned to the C-H out-of-plane bending at the α-positions of the pyrrole ring.

3.1.4.2   Electrochemical polymerization

Thin films of complexes **7** and **8** were spin-coated on ITO-coated glass slides and electropolymerized (for details see section 5.2.4.2). On polymerization, the films appeared darker in colour and became insoluble in chloroform. The cyclic voltammetric curves obtained on electropolymerization of complex **8** are shown in Figure 32. The cyclic voltammograms were measured in the range of 0 to 1.2 V vs the Ag/AgCl reference electrode. The complexes exhibited an irreversible oxidation wave at the higher oxidation potentials with a maximum that occurred at ca. 1.2 V, corresponding to the oxidation of the pyrrole rings. In fact N-alkyl pyrroles are known to be oxidized at around 1 V.[106] Since the electropolymerization process was carried out in monomer-free solution, the resulting voltammograms show, from the first scan, an irreversible wave that decreases in intensity and

subsequently vanishes on further scans.[107] The lack of a cathodic wave upon reversal of the potential sweep indicates that the polymers are not subject to reduction in the aqueous buffer medium in the normal potential range for alkylpyrroles. This effect has been previously observed and occurs when the bulky anions originating from the medium remain immobile in the polymer matrix and cannot escape during reduction. [108]
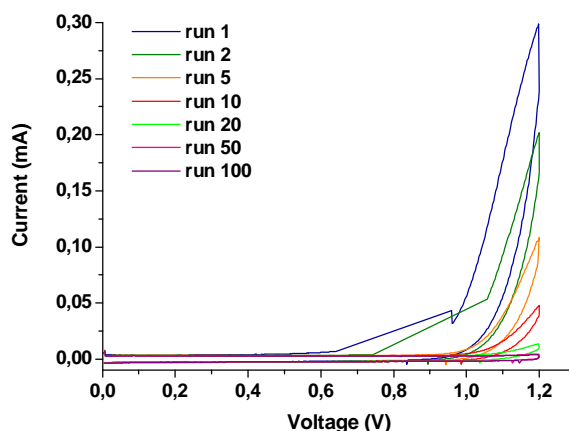

Figure 32: Cyclic voltammogram of complex 8. The voltage is first held at the initial potential of 0 V and is then scanned in the positive direction at a scan rate of 50 mV s⁻¹. Initially, no electrolysis occurs and hence no faradaic current flows. As the voltage increases, the material is oxidised at the electrode surface. At a set value of 1.2 V, the scan direction is reversed and the voltage is returned to the initial value. This potential scan is repeated until oxidation of the sample no longer occurs.

The UV-Vis spectra of the electropolymerized films are shown in Figure 33. The spectra exhibit a strong absorption between 420 nm and 610 nm and a broad absorption with a maximum at 898 nm and 833 nm for the electropolymerized films of complex **7** and **8**, respectively. The absorption between 420 nm and 610 nm results mainly from the π-π transition of the perylene dye but also masks the π-π transition of polypyrrole. The broad band at higher wavelengths results from absorption of polypyrrole.[55c,109]
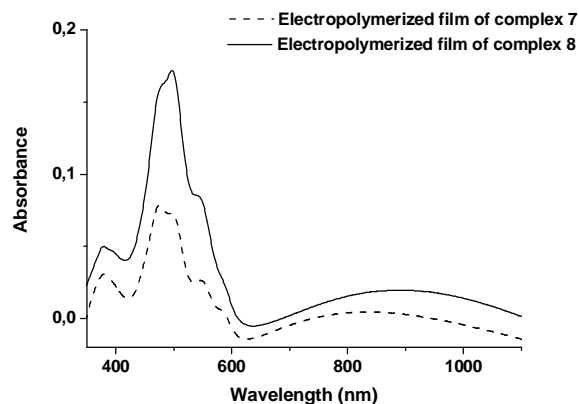
Figure 33: UV-Vis spectra of the electropolymerized films of complex 7 (dashed line) and complex 8 (solid line). The broad band at higher wavelengths is indicative of the formation of polypyrrole.

The electropolymerized films were extremely thin and thus, their removal from the ITO glass plates was not possible. As a result, further analysis of the thin films could not be performed.

3.1.5 Conductive Properties

The reagent molar ratio is a parameter known to affect the conductivity of the final material.[55b,62b] Thus, an investigation of the dependence of the monomer:oxidant:dopant molar ratio on the conductivity of polypyrrole was performed. The results obtained for the conductivity of polypyrrole synthesized using different reagent ratios are summarized in Table 3.

Pyrrole:Oxidant:Dopant	Conductivity ($S\ cm^{-1}$)
1:10:50	3.3 ($\pm$1.3)
1:10:10	0.05 ($\pm$0.03)
1:1:50	0.05 ($\pm$0.02)
1:1:10	0.5 ($\pm$0.3)
1:1:1	0.6 ($\pm$0.3)

Table 3: Conductivity values of polypyrrole obtained by polymerization of pyrrole at various monomer:oxidant:dopant ratios.

Since the monomer:oxidant:dopant molar ratio of 1:10:50 was found to give the polymer with highest conductivity (ca. 3.3 S cm^{-1}), the polymerization of complexes **7** and **8** was conducted using this ratio. The resulting complexes, however, were not dark in colour and still soluble in chloroform indicating that the polymerization was unsuccessful. This was confirmed by the fact that the obtained samples were non-conducting. Thus, synthethic parameters that are adequate for the polymerization of pyrrole to give a conducting polymer may not necessarily be the case for polymerization of substituted pyrroles. This is probably a consequence of the difference in reactivity of the monomers.

Since the lower reactivity of the complex samples compared with unsubstituted pyrrole is likely to be a reason for the low conductivity, we decided to conduct the polymerization in an increased amount of oxidant. The selected monomer:oxidant:dopant molar ratio was 1:50:50. The powdered samples turned dark in colour and exhibited parital or complete insolubility in chloroform indicating that the polymerization was successful. These samples were characterized as described in section 3.1.4.1. The powdered samples were tested for conductivity and were found to be non-conductive (Table 4).

Sample	Conductivity
Polypyrrole	3 x 10^{-5} S cm^{-1}
Polymerized single-tailed surfactant	2 x 10^{-6} S cm^{-1}
Complex **9**	Non-conducting
Complex **10**	Non-conducting

Table 4: Measured conductivities of polypyrrole, the polymerized single-tailed surfactant and the polymerized complexes, 9 and 10. Polymerization was performed using FeCl$_3$ and HCl at a monomer:oxidant:dopant molar ratio of 1:50:50.

Complexes **7** and **8** were then polymerized using iodine vapour, which acts as both oxidant and dopant.[50,65a] Although complex **7** polymerized with iodine was found to be weakly conductive (resistivity = 190 MOhm), complex **8** exhibited a conductivity of 10^{-6} S cm^{-1}. This value is low compared with the general conductivities of unsubstituted pyrrole or pyrroles substituted at the β-positions. However, it is comparable (albeit lower) to the conductivity values of similar pyrrole-based polymers, which are reported in the range of 10^{-4}

- 10^{-5} S cm^{-1}.[50,65a,110] The low conductivity of the polymerized ISA materials is a consequence of the situation of the substituent at the N-position of the pyrrole ring[52] and the steric bulk of this substituent that acts both to separate the pyrrole chains, slowing the rate of electron hopping, and to reduce the polymer conjugation length through chain twisting.[65a] Low conductivity probably also results from the formation of non-linearly aligned polymer chains due to polymerization in 3D geometry.

3.1.6 Conclusion

In this study we explored the ISA approach using truly functional surfactants as building blocks in the design of supramolecular functional materials. This firstly required the synthesis of such functional surfactants - the target molecules adopted were a single-tailed and a double-tailed N-substituted pyrrole monomer. Owing to the presence of the pyrrole moiety, these surfactants are not only polymerizable but are also potentially conductive when polymerized. Since routine characterization analysis of the double-tailed pyrrole-containing surfactant indicated a very interesting, complex phase behaviour, a comprehensive investigation into the phase properties of this surfactant was conducted. The pyrrole-derived surfactants were then employed in the synthesis of ISA materials by complexation with a perylene-based dye. The self-assembled materials were characterized and, through the presence of the polymerizable moiety within the surfactant molecule, subsequently polymerized by both chemical and electrochemical methods. This polymerization reaction within confined geometry led to a decrease in the structural order of the molecular self-assemblies but affected an increase in the conductivity of the resulting materials. The results of this study show that, through the use of functional surfactants, functional nanostructures can be obtained by the ionic self-assembly (ISA) strategy. Thus, the use of oppositely charged tectons not only provides the possibility for facile synthesis of self-organising materials, but also the chance to use this method as a toolbox for the production of functional materials.

3.2 Lysine-based surfactants

3.2.1 Synthesis

With the aim of inducing chirality in perylene assemblies, two chiral surfactants were synthesized (for details see section 5.2.1.3). The surfactants carrying one (**13**) or two (**14**) protonated ammonium head groups for complexation with an anionic perylene derivative, were synthesized starting from a lysine (lys)-based salt (Scheme 6). By using orthogonal protecting groups for the terminal α- and ε-amines, both **13** and **14** were synthesized from the same intermediate **11**. Compound **11** was synthesized by reaction of N-α-(Z)-lys-N-ε-(Boc)-OH with hexadecanol. After column chromatography, the Boc-group could be selectively removed by acid treatment yielding an amphiphile with a single protonated head group (**13**). Selective Z-group deprotection by hydrogenation of **11**, resulted in **12**, which, after Boc deprotection, yielded a surfactant with two head groups (**14**).
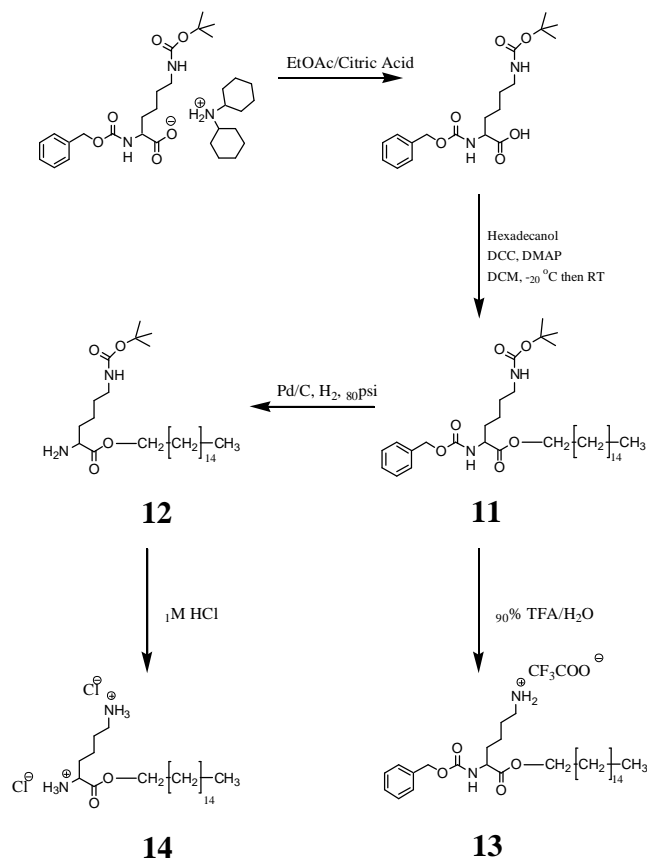
Scheme 6: Synthesis of the chiral surfactants, 5-benzyloxycarbonylamino-5-hexadecyloxycarbonyl-pentyl-ammonium trifluoro-acetic acid salt (13) and 1-hexadecyloxycarbonyl-pentylene-1,5-diammonium dichloride (14).

3.2.2 Complexation with perylene oligoelectrolyte

The ISA materials were subsequently prepared by mixing aqueous 1 %wt solutions of the anionic perylene derivative **1** with a solution of either the cationic surfactant **11** or **12** yielding complexes **13** and **14**, respectively (Chart 5 - for details see section 5.2.3).
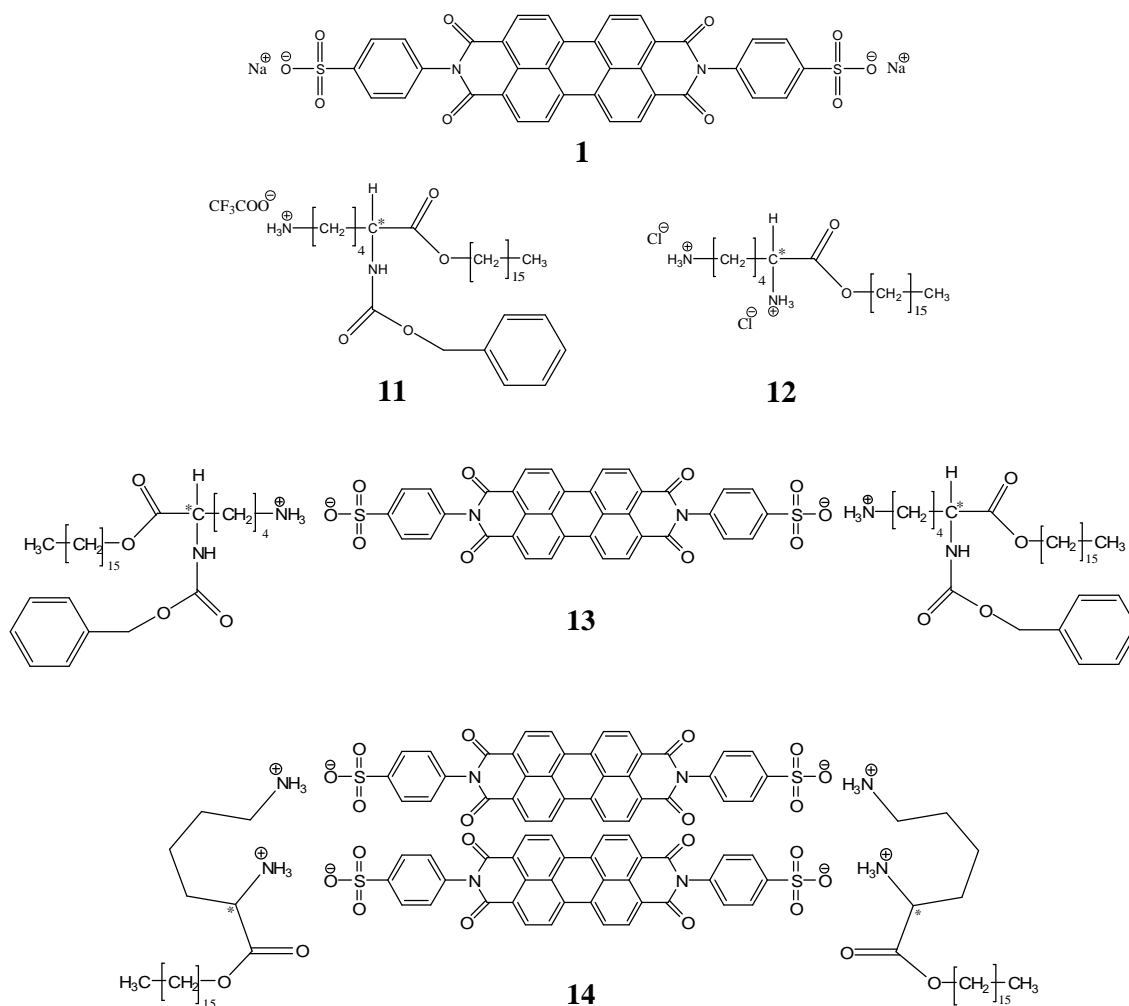

Chart 5: Anionic perylene derivative, N,N'-bis(4-benzenesulphonic acid) perylene-3,4:9,10-tetracarboxyldiimide sodium salt (1); singly-charged chiral surfactant, 5-benzyloxycarbonylamino-5-hexadecyloxycarbonyl-pentyl-ammonium trifluoro-acetic acid salt (11); doubly-charged chiral surfactant, 1-hexadecyloxycarbonyl-pentylene-1,5-diammonium dichloride (12); resulting complexes (13) and (14).

3.2.3 Film Characterization

3.2.3.1   UV characterization

The UV-VIS absorption spectra of complexes **13** and **14** in solution at RT were identical and that of complex **14** is shown in Figure 34a as a representative example. These spectra, however, differ significantly from that of the pure perylene dye **1** (Figure 34b). The spectrum of **1** is characterized by two absorption maxima at 501 nm (band B') and 546 nm (band C'), together with a broad shoulder at ca. 472 nm (band A'). The peaks correspond to the S_0-S_1 electronic transition superimposed with vibrational transitions.[111] According to the molecular exciton model, since the higher energy band B' (501nm) is of higher intensity than the lower energy band C' (546nm), the dye molecules adopt a parallel, stacked geometry.[112]

Upon complexation of the dye with the chiral surfactants **11** and **12**, pronounced changes occur in the UV-VIS spectrum (Figure 34a). The strong absorption band at 501 nm is still present in the spectra of the complexes (Band B'). The weaker band C' at 546nm in the spectrum of the pure dye undergoes a bathochromic shift of 8 nm to 554 nm on complexation (Band C), implying that this transition requires less energy. The shoulder observed at 472 nm in the spectrum of the pure dye (Band A') is strongly enhanced and slightly shifted in the spectra of the complexes, appearing as a peak at 476 nm (band A). The intensity ratio of bands A, B and C change from 1.2:1.9:1 in the dye to 2.5:2.2:1 in the complexes. Furthermore, a new peak appears in the spectra of the complexes at 586 nm (band D). This absorption is caused by resonance interactions between the transition dipoles in the aggregated state,[113] clearly indicating a different mode of packing for the complexed dyes compared with the pure dye (see below).

Solid-state spectra of the complexes as thin films at varying concentrations (20, 40, 60 and 80 mg mL^{-1}) were found to be identical to those in THF solution, indicating that the aggregation of the dye units in the films at these concentrations is comparable to that in solution (see below for more details; for the UV spectra see Appendix, Figure 3). Thermal treatment (to 50 °C, see section 3.2.3.3 on the thermal properties of the complexes) did not result in changes in the UV spectra (i.e. the complexes were already in a thermodynamic equilibrium state before annealing, and no rearrangement of the dye organisation took place).
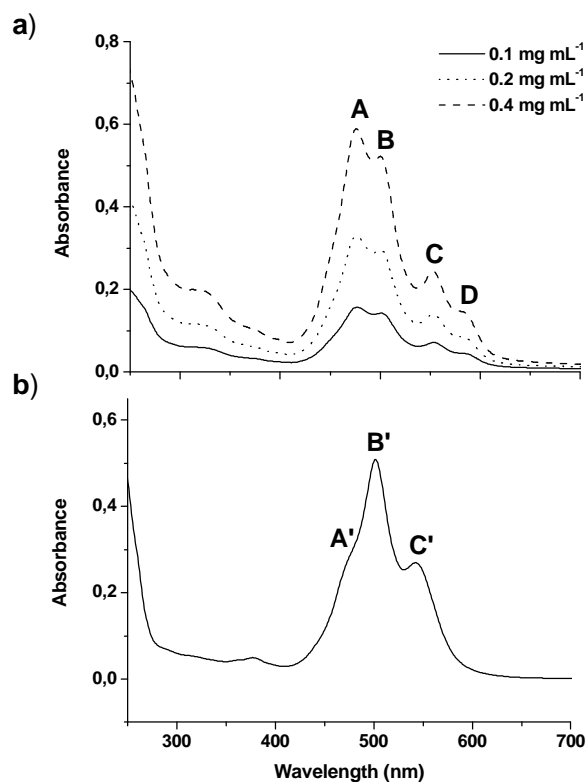
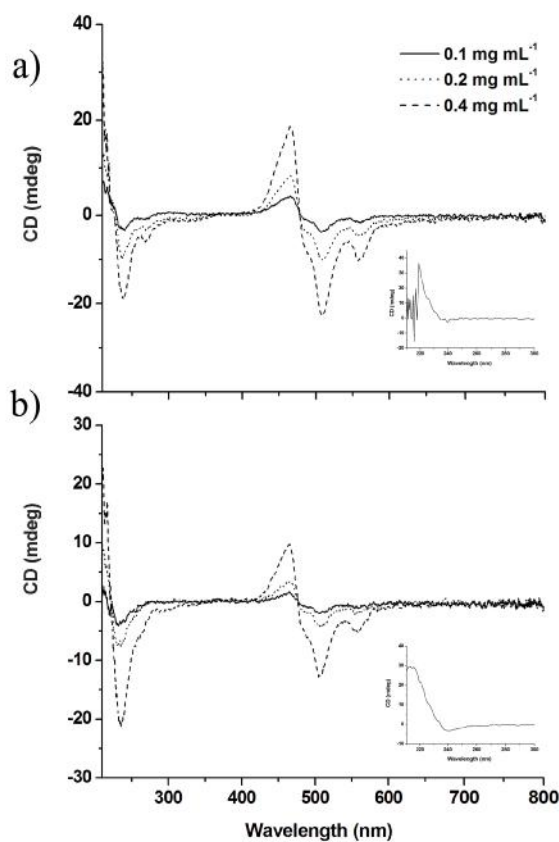**Figure 34: a) UV-VIS spectra of complex 14, in THF at varying concentrations. The spectra do not show changes in the optical properties upon concentration variation, at least within the range of concentration measured; b) UV-VIS spectrum of the pure dye (1) in the aggregated state (0.2 mg mL^{-1} in H$_2$O).**

3.2.3.2   The induction of chirality

In order to investigate the possible expression of chirality within the aggregates and, thus, gain more information on the structure of the assemblies, circular dichroism (CD) measurements were performed on 0.1 - 0.4 mg mL^{-1} solutions of the complexes (Figure 35). Although the pure surfactants **11** and **12** both gave rise to positive Cotton effects at around 220 nm (Figure 35, insets), the corresponding complexes **13** and **14** displayed a bisignate Cotton effect in the absorption range of the surfactants. More importantly, a strong bisignate Cotton effect was present in the absorption region of the perylene dye indicating that, upon complexation, the chirality of the surfactant indeed becomes expressed in the bisimide chromophore.

In the CD spectra of both complexes, the perylene band exhibits a crossover at 476 nm, which corresponds to the absorption maximum as found for the UV spectra recorded in solution. The bisignated CD signals are indicative of chiral excitonic couplings that arise when the chromophores are aggregated in close proximity with their transition dipoles oriented in a helical fashion.[8,68a,114] The negative sign of the couplet, characterized by the signal change from positive to negative with increasing wavelength, indicates a left-handed or counter clockwise helical arrangement of the transition dipoles.[8,68,115] Thus, the chiral information of the surfactant is transferred to the perylene stacks leading to a left-handed helical stacking of the molecules.

Figure 35: CD spectra of complex 13 (a) and complex 14 (b), in THF at varying concentrations. The spectra do not show changes in the optical properties upon concentration variation, at least within the range of concentration measured. The insets show the CD spectra of the corresponding pure surfactants in THF at a concentration of 2.5 mg mL^{-1}. The CD spectra are plotted from 210 nm since THF absorbs below this wavelength.

The CD spectra of spin cast films of the complexes **13** and **14** (Figure 36) showed significant differences to the CD spectra in solution (Figure 35). For thin films, the CD spectra displayed strong Cotton bands at low wavelengths coinciding with the UV absorptions of the surfactants together with significantly smaller Cotton effects at 475 nm and 500 nm, corresponding to the two UV-VIS absorption maxima found before. The bands, however, were not bisignate as those observed in the solution CD spectra. The CD spectrum of the pure perylene dye as a thin film, formed by drop-casting of a 2.5 mg mL^{-1} aqueous solution, exhibited no peaks in the perylene absorption region.

The intensity of the positive and negative bands resulting from exciton coupling of two identical chromophores can be described by the following equation:[116]

$$\Delta\varepsilon = \pm\, \pi/(4\lambda)\ \mu_a\, \mu_d\, R_{da}^{-2}\, \sin(2\theta) \tag{9}$$

where μa and μd are the electronic transition dipoles of the two chromophores, R_{da} is their centre-to-centre transition and θ is the angle between their transition dipoles. The factor of $\sin(2\theta)$ results in zero intensity when theta = 0, 90 or 180° and maximum intensity when theta = 45 or 135°. The very low CD intensity of the perylene signal in the spectra of the thin films suggests a dimer geometry in which the perylene long axes are aligned, i.e., the preferred geometry for unconstrained perylene aggregates. The much larger CD intensity for the perylene signal in solution is therefore clearly indicative of a non-aligned geometry.
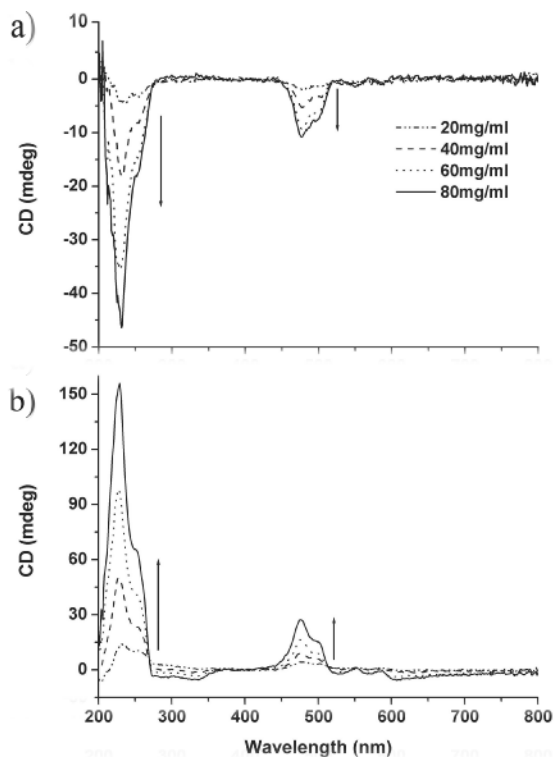
Figure 36: CD spectra of complex 13 (a) and complex 14 (b), spin-cast from solutions of varying concentrations. The spectra do not show changes in the optical properties upon concentration variation, at least within the range of concentration measured. The arrows indicate increasing complex concentration.

A further significant observation from the CD spectra of complexes as thin films was that, although the pure surfactants **11** and **12** both gave rise to positive Cotton effects (Figure 35, insets), the corresponding complexes **13** and **14** did not both display positive Cotton effects. Whereas complex **14** displayed a positive Cotton effect at low wavelength, complex **13** displayed a negative Cotton effect, opposite to that of the original surfactant (Figure 36a).[iv]

With the structure of the complex in solution elucidated, we aimed to obtain insight into the molecular organization of the complexes in the solid state.

---

iv It is important to note that this reversal of sign does not necessarily indicate a corresponding reversal in the organization of the stacks. A reversal of sign in the CD effect has, for example, also been observed upon saponification of the side chains of poly(isocyanides), see reference 117.

3.2.3.3   Structural analysis

Thermogravimetric analysis (TGA) revealed that both **13** and **14** degrade above 125 ^{o}C. Differential scanning calorimetry (DSC) showed that **14** exhibited no transitions between -20 ^{o}C and 125 ^{o}C whereas **13** showed a broad endothermic transition at ca. 28 ^{o}C upon heating. This transition was reversible as indicated by the appearance of an exothermic peak on the cooling curve at ca. 21 ^{o}C (Figure 37).
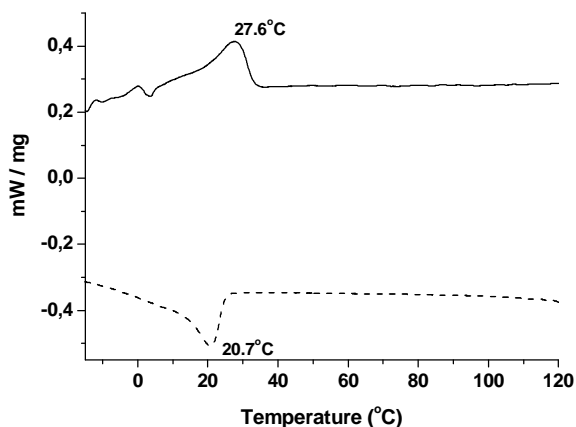

Figure 37: DSC plot of complex 13 performed at a heating/cooling rate of 10 K min^{-1} (solid line - 2nd heating curve; dashed line - 1st cooling curve).

Temperature-dependent wide angle X-ray scattering performed on **13** at RT, 50 ^{o}C and again at RT in all cases indicated a stacking of the perylene tectonic units at a d-spacing of approximately 0.35 nm, as well as a liquid-crystalline arrangement of the surfactant tails at a d-spacing of 0.48 nm. Further cooling to 0 ^{o}C revealed a slight narrowing of the surfactant halo as well as a decrease in the average d-spacing (from 0.48 nm to 0.42 nm, see Figure 38a). From this, it can be concluded that the transition observed in the DSC is due to an increase in the order of the alkyl phase at low temperature.

FTIR vibrational frequencies of the CH_2 asymmetric stretch, $\upsilon_{as}(CH_2)$, and the CH_2 symmetric stretch, $\upsilon_s(CH_2)$, are sensitive to the conformation of the alkyl chains and hence can be used as practical indicators of the degree of order within the surfactant phase.[99] When the CH_2 groups in a polymethylene chain are in the all-trans conformation, the bands appear near 2920 cm^{-1} and 2850 cm^{-1}, respectively. However, when the alkyl chains are highly

disordered, the frequencies generally shift upwards to ca. 2928cm^{-1} and 2856 cm^{-1}. In the FTIR spectrum of complex **13**, the $\upsilon_{as}(CH_2)$ band appears at 2922cm^{-1} and the $\upsilon_s(CH_2)$ band at 2851 cm^{-1}, implying few gauche defects in the arrangement of the hydrocarbon chains (Appendix, Figure 4). This would strongly suggest that a so-called alkane rotator phase is present at lower temperatures. This phase is characterized by rotational freedom of the alkyl chains, however with restricted lateral movement[118] and fits very well with the obtained WAXS and IR data.

The X-ray diffractograms of **14** obtained at RT, 50 °C and again at RT, in all cases indicated a stacking of the perylene tectonic units at a d-spacing of approximately 0.35 nm, as well as a liquid-crystalline arrangement of the surfactant tails at a d-spacing of 0.48 nm (Figure 38b).
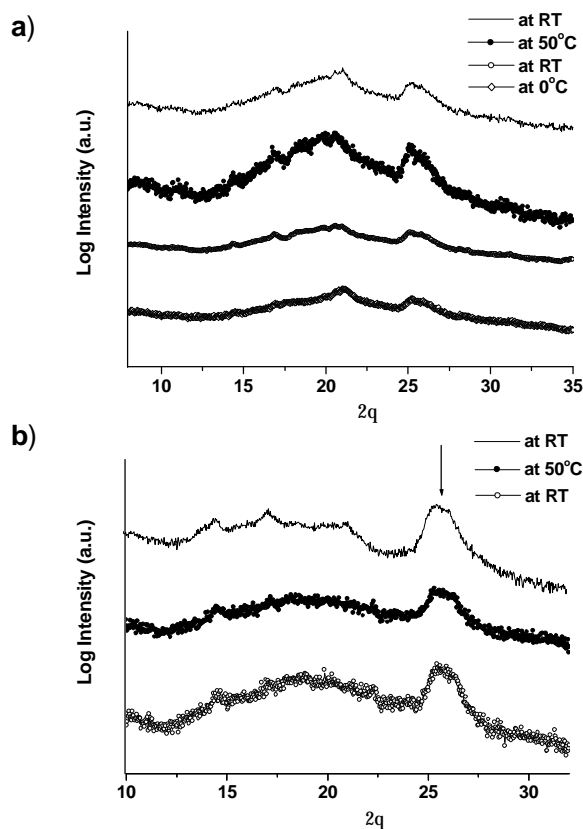
Figure 38: Temperature-dependent WAXS of complex 13 (a) and complex 14 (b) performed at a heating/cooling rate of 10 K min^{-1} (solid line - at RT; closed circles - at 50 °C; open circles - at RT after heating to 50 °C; open diamonds – at 0 °C after heating to 50 °C). The arrows indicate the peaks arising from the stacking of the perylene units.

In order to determine the mesoscopic arrangement of the materials, SAXS measurements were performed at RT and at 50 ^{o}C (Figure 39a and b). For both complexes and at both investigated temperatures, only one major peak was observed in the scattering diagram. In addition, the diffractograms of the complexes at 50 ^{o}C displayed small higher order peaks, which were difficult to observe in the RT diffractograms. The scattering peaks were indexed to a lamellar phase (the arrows in Figure 39a and b indicating the higher order reflections) with a d-spacing of 5.5 nm and 4.6 nm at RT for **13** and **14**, respectively. Thus, at both RT and at 50 ^{o}C, both complexes are in a highly ordered thermotropic liquid-crystalline state.[119] The arrangement of molecules shows the characteristics of discotic lamellar ordering and, although low in intensity, several higher-order reflections are found. The large number of higher order reflections signifies that a very regular repetition of the layers exists, despite the fact that this is solely based on noncovalent interactions.
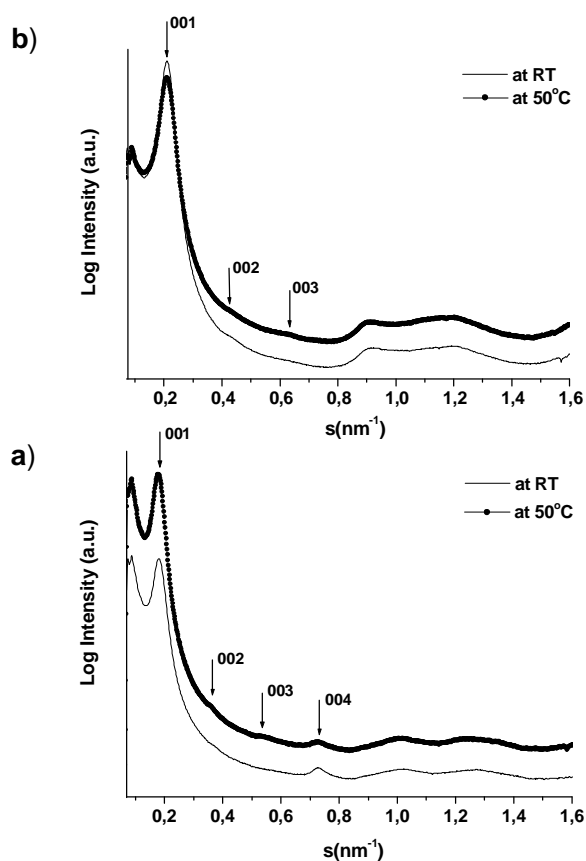

Figure 39: Temperature-dependent SAXS of complex 13 (a) and complex 14 (b) (solid line - at RT; closed circles – at 50 ^{o}C). All diffractograms show a major peak and higher order peaks that are indexed to a lamellar phase.

The thickness and the film-forming properties of both spin-coated complexes were studied by tapping mode AFM. For both complexes and at all investigated concentrations, a Schlieren texture was observed (Appendix, Figure 5 for complex **13** at 80 mg mL^{-1}). The mean thickness (at the centre and edges of the films) was determined by a scratch test and, as expected, increases with increasing concentration (Appendix, Table 1).

3.2.4 Molecular Modeling Studies

From the d-spacings determined by X-ray measurements, a computer generated structural model for the intermolecular ordering of the two complexes was derived. The model for complex **13** is presented in Figure 40. This model indicates a layered or smectic ordering in one dimension: the layer of perylene cores is separated from the next layer of perylene cores by the alkyl chains. In the case of **13**, the length of the model complex is 5.4 nm[120] and is in very good agreement with the length obtained from X-ray measurements (5.5 nm). In the model system for complex **14**, where the alkyl chains are in an all-trans conformation and a slight interdigitation of alkyl chains (over approximately 4 C-C bonds) is predicted, the length of the repeat unit (corresponding to the 'a' distance in Figure 40) is approximately 4.4 nm in length[120] and is also in close agreement with the obtained X-ray data. The distance between the perylene cores in adjacent stacks, which corresponds to the 'b' distance, is found to be 0.35 nm in the structural models of both complexes, and corroborate the values obtained from X-ray measurements.
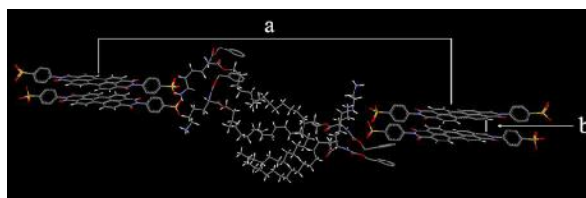

Figure 40: Structural model for the intermolecular ordering of the complex 13. The length of the complex molecule ('a') is found to be ca. 5.4 nm, while the distance between the perylene cores ('b') is ca. 0.35 nm. These values are in agreement with the corresponding distances obtained from X-ray diffraction measurements.

Figure 41, a model obtained after optimising the packing of 72 molecules of complex **13** using UFF energy minimisation,[120] provides an indication of how the transfer of chiral information from the surfactant to the supramolecular assemblies might lead to a viable low energy arrangement of the complexed dyes. These results, however, are only preliminary in nature and do not provide any conclusive evidence to explain the origin of the transfer of chirality.
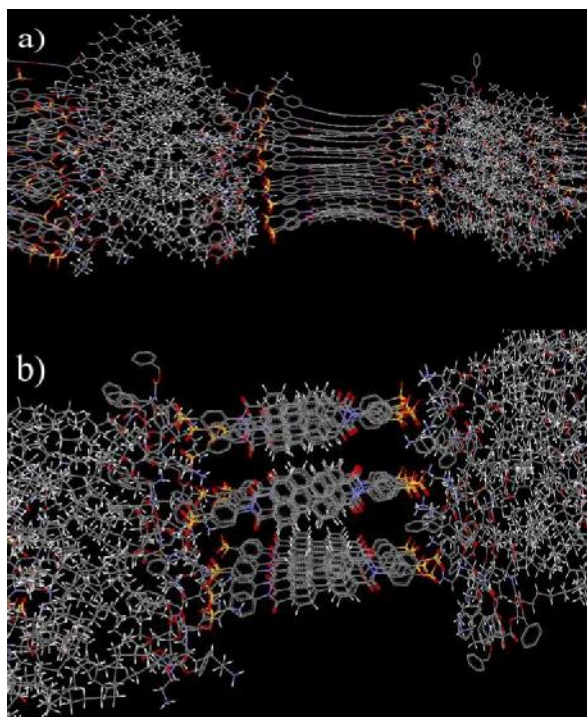

Figure 41: Molecular arrangement of the energy-minimized complex 13 system determined using universal force field (UFF) calculations:[120] (a) view along the stacking direction (side view) showing that the perylene molecules are non-planar, despite the absence of bay-substituents; (b) view at an axis 90° to the stacking direction (top view) showing a twist of the perylene cores.

3.2.5 Conclusion

In this investigation we presented a proof-of-principle study to show that chirality can be transferred from low molecular chiral tectons into supramolecular assemblies through ionic interactions, in both the solution and solid state. It was shown that complexes are organised into a left-handed helical arrangement in solution. Since it is possible to tune the materials properties and characteristics of such ionically self-assembled materials through the choice of

the starting materials, it has enabled us to produce low molecular weight chiral liquid-crystalline materials using this strategy. This opens a wide variety of opportunities for the production of functional chiral materials for application in display technologies (e.g. for the production of polarised emission) as well as possible applications as chiral sensing materials. The induction of chiral effects opposite in sign to that of the starting materials offers an intriguing possibility for the production of dynamic switchable materials.

4   SUMMARY AND OUTLOOK

The present work describes a modular synthetic approach towards supramolecular systems with integrated functionality. Basic supramolecular concepts were applied for the noncovalent synthesis of supramolecular entities, with the ultimate objective being the introduction of functions in such ordered structures. Since the ionic self-assembly (ISA) strategy has proved to be a facile method for the production of liquid-crystalline materials, we continued investigations into the phase behaviour, physical properties and function of a variety of ISA materials, comprising a perylenediimide derivative as the employed oligoelectrolyte. Functionality was introduced into the materials through the use of functional surfactants.

The distinctive functionality of polypyrrole motivated us to design and synthesize pyrrole-derived surfactant monomers as building blocks for use in ISA materials. Owing to the presence of the pyrrole moiety, these surfactants are not only polymerizable but are also potentially conductive when polymerized. We adopted single-tailed and double-tailed N-substituted pyrrole monomers as target molecules. Although polymers derived from such pyrroles generally exhibit lower conductivity than those derived from monomers substituted at the β-position, the synthesis of N-substituted monomers is considerably easier and the symmetry of the resultant species is more conducive to the formation of ordered phases.

Since routine characterization analysis of the double-tailed pyrrole-containing surfactant indicated very interesting, complex phase behaviour, we conducted a comprehensive investigation of the properties of this surfactant. The Krafft temperature was found to be ca. 27 ^{o}C and the critical micelle concentration (cmc) at 40 ^{o}C ca. 1 mM, as obtained from surface tension, potentiometry and isothermal titration calorimetry measurements. The lyotropic behavior of the surfactant was found to be of a complex nature. At concentrations higher than the micellar (L_1) region, two mesophases were identified: a second isotropic (L_2) phase, which is probably micellar but not fully miscible with water, and a lamellar (L_α) phase. Light scattering, modeling of X-ray data and the observation of high viscosity solutions by light

microscopy, suggest the formation of large self-assembled aggregates. The nature of these aggregates is subject to future characterization by cryo-TEM and neutron scattering.

The synthesized pyrrole-derived surfactants were then employed in the synthesis of ISA complexes. The self-assembled materials were characterized and subsequently polymerized by both chemical and electrochemical methods. This polymerization reaction within confined geometry led to a decrease in the structural order of the molecular self-assemblies, as observed by small-angle X-ray scattering, and affected an increase in the conductivity of the resulting materials.

Although molecular self-assembly was expected to afford a highly ordered polymer, the conductivity of the resulting materials was relatively low. The polymerized complex incorporating the double-tailed surfactant was found to be weakly conductive (resistivity = 190 MOhm), and that incorporating the single-tailed surfactant showed a conductivity of 10^{-6} S cm^{-1}. The latter value, however, is comparable (albeit lower) to the conductivity values of similar pyrrole-based polymers, which are reported in the range of 10^{-4} - 10^{-5} S cm^{-1}. The low conductivity of the polymerized ISA materials is a consequence of the situation of the substituent at the N-position of the pyrrole ring and the steric bulk of this substituent that acts both to separate the pyrrole chains, slowing the rate of electron hopping, and to reduce the polymer conjugation length through chain twisting. Low conductivity probably also results from the formation of non-linearly aligned polymer chains due to polymerization in 3D geometry.

A major challenge is to raise the conductivity of these materials. β-substituted monomers are expected to provide an improvement in the conductivity of the polymers by drastically reducing defect formation during polymerization, through hindrance of β-β' and α-β' linkages. Thus, future work may include synthesis of β-substituted pyrrole surfactants and their incorporation in ISA materials.

In the second part of this work, the motif investigated was a property rather than a function, i.e. the influence of the chiral nature of the surfactants on the supramolecular organization of the resulting ISA materials. Circular dichroism (CD) spectroscopy showed that, upon complexation, the molecular chirality of the surfactants is expressed in the perylene

chromophore through the ionic linkage, clearly indicating that the surfactants act as structure-inducing moieties within the superstructures in both solution and the solid state. It was shown that complexes are organised into a left-handed helical arrangement in solution and that the induced chiral effect is opposite in sign to that of the starting materials. In the solid state, the systems are highly ordered liquid-crystalline materials that exhibit lamellar morphologies. Preliminary calculations based on molecular mechanics reveal that, as a result of this chiral transfer, the energy-minimized systems exhibit a twist within the perylene stacks. The well-defined structures presented here are the first examples of ISA materials showing supramolecular chirality.

The possibility to tune the materials properties and characteristics of such ionically self-assembled materials through the choice of the starting materials, opens a wide variety of opportunities for the production of functional chiral materials for application in display technologies (e.g. for the production of polarised emission) or as chiral sensing materials. The induction of chiral effects opposite in sign to that of the starting materials offers an intriguing possibility for the production of dynamic switchable materials. This process is not fully understood, and will be the subject of further investigations. Possible future studies include the influence of the 'twisting power' of surfactant tectons owing to the position of the chiral centers and the alkyl tail volume, as well as the formation of lyotropic chiral phases.

The results of this thesis show that, through the use of functional surfactants, functional nanostructures can be obtained by the ionic self-assembly (ISA) strategy. Thus, the use of oppositely charged tectons in ISA not only provides the possibility for facile synthesis of self-organising nanostructured materials, but also the chance to use this method as a toolbox for the production of functional materials.

5   EXPERIMENTAL

5.1 Materials

All common solvents were of analytical grade and used as received, unless stated otherwise. Water used for the preparation of the relevant solutions was distilled and deionized in a "Milli- Q" water purification system (Millipore Corp.)

Perylene Dye Perylenetetracarboxylic acid-3,4,9,10-dianhydride (Fluka, purum), sulphanilic acid (Sigma-Aldrich, >99%), imidazole (Sigma-Aldrich, >99%), zinc acetate (Sigma-Aldrich, 99.99%) and sodium acetate (Sigma-Aldrich, >99%) were used as received.

Pyrrole Surfactants Pyrrole (Sigma-Aldrich, 98%) was used after distillation under reduced pressure. Pyridine and dimethylformamide (DMF) were dried over 0.3 nm molecular sieves. The following reagents were purchased from the indicated suppliers and used without further purification: N,N-dimethylethylenediamine (Sigma-Aldrich, 99%), 2,5-dimethoxytetrahydrofurane (cis + trans, Fluka, ≥97%), ethanoic acid (Sigma-Aldrich, ≥99.7%), Na_2CO_3 (Fluka, ≥99.5%), Na_2SO_4 (Acros, 99%), 1-dodecanol (Acros, 98%), p-toluene sulphonic acid chloride (Sigma-Aldrich, 98%), HCl (Sigma-Aldrich, 37% in water), 1,12-dibromododecane (Sigma-Aldrich, 98%), KOH (Fluka, ≥86%), triethylamine (Sigma-Aldrich, 99%).

Chiral Surfactants 2-benzyloxycarbonylamino-6-tert-butoxycarbonylamino-hexanoic acid dicyclohexylamine salt (Z-lys(Boc)-OH DCHA, Fluka, >98%), hexadecanol (Fluka, >99%), N,N-dicyclohexylcarbodiimide (DCC, Fluka, >99%), 4-(dimethylamino)pyridine (DMAP, Acros, 99%), Pd/C (10% Pd, Merck), chloroform ($CHCl_3$, Biosolve), methanol (MeOH, Biosolve), ethyl acetate (EtOAc, Biosolve), trifluoroacetic acid (TFA, Fluka, >98%), 1M HCl (Merck), dimethylsulphoxide (DMSO, Fluka), N-methyl-pyrrolidone (NMP, Biosolve) and dimethylformamide (DMF, Sigma-Aldrich) were used as received. Dichloromethane (DCM) was distilled over P_2O_5.

5.2   Synthetic Procedures

5.2.1   Synthesis of perylene dye derivative

The perylene dye derivative, N,N'-bis(4-benzenesulphonic acid) perylene-3,4:9,10-tetracarboxyldiimide sodium salt (**1**), was synthesized following a slightly modified procedure for similar perylene derivatives described previously.[121] Perylenetetracarboxylic acid-3,4,9,10-dianhydride (1 g, 2.6 mmol) was reacted with sulphanilic acid (0.8664 g, 5 mmol) in molten imidazole as solvent in the presence of zinc acetate (350 mg, 2.2 mmol). The reaction mixture was stirred under Ar for 6 h at 180 $^{\circ}$C and, after cooling to RT, was added to a mixture of 5 mL of water and 50 mL of ethanol. The precipitate was collected by filtration and then reacted with sodium acetate to give the sodium salt of the perylene derivative. Yield = 90%; elemental analysis (%) calculated for $C_{36}H_{16}O_{10}N_2S_2Na_2$ (746 g): C 57.91, H 2.14, N 3.75, S 8.58; found C 53.67, H 2.69, N 4.01, S 7.59. Further analysis is presented in Appendix, Figures 6-8.

5.2.2   Synthesis of surfactants

5.2.2.1   Pyrrole-Based Surfactants

5.2.2.1.1   Dodecyl-dimethyl-(2-pyrrol-1-yl-ethyl)-ammonium tosylate (Scheme 4, 4)

Synthesis of the double-tailed pyrrole-containing surfactant, dodecyl-dimethyl-(2-pyrrol-1-yl-ethyl)-ammonium tosylate (**4**), has already been described.[76,107] In the synthesis, the described strategy was employed, although with various modifications. N,N-dimethyl-2-(pyrrol-1-yl)ethylamine (**2**) was synthesized by reaction of N,N-dimethylethylenediamine (24.7 mL, 0.4 mol) and 2,5-dimethoxytetrahydrofuran (37.3 mL, 0.4 mol) in ethanoic acid (160 mL) and distilled water (240 mL) at 70 $^{\circ}$C for 6 h. The reaction flask was then cooled in an ice bath and a saturated aqueous solution of Na_2CO_3 was added very carefully to the reaction mixture while stirring. Addition of the salt was terminated when the pH of the

solution reached a value of about 7. The organic phase was extracted with dichloromethane, washed 2x with water and dried over Na_2SO_4. The solvent was removed under reduced pressure and the resulting oil was purified by chromatography on a basic alumina column (Brockmann activity I) using dichloromethane as elution solvent (yield = 22%). ^{1}H NMR (Appendix, Figure 9): 6.7 ($C_{\alpha,\alpha'}$, 2H, 'br' s), 6.2 ($C_{\beta,\beta'}$, 2H, 'br' s), 4.0 ($NCH_2CH_2N(CH_3)_2$, 2H, t), 2.7 ($CH_2N(CH_3)_2$, 2H, t), 2.3 ($N(CH_3)_2$, 6H, s).

1-tosyldodecane (**3**) was prepared by reacting equimolar amounts of 1-dodecanol (6.3 g, 34 mmol) and p-toluene sulphonic acid chloride (9.9 g, 52 mmol) under Ar at 0 °C for 24 h in anhydrous pyridine (80 mL). Use of the acid chloride, as compared to the acid as previously described,[76] allowed for increased reactivity of the tosylate compound. A volume of chloroform (equal to ≈¼ the volume of pyridine) was added to the reaction mixture, which is a practice employed in the general synthesis of p-toluenesulphonic acid alkyl esters.[122] A mixture of 40 g of ice and 14 mL concentrated HCl were then added to the reaction mixture and the chloroform layer was collected. This layer was washed 3x with an ice-water/HCl (40 mL/14 mL) solution and dried over Na_2SO_4. The solvent was removed under reduced pressure and product **3** was used without further purification (yield = 55%). ^{1}H NMR (Appendix, Figure 10): δ 7.8 ($H_{aromatic}$, 2H, d), 7.3 ($H_{aromatic}$, 2H, d), 4.0 (CH_2OS, 2H, t), 2.4 ($C_6H_5CH_3$, 3H, s), 1.60 (CH_2CH_2OS, 2H m), 1.5 ($CH_3(CH_2)_9$, 18H, m), 0.9 ($CH_3(CH_2)_9$, 3H, t).

Surfactant 4 was obtained by reaction of 2 (2.4 g, 17.6 mmol) and 3 (6 g, 17.6 mmol) in absolute ethanol (11 mL) as solvent, at 80 °C for 17 h under Ar.[76] The solvent was partially removed under reduced pressure and the resulting oil was dropped into dry diethyl ether to form a white precipitate. This surfactant precipitate was collected by suction filtration and dried under vacuum at RT. To prevent its polymerization, when not in use, the surfactant was kept in a vessel wrapped in aluminium foil and stored in the fridge. Yield = 85%; elemental analysis (%) calculated for $C_{27}H_{46}N_2SO_3$ (478.4 g): C 67.79, H 9.62, N 5.86, S 6.70; found C 67.64, H 9.43, N 5.86, S 6.75. ^{1}H NMR (Appendix, Figure 11): δ 7.7 ($H_{aromatic}$, 2H, d), 7.1 ($H_{aromatic}$, 2H, d), 6.7 ($C_{\alpha,\alpha'}$, 2H, 'br' s), 6.1 ($C_{\beta,\beta'}$, 2H, 'br' s), 4.5 ($NCH_2CH_2N(CH_3)_2$, 2H, t), 4.0 ($NCH_2CH_2N(CH_3)_2$, 2H, t), 3.2 ($N(CH_3)_2$, 6H, s), 2.3 ($C_6H_5CH_3$, 3H, s), 1.7 ($NCH_2CH_2(CH_2)_9CH_3$, 2H, m), 1.5 ($NCH_2CH_2(CH_2)_9CH_3$, 2H, m), 1.2 ($CH_3(CH_2)_9$, 18H, m), 0.86 ($CH_3(CH_2)_9$, 3H, t). The product purity (as confirmed by [1]H

NMR) was >91%. When required, e.g. for surface tension measurements, the purity was increased to >99%, by recrystallization from bidistilled water.

5.2.2.1.2   Triethyl-(12-pyrrol-1-yl-dodecyl)-ammonium bromide (Scheme 5, 6)

Dibromododecane (51.60 g, 0.157 mol), KOH (3.52 g, 0.063 mol) and freshly distilled pyrrole (4.35 mL, 0.063 mol), were left to react overnight in anhydrous DMF (150 mL) under Ar at RT. Bidistilled water (150 mL) was added to the reaction mixture and the organic phase was extracted with diethylether (6 x 50 mL) and subsequently dried over Na_2SO_4. The solvent was removed by rotary evaporation and a brownish viscous paste resulted. This solid was purified on a silica gel column using a 10:1 mixture of high boiling petroleum ether (PET):dichloromethane as elution solvent to result in 12-pyrrol-1-yl-dodecylbromide (**5**) as a yellow oil (yield = 76%). ^{1}H NMR (Appendix, Figure 12): δ 6.6 ($C_{\alpha,\alpha'}$, 2H, 'br' s), 6.1 ($C_{\beta,\beta'}$, 2H,'br' s), 3.9 (NCH_2, 2H, t), 3.4 (CH_2Br, 2H, t), 1.9-1.8 (NCH$_2$CH_2(CH$_2$)$_8$CH_2, 4H, m), 1.3 (NCH$_2$CH$_2$(CH_2)$_8$, 16H, m).

Triethylamine (60 mL, 0.430 mol) and 12-pyrrol-1-yl-dodecylbromide (**5**) (15.02 g, 0.048 mol) were refluxed in absolute ethanol (100 mL) for 60 h under Ar. Removal of the solvent and excess amine via rotary evaporation resulted in a dark yellow oil. This was dissolved in a minimum amount of bidistilled water and freeze dried, yielding surfactant **6**. Yield = 69%; elemental analysis (%) calculated for $C_{22}H_{43}N_2Br$ (415 g): C 63.61, H 10.36, N 6.75, S 0.00; found C 61.30, H 10.41, N 6.34, S 0.00. ^{1}H NMR (Appendix, Figure 13): δ 6.6 ppm ($C_{\alpha,\alpha'}$, 2H, 'br' s), 6.1 ($C_{\beta,\beta'}$, 2H,'br' s), 3.8 (NCH_2, 2H, t), 3.4 (N(CH_2CH$_3$)$_3$, 6H, q), 3.2 (CH_2N(CH$_2$CH$_3$)$_3$, 2H, m), 1.8 (NCH$_2$CH_2, 2H,m), 1.3 ((CH$_2$)$_8$CH_2CH$_2$N(CH$_2$CH_3)$_3$, 27H, m).

5.2.2.2 Lysine-Based Surfactants

5.2.2.2.1 2-benzyloxycarbonylamino-6-tert-butoxycarbonylamino-hexylhexadecanoate (Scheme 6, 9)

Z-lys(Boc)-OH was commercially available as the dicyclohexylamine (DHCA) salt. To obtain the free acid form, Z-lys(Boc)-OH DCHA was suspended in EtOAc and washed with 5% citric acid solution until both phases were no longer turbid. After separation, the organic phase was washed twice with water and once with brine. Subsequent drying over magnesium sulphate followed by filtration and evaporation of the solvent, yielded the free acid form; a yellow oil, which was used for further synthesis. Z-lys(Boc)-OH (2 g, 5.25 mmol) and hexadecanol (1.2 g, 5.0 mmol) were dissolved in dry DCM, and the mixture was cooled to -20 °C. While stirring vigorously, DCC (1.2 g, 5.8 mmol) and DMAP (70 mg, 0.58 mmol) were added in quick succession and the mixture was allowed to warm to RT; a white precipitate formed. The reaction mixture was then stirred for 24 h at RT. Dicyclohexylurea (DCU) was filtered off and weighed to determine whether the reaction had reached completion. Evaporation of the solvent yielded the crude product (yield = 75%). This product was purified by column chromatography on a silica gel column using 15 vol.% EtOAc in CHCl$_3$ as elution solvent. ^{1}H NMR (Appendix, Figure 14): δ 0.9 (CH$_2$CH_3, 3H, t), 1.2-1.9 ((CH_2)$_{14}$CH$_3$, 28H, m and (CH_2)$_3$CH$_2$NH, 6H, m), 1.4 (C(CH$_3$)$_3$, 9H, s), 3.1 (CH_2NHCOOC(CH$_3$)$_3$, 2H, dd), 4.1 (COOCH_2CH$_2$, 2H, t), 4.3 (NHCHCO, 1H, dd); 4.5 (NHCOOC(CH$_3$)$_3$, 1H, t); 5.1 (COOCH_2C$_6$H$_5$, 2H, s); 5.4 (NHCOOCH$_2$C$_6$H$_5$, 1H, t), 7.3 (C$_6$$H_5$, 5H, m). MALDI-TOF-MS (Appendix, Figure 15): m/e 505 (M$^+$-Boc +2H), 627 (M$^+$ + Na), 643 (M$^+$ + K).

5.2.2.2.2 2-amino-6-tert-butoxycarbonylamino-hexylhexadecanoate (Scheme 6, 10)

For Z-group deprotection, **9** (0.5 g, 0.83 mmol) was dissolved in MeOH and a catalytic amount of Pd/C was added. The system was purged with a stream of N$_2$ to remove all oxygen. Hydrogenation was carried out overnight using a shaken type Parr reactor operating at 80 psi H$_2$ overpressure. The reaction was monitored by ^{1}H NMR spectroscopy

until complete deprotection of the Z-group. The catalyst was removed by filtration over Celite and the solvent, formed toluene and CO_2 were evaporated. The crude product was obtained in almost quantitative yield and further purified by column chromatography on a silica gel column using 80 vol.% EtOAc in $CHCl_3$ as elution solvent. ^1H NMR (Appendix, Figure 16): δ 0.9 (CH_2CH_3, 3H, t), 1.2-1.9 (($CH_2)_{14}CH_3$, 28H, m and ($CH_2)_3CH_2NH$, 6H m), 1.4 ($C(CH_3)_3$, 9H, s), 1.8 (CH_2NH_2, 2H, m), 3.1 ($CH_2NHCOOC(CH_3)_3$, 2H, dd), 3.5 ($CHCOO(CH_2)_{15}CH_3$, 1H, m), 4.1 ($COOCH_2CH_2$, 2H, t), 4.5 ($NHCOOC(CH_3)_3$, 1H, t). MALDI-TOF-MS (Appendix, Figure 17): m/e 415 (M^+ -$C(CH_3)_3$ +H), 471 (M^+ + H), 493 (M^+ + Na).

5.2.2.2.3   5-benzyloxycarbonylamino-5-hexadecyloxycarbonyl-pentyl-ammonium trifluoro-acetic acid salt (Scheme 6, 11)

Surfactant **11** was synthesized by deprotection of the Boc-group of **9** under acidic conditions. A 1 %wt solution of **9** was prepared in 90 % aqueous TFA in an open flask and left to stir for 1.5 h to allow the CO_2 and isobutene to escape. This solution containing the mono-protonated ammonium surfactant was directly used for complexation with **1.**

5.2.2.2.4   1-hexadecyloxycarbonyl-pentylene-1,5-diammonium dichloride (Scheme 6, 12)

Surfactant **12** was synthesized by deprotection of the Boc-group of **10** under acidic conditions, thereby also protonating the free amine present after Z-group deprotection of **9**. A 1 %wt solution of **10** was prepared in 1 M HCl in an open flask and left to stir for 1.5 h to allow the CO_2 and isobutene to escape. This solution containing the di-protonated diammonium surfactant was directly used for complexation with **1**.

5.2.3 Synthesis of Complexes

For the preparation of the ISA complexes, 1 %wt aqueous solutions of the perylene dye derivative (**1**) were added dropwise to 1 %wt aqueous solutions of the respective

surfactant[v] in a 1:1 molar ratio with respect to the charged groups. This procedure yielded the complexes as precipitates. After stirring the suspensions for approximately 4 h while purging with Ar, the complex precipitates were collected by centrifugation and washed several times with doubly distilled water to remove produced salts and possible non-complexed precursors. In the case of halide-containing surfactants, the washing procedure was repeated until the supernatant did not turn turbid on addition of a few drops of 0.5 M $AgNO_3$ solution, implying complete removal of the excess counterions generated during complex formation. The materials were dried under vacuum at RT for 24 h and, when required, dissolved in chloroform and cast into films on Teflon foil.

5.2.3.1 Pyrrole Complexes

Complex **7**: Yield = 82%; elemental analysis (%) calculated for $C_{76}H_{94}O_{10}N_6S_2$ (1314 g): C 69.41, H 7.15, N 6.39, S 4.87; found: C 67.08, H 7.17, N 6.27, S 4.84.

Complex **8**: Yield = 87%; elemental analysis (%) calculated for $C_{80}H_{102}O_{10}N_6S_2$ (1370 g): C 70.07, H 7.44, N 6.13, S 4.67; found: C 67.28, H 8.19, N 6.00, S 4.37.

5.2.3.2 Chiral Complexes

Complex **13**: Yield = 78%; elemental analysis (%) calculated for $C_{96}H_{122}O_{18}N_6S_2$ (1710 g): C 67.37, H 7.13, N 4.91, S 3.74; found C 66.02, H 7.42, N 4.86, S 3.38.

Complex **14**: Yield = 83%; elemental analysis (%) calculated for $C_{58}H_{64}O_{12}N_4S_2$ (1072 g): C 64.93, H 5.97, N 5.22, S 5.97; found C 63.27, H 6.97, N 5.04, S 4.63.

The elemental analysis results of all complexes are satisfactory in light of the elemental analysis results obtained for the starting perylene-based dye material.

---

v When necessary, the surfactant solution was heated above the Krafft temperature of the respective surfactant to allow for complete dissolution. In such cases, the water used for washing of the resulting complex was also heated above the surfactant Krafft temperature to aid removal of potentially non-complexed surfactant.

5.2.4 Polymerization of pyrrole-containing complexes

5.2.4.1　　　Chemical Polymerization

The complex powders were ground finely using a pestle and mortar and then annealed at 100 $^{\circ}$C for 30 mins. The apparatus used for the chemical polymerization is shown in Figure 42. Typically, the complexes (9.5×10^{-2} mmol) were each placed in a reactor set at 0 $^{\circ}$C under Ar and 3 ml of deionized water was added. A solution of FeCl$_3$ (9.5 mmol) as the oxidant in 2 mL of deionized water was then added dropwise to each reactor with vigorous stirring (molar ratio monomer/oxidant = 1/50). On addition of the oxidant, the complex powders began to darken in colour. When all the oxidant was added, HCl (9.5 mmol) as the dopant was added to each reactor (molar ratio monomer/dopant = 1/50).   Thus, polymerization was carried out using the so-called 'two-step' method in which the monomer is first polymerized in the absence of the dopant and then the resulting polymer is doped.[55c] The reaction mixtures were left to stir for 48 hours under Ar, after which each was poured into a large excess of deionized water and then filtered. The resulting residues were repeatedly washed with water until the filtrate was no longer yellow in colour, indicating complete removal of FeCl$_3$. The powders were then dried for 24 hours at RT under vacuum. This method was also used for the polymerization of pyrrole and the pure surfactants as blanks.

Figure 42: Set-up for the chemical polymerization using FeCl$_3$ as oxidant and HCl as dopant. The reactors are equipped with a thermostatted jacket and an air-tight seal allowing the reaction to proceed at a controlled temperature and in an inert atmosphere.

Chemical polymerization was also conducted using iodine vapour as both oxidant and dopant.[50,65] The complex powders were ground finely using a pestle and mortar and then annealed at 100 ^{o}C for 30 mins. The fine powders were then each spread over the base of a Petri dish and exposed over 2 days to saturated iodine vapour at RT under Ar. The excess iodine was removed by placing the powders under vacuum for 24 hours.

5.2.4.2   Electrochemical Polymerization

Films of the pyrrole-containing complexes were prepared on ITO-coated glass slides by spin-coating solutions of 20 mg mL^{-1} concentration in chloroform at a spin-rate of 1000 rpm for 1 min. Part of the slide was covered with aluminium foil prior to spin-coating so that part of the substrate was clear of the film to allow for electrical contact. The films were submerged in an aqueous phosphate buffer at RT and electropolymerization was performed by scanning the potential to a maximum of 1.2 V, at a scan speed of 50 mV s^{-1}. All potentials reported are relative to the Ag/AgCl reference electrode.

5.3 Instrumentation

Differential scanning calorimetry (DSC) was performed on a Netzsch DSC 204. Samples were examined at a scanning rate of 1 K min^{-1} or 10 K min^{-1} by applying two heating and two cooling cycles. Thermo gravimetric analysis (TGA) was performed on a Netzsch TG 209 at a scanning rate of 20 K min^{-1}.

Wide-angle X-ray scattering (WAXS) measurements were performed on a Nonius PDS120 powder diffractometer in transmission geometry. An FR590 generator was used as the source of Cu α radiation (λ = 0.154 nm). Scattered radiation was measured using a Nonius CPS120 position-sensitive detector (resolution in 2θ is 0.018 °).

Small-angle X-ray scattering (SAXS) measurements were performed on a Bruker-Nonius rotating anode (U = 40 kV, I = 100 mA, λ = 0.154 nm) using image plates. With the image plates placed at a distance of 40 cm from the sample, a scattering vector of s = 0.07-1.6 nm^{-1} was available. 2D diffraction patterns were transformed into 1D radial averages.

Elemental Analysis (EA) was performed on a Vario EL Elementar (Elementar Analysen-systeme, Hanau, Germany). The samples were tested for carbon, hydrogen, nitrogen and sulfur content.

[1]H Nuclear Magnetic Resonance (NMR) spectra were recorded on a 400 MHz Bruker spectrometer equipped with a 9.395 T Bruker magnet. Samples of ca. 5 mg were analyzed at RT in deuterated solvent. The signal of the solvent was used as chemical shift reference. [13]C Nuclear Magnetic Resonance (NMR) spectra were performed on a Bruker Avance 400 NMR spectrometer operating at 100.61 MHz. CP/MAS experiments were carried out using a standard pulse sequence with high-power composite-pulse ^{1}H decoupling employed during the acquisition of the ^{13}C FID. The samples were spun at the magic angle at a rate of 10,520 Hz. For all samples, a ^{13}C contact time of 5 ms was used together with a recycle delay of 3 s between scans.

Polarized Light Microscopy (PLM) measurements were performed with an Olympus BX50 microscope equipped with a Linkam THMS 600 heating/cooling stage and a TP92 temperature controller. Measurements were generally carried out at a heating/cooling rate of 10 K min^{-1} but at the phase transition regions, a much slower rate (ca. 1 K min^{-1}) was used.

Ultraviolet-Visible (UV-VIS) spectra were recorded at RT using a UVIKON 940/941 dual-beam grating spectrophotometer (Kontron Instruments).

Circular Dichroism (CD) measurements were performed on a Jasco J 715 Spectrometer at RT and at 50 ^{o}C. The measurement parameters were set as follows: Resolution: 0.2 nm; Scan speed: 10 nm s^{-1}; Bandwidth: 1 nm. Each measurement involved baseline correction and the accumulation of at least 5 single scans.

Atomic Force Microscopy (AFM) measurements were performed at RT on a Nanoscope IIIa controller (Digital Instruments, *USA*) in the Tapping Mode regime. Microfabricated silicon cantilever tips with a resonance frequency of ca. 300 kHz and a spring constant of about 42 N m^{-1} were used.

Surface Tension Measurements were measured in bidistilled water at $40(\pm 0.5)$ $^{\circ}$C with a K12 tensiometer (Krüss) using the Du Nouy ring method.

Potentiometric measurements were performed with a 702SM Titrino (Metrohm) in a jacketed cell, through which thermostatted water was circulated to maintain a constant temperature of $40(\pm 0.5)$ $^{\circ}$C. The working electrode was an ionic surfactant electrode (Metrohm, temperature range = 0-40 $^{\circ}$C) and the potential was measured relative to an Ag/AgCl in 3 M KCl reference electrode. The composition of the medium used for the measurements was a 10^{-2} M p-toluene sulphonic acid sodium salt (sodium tosylate, NaOTs) electrolyte (Acros, 99%).

Isothermal titration calorimetry (ITC) measurements were performed with a VP-ITC microcalorimeter from MicroCal (Northhampton, MA). The reference and sample cells, each with a volume of 1.442 mL, were enclosed in an adiabatic jacket and kept at 40 $^{\circ}$C. Both working and reference cells were filled with the electrolyte used to prepare the sample solution. The surfactant solution was injected stepwise into the working cell via a syringe of total volume 288μl. Thus, the measurement performed was of the dilution type. The concentration of the surfactant solution in the syringe was chosen in such a way that, with increasing surfactant concentration in the sample cell, the cmc was reached during the experiment. Small aliquots (10μl) of titrant were successively injected into the solution of the working cell. Each injection produced a characteristic peak in the heat flow (J s^{-1}) due to released or absorbed heat. An exothermic reaction yields a negative peak signal because the released heat in the sample cell is no longer required from the resistive heater of the instrument. Similarly, endothermic reactions cause a positive peak. Integration of the peaks provides the heat per injection. The data analysis was performed using the Origin software provided by MicroCal.

Dynamic Light Scattering (DLS) measurements were performed on an ALV-NIBS High Performance Particle Sizer (ALV-Laser) Vertriebgesellschaft m.b.H., Langen, Germany. The instrument uses a 2 mW HeNe Laser at a wavelength of 632.8 nm and detects the scattered light at an angle of 173°. The autocorrelation function is measured using exponential spacing of the correlation time. The data analysis was performed with software provided by ALV.

Conductivity measurements were run at RT on samples in pellet form using silver paste and either the 2- or 4-wire technique, which uses two or four needle point pins, respectively, to mechanically contact the sample surface. The pellets were prepared by pressing the sample (ca. 50mg) under 10 tons for 10 mins. Samples were dried for 24 h under vacuum before measurement.

Chiral films analyzed by UV-VIS spectroscopy, CD spectroscopy and AFM were prepared on quartz slides (1 mm thickness, cleaned with chloroform and dried under nitrogen flow), by spin-coating solutions of varying concentrations (20, 40, 60 and 80 mg mL^{-1}) in chloroform, at a spin-rate of 1000 rpm for 1 min.

6   APPENDIX

The Gibbs adsorption equation may be described as follows:

$$-d\gamma = \Sigma_i \, \Gamma_i \, RT \, \ln C_i \tag{1}$$

where Γ_i = Gibbs surface excess of component i; C_i = concentration of the ith component; R = universal gas constant; T = Kelvin temperature.

The component and total mass balances may yield the following equation:

$$\Gamma_{max} = -1/2RT \, \lim \, d\gamma/d\ln C_{tot} \tag{2}$$

where Γ_{max} = maximum Gibbs surface excess; C_{tot} = total surfactant concentration.

Using Γ_{max}, the minimum area per surfactant molecule, a_{min}, can be calculated:

$$a_{min} = (N_{av} \, \Gamma_{max})^{-1} \tag{3}$$
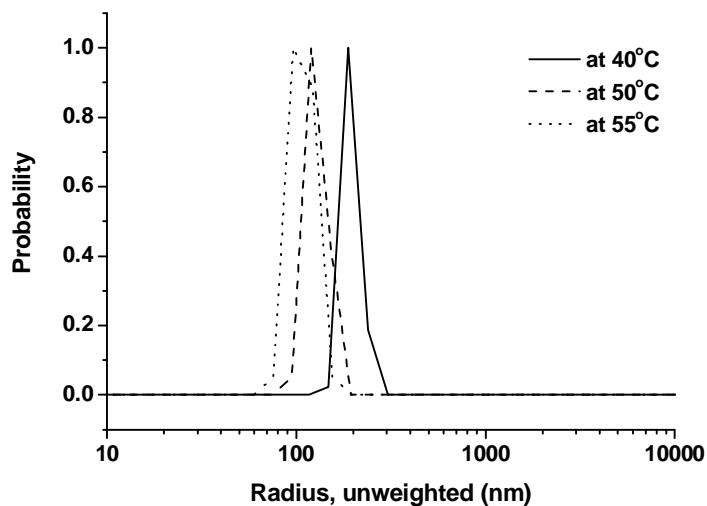
Figure 1: Light Scattering plots of a 1.24 x 10^{-3} M solution of surfactant 4 in water (above cmc) at varying temperatures. Measurements show presence of large aggregates with a mean diameter that decreases with increasing temperature.
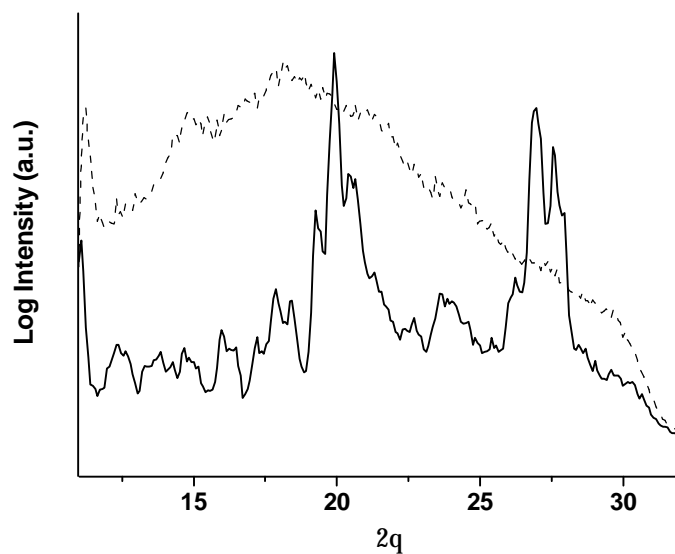
Figure 2: RT WAXS diffractograms of the single-tailed pyrrole-based surfactant, triethyl-(12-pyrrol-1-yl-dodecyl)-ammonium bromide (6) (solid line) and the surfactant after chemical polymerization (dashed line).
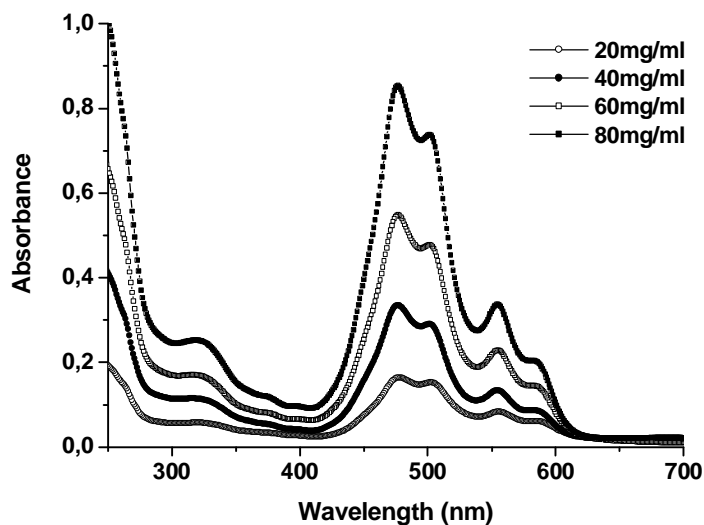
Figure 3: Solid-state UV-VIS spectra of complex 14, as thin films spin-coated from CHCl$_3$ solutions of varying concentrations (20, 40, 60 and 80 mg mL^{-1}). The spectra do not show changes in the optical properties upon concentration variation, at least within the range of concentration measured.
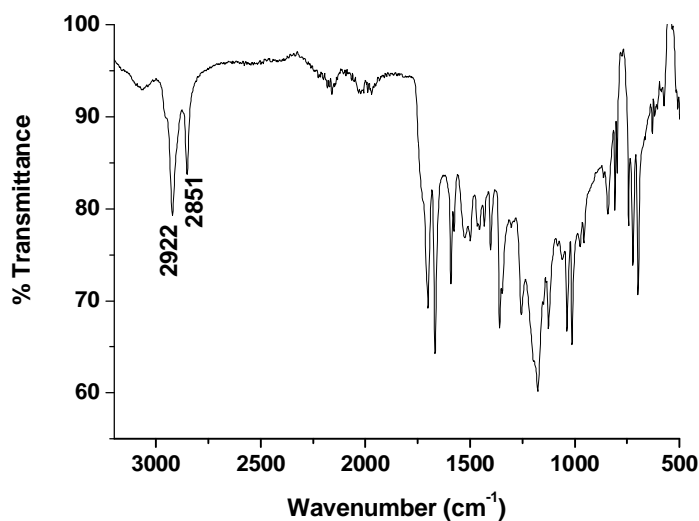
Figure 4: FTIR spectrum of 13, resulting from complexation of PTDI-3 and the singly-charged chiral surfactant, 5-benzyloxycarbonylamino-5-hexadecyloxycarbonyl-pentyl-ammonium trifluoro-acetic acid salt. The $\upsilon_{as}(CH_2)$ band appears at 2922 cm^{-1} and the $\upsilon_s(CH_2)$ band at 2851 cm^{-1}, implying few gauche defects in the arrangement of the hydrocarbon chains.
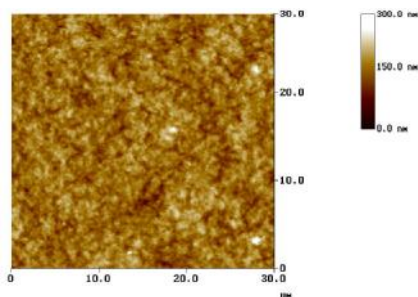
Figure 5: Tapping mode AFM topographic image of complex 13 after spin-coating from an 80 mg mL^{-1} solution in CHCl$_3$.

Concentration (mgml^{-1})	Mean film thickness at centre (nm)	Mean film thickness at edge (nm)
20	118.5	59.4
40	150.5	193.1
60	231.5	231
80	396.3	404.9

Table 1: Mean thickness (at centre and at edge) determined by a scratch test of films of complex 13 prepared by spin-coating from CHCl$_3$ solutions of various concentrations. The thickness of the film is generally of a larger value at the edge than at the centre.
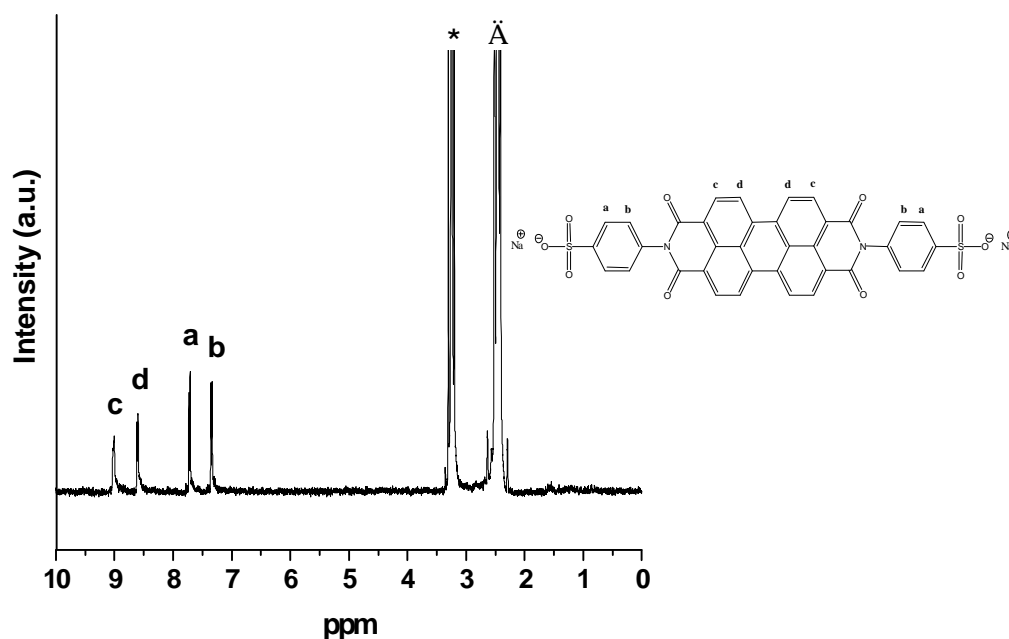
Figure 6: ^{1}H NMR spectrum (DMSO-d$_6$) of N,N'-bis(4-benzenesulfonic acid) perylene-3,4:9,10-tetracarboxyldiimide sodium salt (1). Peaks marked with * and • denote solvent and water peaks, respectively.
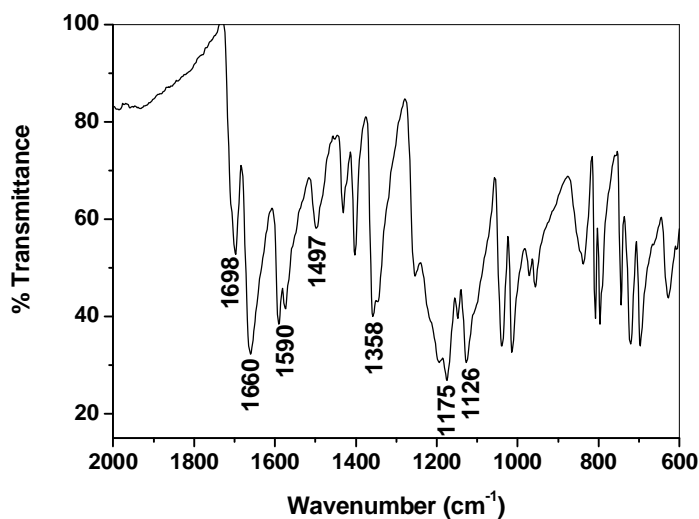
Figure 7: FTIR spectrum of N,N'-bis(4-benzenesulfonic acid) perylene-3,4:9,10-tetracarboxyldiimide sodium salt (1). υ C=O: 1698 cm^{-1}, 1660 cm^{-1}; υ C=C (perylene core): 1590 cm^{-1}; υ C=C (benzene core): 1497 cm^{-1}; υ (O=C)N-CH: 1431 cm^{-1}; υ (O=C)-N: 1402 cm^{-1}; υ SO3-: 1358 cm^{-1}, 1175 cm^{-1}, 1126 cm^{-1}; δ C-H (perylene core): 808 cm^{-1}, 744 cm^{-1}.
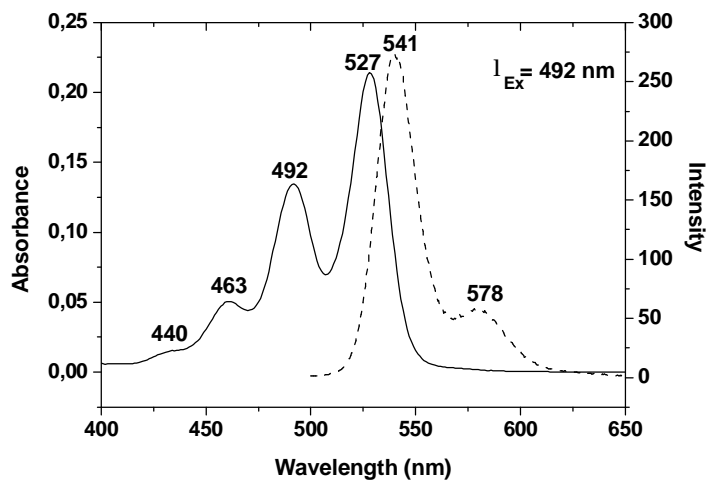
Figure 8: UV-Vis spectrum (solid) and Fluorescence spectrum (dashed) of N,N'-bis(4-benzenesulfonic acid) perylene-3,4:9,10-tetracarboxyldiimide sodium salt (1) in DMSO. Excitation wavelength = 492 nm.
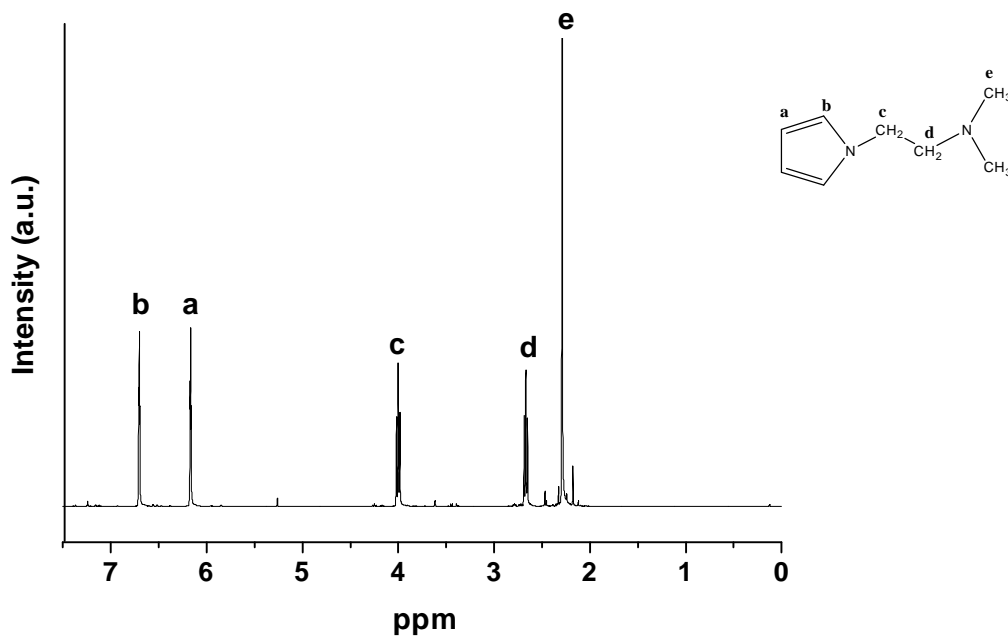
Figure 9: ^{1}H NMR spectrum (CDCl$_3$) of N,N-dimethyl-2-(pyrrol-1-yl)ethylamine (2).
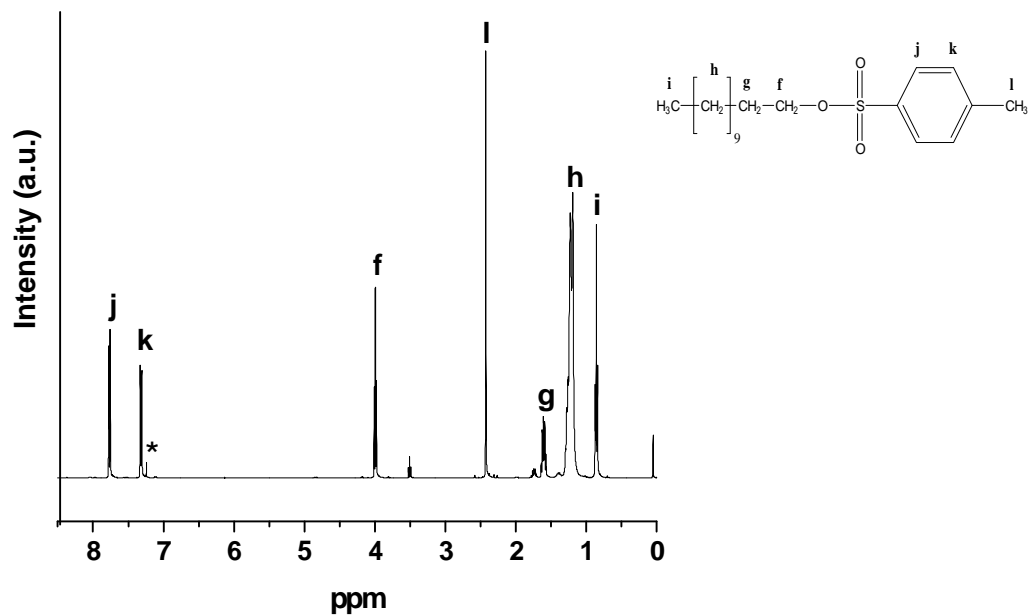
Figure 10: ^{1}H NMR spectrum (CDCl$_3$) of 1-tosyldodecane (3). * denotes solvent peak.
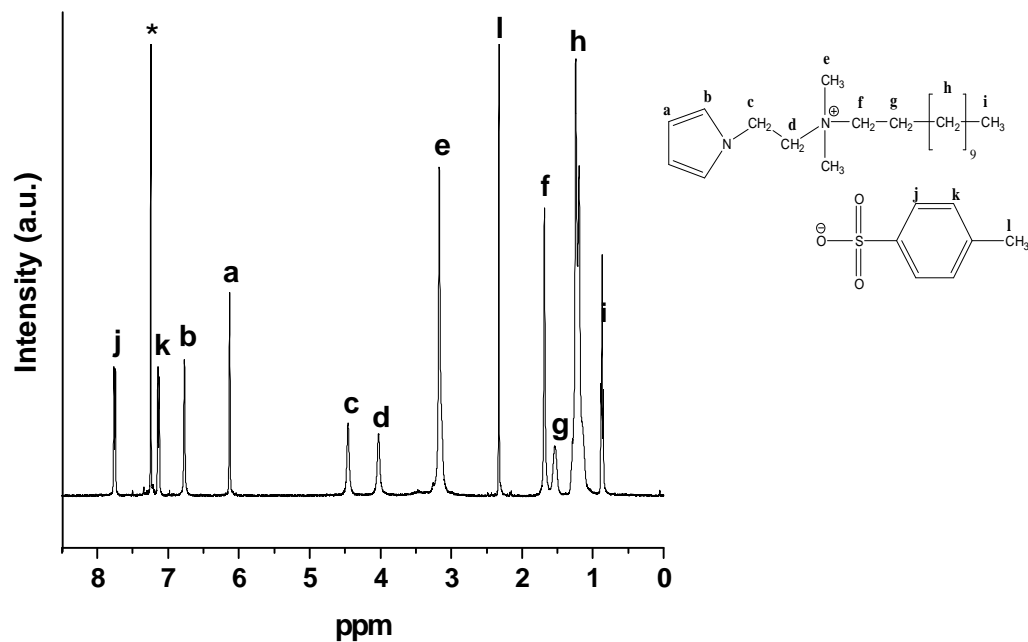
Figure 11: ^{1}H NMR spectrum (CDCl$_3$) of dodecyl-dimethyl-(2-pyrrol-1-yl-ethyl)-ammonium tosylate (4). * denotes solvent peak.
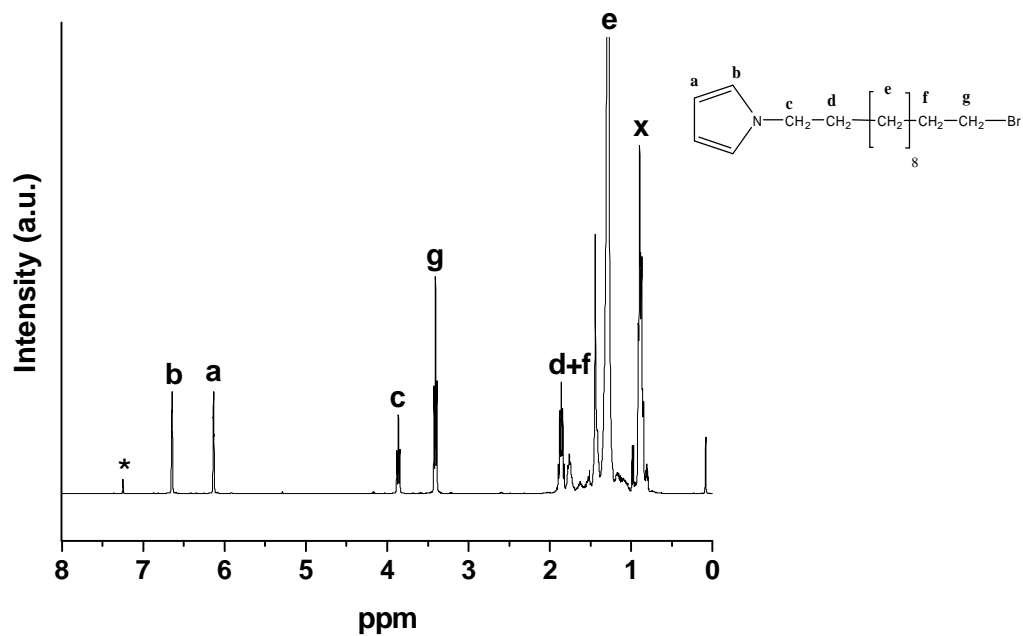
Figure 12: ^{1}H NMR spectrum (CDCl$_3$) of 12-pyrrol-1-yl-dodecylbromide (5). * denotes solvent peak; x denotes traces of PET.
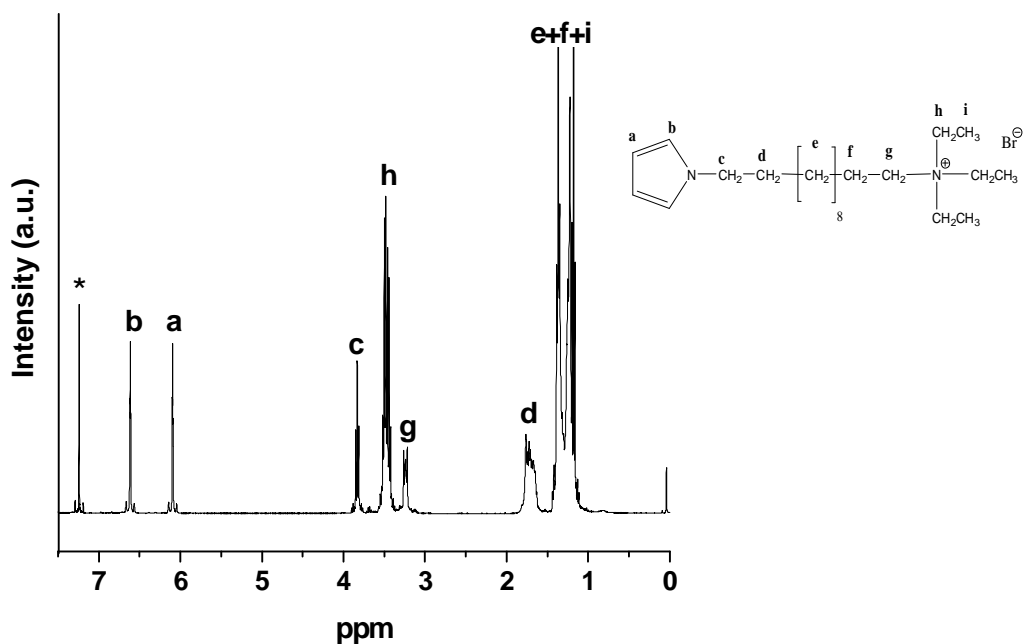
Figure 13: ^{1}H NMR spectrum (CDCl$_3$) of triethyl-(12-pyrrol-1-yl-dodecyl)-ammonium bromide (6). * denotes solvent peak.
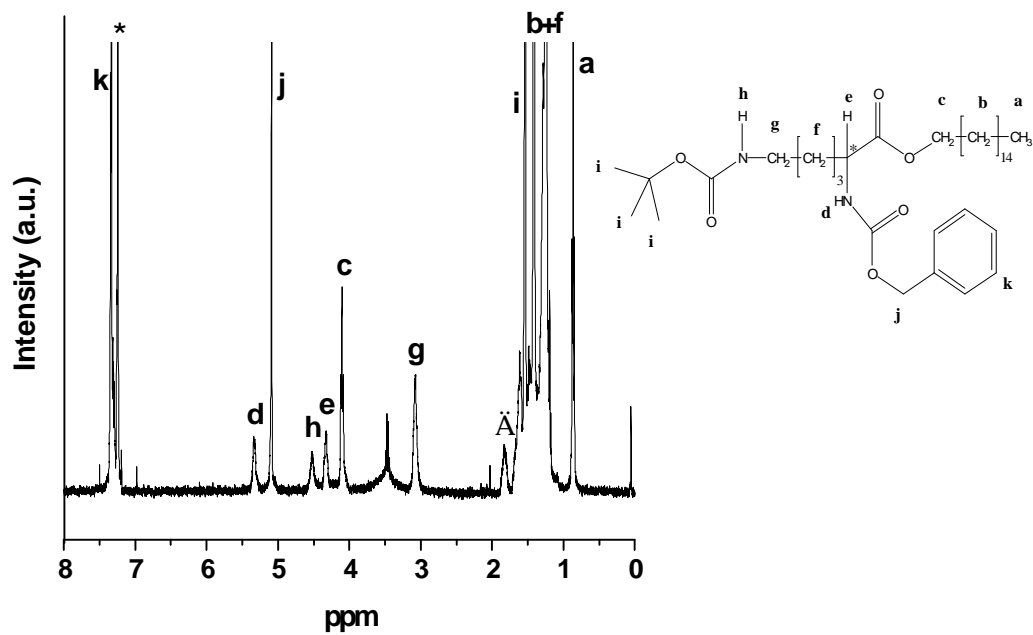
Figure 14: **¹H NMR spectrum (CDCl₃) of 2-benzyloxycarbonylamino-6-tert-butoxycarbonylamino-hexyl hexadecanoate (9). Peaks marked with * and Ä denote solvent and water peaks, respectively.**
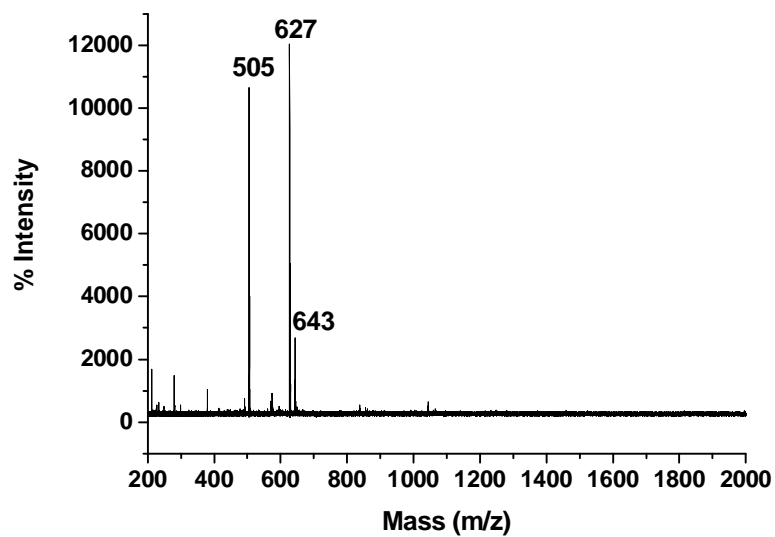
Figure 15: Mass spectrum of 2-benzyloxycarbonylamino-6-tert-butoxycarbonylamino-hexyl hexadecanoate (9).
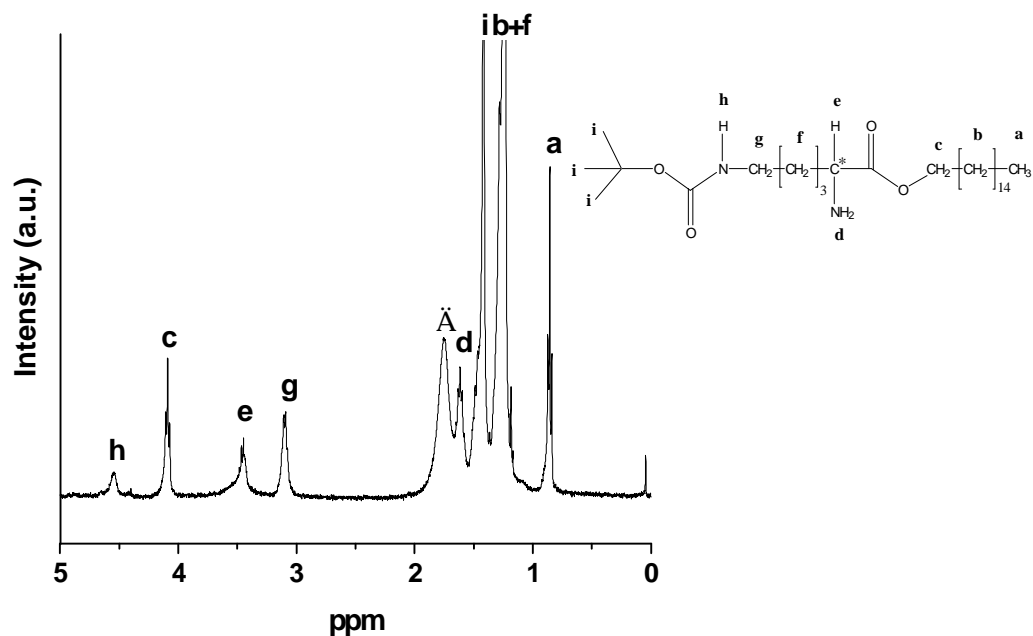
Figure 16: **^{1}H NMR spectrum (CDCl$_3$) of 2-amino-6-tert-butoxycarbonylamino-hexyl hexadecanoate (10).**
Ä denotes water peak
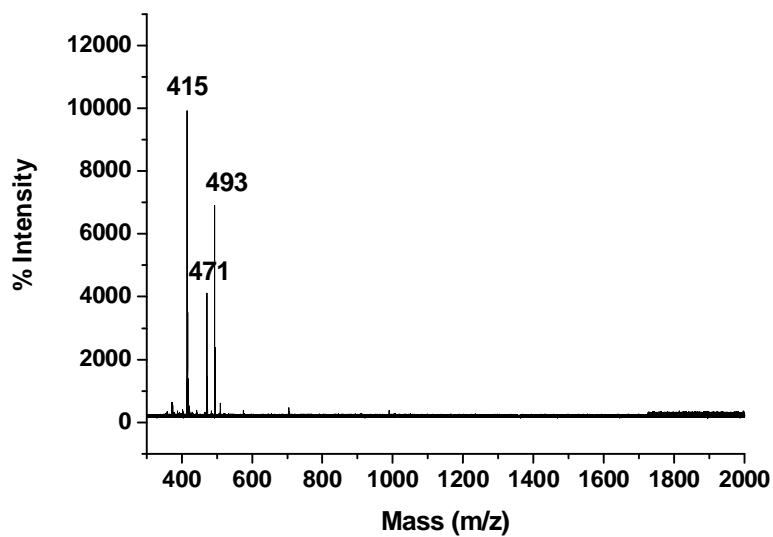
Figure 17: Mass spectrum of 2-amino-6-tert-butoxycarbonylamino-hexyl hexadecanoate (10).

7   LIST OF ABBREVIATIONS

AFM:	atomic force microscopy
cac:	critical aggregation concentration
CD:	circular dichroism
cmc:	critical micelle concentration
CP:	cross-polarization
DNA:	deoxyribonucleic acid
Boc:	tertiary butyloxycarbonyl
'br':	broad
d:	doublet
DBSA:	dodecyl benzene sulphonic acid
dd:	doublet of doublets
DLS:	dynamic light scattering
DSC:	differenctial scanning calorimetry
EO:	ethylene oxide
FTIR:	fourier transform infra-red spectroscopy
FWHM:	full-width half-maximum full
HOMO:	highest occupied molecular orbital
ICP:	intrinsically conducting polymers
ISA:	ionic self-assembly
ITC:	isothermal titration calorimetry
LUMO:	lowest occupied molecular orbital
m:	multiplet
MALDI-TOF-MS:	matrix assisted laser desorption/ionization time-of-flight mass spectrometry
MO:	molecular orbital
MS:	mass spectrometry
NMR:	nuclear magnetic resonance
^{13}C NMR:	carbon-13 nuclear magnetic resonance
^{1}H NMR:	proton nuclear magnetic resonance

β-NSA:	β-naphthalene sulphonic acid
PLM:	polarized light microscopy
ppm:	parts per million
q:	quartet
RT:	room temperature
s:	singlet or second
SAXS:	small angle X-ray scattering
SGLCP:	side group liquid crystal polymer
t:	triplet
TGA:	thermal gravimetric analysis
TMS:	trimethylsilane
UV-VIS:	ultraviolet-visible
WAXS:	wide angle X-ray scattering
XRD:	X-ray diffraction

8 LIST OF SYMBOLS

α: position 2 of the heterocycle or terminal amine in lysine

α': position 5 of the heterocycle

β: position 3 of the heterocycle

β': position 4 of the heterocycle

δ: chemical shift

ε: terminal amine in lysine

ε_L: molar extinction coefficients for left-circularly polarized light

ε_R: molar extinction coefficients for right-circularly polarized light

Δε: difference in intensity of positive and negative bands in CD

θ: angle of incident beam with plane (in XRD) or angle between transition dipoles (in CD) or ellipticity (in CD)

[θ]: molar ellipticity

λ: wavelength

μ_a: electronic transition dipoles of chromophore a

μ_d: electronic transition dipoles of chromophore d

ν_{as}: asymmetric stretching vibration

ν_s: symmetric stretching vibration

π: pi-bonding orbital

π*: pi-antibonding orbital

σ: conductivity

A: analyzer

ΔA: change in absorbance

a_{min}: minimum interfacial area

c: concentration in $g\ mL^{-1}$

C: molar concentration

d: distance between successive planes

e: electronic charge (1.6×10^{-19} C) or extraordinary ray

E: molecular electronic energy

I: current

l:	path length
M:	molecular weight
m/z:	mass/charge ratio
n:	order of diffraction (in XRD) or non-bonding orbital
n_i:	number of charges carried by each type, i
o:	ordinary ray
P:	polarizer
R_{da}:	centre-to-centre transition
s:	scattering vector
U:	voltage
v_i:	drift velocity of an electron
Z_i:	carrier type

9   LIST OF FIGURES

10 AKNOWLEDGEMENTS

Many thanks to Dr. Justyna Justynska for her advice, kindness and the occasional therapy session. Thanks also to Ines Below who was always ready to help and to Laura Hartmann for her stories, that never failed to humour us. Dr Reinhardt Sigel is especially thanked for the unlimited supply of duct tape and bubble wrap. A big thank you also to Zofia, Hans, Andreas, Arne, Mattijs, Matthias, Nicole, Helena, Steffen, Georg, Julia, Rumi and Regina.

From the formative stages of this thesis, to the final draft, I owe my husband, Christian, for urging me on, listening to my groans, laughing with me, and 'rescuing' me at those times when I was felt defeated by technology. His steadfast support in this thesis was invaluable and is deeply appreciated.

11 REFERENCES

1 a) J.-M. Lehn, *Supramolecular Chemistry: Concepts and Perspectives*, VCH, Weinheim, 1995; b) J. L. Atwood, J. E. D. Davies, D. D. MacNicol, F. Vögtle (Eds.), *Comprehensive Supramolecular Chemistry*, Vol. XI, Pergamon, Oxford, 1996.

2 Recent literature on supramolecular chemistry and its applications: a) H.-J. Schneider, A. Yatsimirsky, *Principles and Methods in Supramolecular Chemistry*, Wiley, Chichester, 2000; b) J. W. Steed, J. L Atwood, *Supramolecular Chemistry*, Wiley, Chichester, 2000; c) D. N. Reinhoudt (Ed.), *Supramolecular Materials and Technologies, Perspectives in Supramolecular Chemistry*, Vol. IV, Wiley, Chichester, 2002.

3 J.-M. Lehn *Angew. Chem. Int. Ed.* **1988**, *27*, 89.

4 a) J.-M. Lehn *Proc. Natl. Acad. Sci. USA* **2002**, *99*, 4763; b) J.-M. Lehn *Science* **2002**, *295*, 2400.

5 S. Fernandez-Lopez, H.-S. Kim, E. C. Choi, M. Delgado, J. R. Granja, A. Khasanov, K. Kraehenbuehl, G. Long, D. A. Weinberger, K. M. Wilcoxen, M. R. Ghadiri *Nature* **2001**, *412*, 452.

6 a) J. C. Macdonald, G. M. Whitesides *Chem. Rev.* **1994**, *94*, 2383; b) J.-M. Lehn *Angew. Chem. Int. Ed.* **1990**, *29*, 1304; c) M. W. Hosseini Coord. *Chem. Rev.* **2003**, *240*, 157; d) C. F. J. Faul, M. Antonietti *Adv. Mater.* **2003**, *15(9)*, 673.

7 C. F. J. Faul, M. Antonietti *Chem. Eur. J.* **2002**, *8*, 2764.

8 C. Thalacker, F. Wuerthner *Adv. Funct. Mater.* **2002**, *12*, 209.

9 a) H. Hayagawa, J. P. Santerre, J. C. T. Kwak *J. Phys. Chem.* **1982**, *86*, 3866; b) H. Hayagawa, J. P. Santerre, J. C. T. Kwak *Macromolecules* **1983**, *16*, 1642; c) H. Hayagawa, J. C. T. Kwak *Phys. Chem.* **1983**, *87*, 506.

10 E. D. Goddard *Colloids Surf.* **1986**, *19*, 301.

11 Y. Guan, M. Antonietti, C. F. J. Faul *Langmuir* **2002**, *18*, 5939.

12 Y. Guan, Y. Zakrevskyy, J. Stumpe, M. Antonietti, C. F. J. Faul *J. Chem. Soc.*, *Chem. Commun.* **2003**, 894.

13 Y. Zakrevskyy, C. F. J. Faul, Y. Guan, J. Stumpe *Adv. Funct. Mater.* **2004**, 835.

14 a) F. Camerel, M. Antonietti, C. F. J. Faul *Chem. Eur. J.* **2003**, *9*, 2160; b) F. Camerel, P. Strauch, M. Antonietti, C. F. J. Faul *Chem. Eur. J.* **2003**, *9*, 3764.

15 T. Zhang, C. Spitz, M. Antonietti, C. F. J. Faul *Chem. Eur. J.* **2005**, *11*, 1001.

16 F. Camerel, C. F. J. Faul *J. Chem. Soc.*, *Chem. Commun.* **2003**, 1958.

17 J. J. D. de Jong, L. N. Lucas, R. M. Kellogg, J. H. van Esch, B. L. Feringa *Science* **2004**, *304*, 278.

18 H. Engelkamp, S. Middelbeek, R. J. M. Nolte *Science* **1999**, *284*, 785.

19 Z. Wei, T. Laitinen, B. Smarsly, O. Ikkala, C. F. J. Faul *Angew. Chem. Int. Ed.* **2005**, *44*, 751.

20 a) D. Ganeva, M. Antonietti, C. F. J. Faul, R. D. Sanderson *Langmuir* **2003**, *19*, 6561; b) D. Ganeva, C. F. J. Faul, C. Götz, R. D. Sanderson *Macromolecules* **2003**, *36*, 2862.

21 A. J. Heeger *J. Phys. Chem. B* **2001**, *105(36)*, 8475.

22 M. Mastragostino, A. M. Marinangeli, A. Corradini, S. Giacobbe *Synth. Met.* **1989**, *28*, C501.

23 a) J. Roncali, R. Garreau, D. Delabouglise, F. Garnier, M. Lemaire *J. Chem. Soc.*, *Chem. Commun.* **1989**, 679; b) M. D. Imisides, R. John, P. J. Reiley, G. G. Wallace *Electroanalysis* **1991**, *3*, 879; c) P. N. Bartlett, P. R. Birkin *Synth. Met.* **1993**, *61*, 15; d) L. Dunsch, P. Rapta, A. Neudeck, A. Bartl, R.-M. Peters, D. Reinecke, I. Apfelstedt *Synth. Met.* **1997**, *85*, 1401.

24 a) J. C. Dubois, O. Sagnes, F. Henry *Synth. Met.* **1989**, *28*, 871; b) H. Kuhn, R. Gregory, W. Kimbrell *Int. SAMPE Electron. Cong.* **1989**, *3*, 570.

25 a) T. J. Yamamoto *J. Chem. Soc.*, *Chem. Commun,* **1981**, 187; b) L. W. Shacklette, R. R. Chance, D. M. Ivory, G. G. Miller, R. H. Baughman *Synth. Met.* **1980**, *1*, *307*; c) D.-K. Moon, A. B. Padias, H. K. Jr. Hall, T. Huntoon, P. D. Calvert *Macromolecules*, **1995**, *28*, 6205.

26 a) D. D. C. Bradley *Chem. Br.* **1991**, *8*, 719; b) K. Davidson *Educ. Chem.* **1991**, *28(6)*, 155; c) S. Chao, M. S. Wrighton *J. Am. Chem. Soc.* **1987**, *109*, 2197; d) B. Bianco, A. Bonfiglio *Thin Solid Films* **1996**, *284-285*, 520.

27 a) C. K. Chiang, C. R. Jr. Fincher, Y. W. Park, A. J. Heeger, H. Shirakawa, E. J. Louis, S. C. Gau, A. G. MacDiarmid *Phys. Rev. Lett.* **1977**, *39*, 1098; b) C. K. Chiang, M. A. Druy, S. C. Gau, A. J. Heeger, E. J. Louis, A. G. MacDiarmid, Y. W. Park, H. Shirakawa *J. Am. Chem. Soc.* **1978**, *100*, 1013; c) C. K. Chiang, S. C. Gau, C. R. Jr. Fincher, Y. W. Park, A. G. MacDiarmid, A. J. Heeger *Appl. Phys. Lett.* **1978**, *33*, 18; d) C. K. Chiang, Y. W. Park, A. J. Heeger, H. Shirakawa, E. J. Louis, A. G. MacDiarmid *J. Chem. Phys.* **1978**, *69*, 5098; e) Y. W. Park, M. A. Druy, C. K. Chiang, A. G. MacDiarmid, A. J. Heeger, H. Shirakawa, S. Ikeda *J. Polym. Sci., Polym. Lett. Ed.* **1979**, *17*, 195; f) Y. W. Park, A. Denenstein, C. K. Chiang, A. J. Heeger. A. G. MacDiarmid *Solid State Commun.* **1979**, *29*, 747; g) G. E. Wnek. J. C. W. Chien, F. E. Karasz, M. A. Druy, Y. W. Park, A. G. MacDiarmid, A. J. Heeger *J. Polym. Sci., Polym. Lett. Ed.* **1979**, *17*, 779.

28 A. F. Diaz *J. Electrochem. Soc.* **1989**, *123*, 115.

29 R. J. Waltman *Can J. Chem.* **1986**, *64*, 76.

30 a) R. J. Waltman, J. Bargon, A. F. Diaz *J. Phys. Chem.* **1983**, *87*, 1459; b) T. Yamamoto, K. Sanechika, A. Yamamoto *J. Polm. Sci., Poly. Lett. Ed.* **1980**, *18*, 9; c) G. Tourillon, F. Garnier *J. Electochem. Soc.* **1983**, *130*, 2042.

31 G. Tourillon, F. Garnier *J. Electroanal. Chem.* **1982**, *135*, 173.

32 a) A. G. MacDiarmid *Poly. Prep. Am. Chem. Soc. Div. Polym. Chem.* **1984**, *25*, 248; b) E. Genies, C. Tsintavis *J. Electroanal. Chem.* **1985**, *195*, 109; c) T. Kobayashi, H. Yoneyama, H. Tamura *J. Electroanal. Chem.* **1984**, *177*, 281; d) I. Rubenstein, E. Sabatini, J. Rishpan *J. Electroanal. Chem.* **1987**, *134*, 3078.

33 a) D. M. Ivory *J. Chem. Phys*. **1979**, *71*, 1506; b) M. Satoh, K. Kaneto, K. Yoshino *J. Chem. Soc., Chem. Commun.* **1985**, 1629.

34 Y. Chen, C. T. Imrie, J. M. Cooper, A. Glidle, D.G. Morris, K.S. Ryder *Polym. Int.* **1998**, *47*, 43.

35 R. E. Peierls, *Quantum Theory of Solids*, Oxford University Press, Oxford, 2001 (reprint of 1936 original).

36 J. L Bredas, R. R. Chance, R. Silbey *Phys. Rev. Part B.* **1982**, *26(10)*, 5843.

37 B. R. Weinberger, E. Ehrenfreund, A. J. Heeger, A. G. MacDiarmid *J. Chem. Phys.* **1980**, *72*, 4749.

38 A. R. Bishop, D. K. Campbell, K. Fesser *Mol. Cryst. Liq. Cryst.* **1980**, *77*, 253.

39 D. J. Walton *Mater. Des.* **1990**, *11(3)*, 142.

40 G. P. Evans, *Advances in Electrochemical Science and Engineering*, Vol. I, Cambridge Life Science, Cambridge, 1990.

41 a) R. Qian, J. Qiu, *Polym. J.* **1987**, *19*, 157; b) J. Roncali, F. Garnier, M. Lemaire, R. Garreau *Synth. Met.* **1986**, *15*, 323.

42 A. R. Hepburn, J. M. Maud, J. M. Marshall *Met. Mater (Inst. Mater.)* **1991**, *7(12)*, 747.

43 H. Naarmann, *Polymers to the Year 2000 and Beyond* , Wiley, 1993, Chapter 4.

44 P. J. Nigrey, A. G. MacDiarmid, A. J. Heeger *J. Chem. Soc., Chem. Commun.* **1979**, 594.

45 E. M. Genies, G. Bidan, A. F. Diaz *J. Electroanal. Chem.* **1983**, *149*, 101.

46 J. Roncali *Chem. Rev.* **1992**, *92(4)*, 711.

47 J. E. Frommer, R. R. Chance, *Electrically Conducting Polymers: Encyclopaedia of Polymer Science and Engineering*, Vol. V, Wiley, New York, 1986, p 462.

48 R. J. Waltman, J. Bargon *Tetrahedron* **1984**, *40(20)*, 3963.

49 W. A. Goedel, G. Hoeltz, G. Wegner, J. Rosemund, G. Zotti *Polymer* **1993**, *34*, 4341.

50 Y. Chen, W. T. A. Harrison, C. T. Imrie, K. S. Ryder *J. Mater. Chem.* **2002**, *12*, 579.

51 A. F. Diaz, J. Bargon in T. J. Skotheim (Ed.), *Handbook of Conducting Polymers*, Marcel Dekker Inc., New York, 1986.

52 G. B. Street in T. A. Skotheim (Ed.), *Handbook of Conducting Polymers*, Marcel Dekker Inc., New York, 1986.

53 R. Qian in W. R. Salaneck, I. Lundstroem and B. Ranby (Eds.), *Conjugated Polymers and Related Materials*, Oxford University Press, London, 1993, p 161.

54 a) Y. Cao, P. Smith, A. J. Heeger *Synth. Met.* **1992**, *48*, 91; b) A. G. MacDiarmid, A. J. Epstein *Synth. Met.* **1994**, *65*, 103.

55 a) J. Y. Lee, D. Y. Kim, C. Y. Kim *Synth. Met.* **1995**, *74*, 103; b) J. Y. Lee, K. T. Song, S. Y. Kim, Y. C. Kim, D. Y. Kim, C. Y. Kim *Synth. Met.* **1997**, *84*, 137; c) Y. Shen, M. Wan *J. Poly. Sci. A* **1999**, *37*, 1443.

56 J. Ruehe, T. Ezquerra, G. Wegner *Makromol. Chem. Rapid Commun.* **1989**, *10*, 103.

57 A. J. Heeger *Faraday Discuss. Chem. Soc.* **1989**, *88*, 203.

58 a) B. J. S. Johnson, J. H. Wolf, A. S. Zalusky, M. A. Hillmyer *Chem. Mater.* **2004**, *16*, 2909; b) S. I. Yoo, B.-H. Sohn, W.-C. Zin, J. C. Jung *Langmuir* **2004**, *20*, 10734.

59 a) P. Ensel, T. Bein *J. Chem. Soc., Chem. Commun.* **1989**, 1326; b) J. Casper, V. Ramamurthy, D. R. Corbin *J. Am. Chem. Soc.* **1991**, *113*, 600; c) T. J. Pinnavaia, P. L. Hall, S. S. Cady, M. M. Mortland *J. Phys. Chem.* **1974**, *78*, 994; d) Z. Cai, C. R. Martin *J. Am. Chem. Soc.* **1989**, *111*, 4138; e) W. Liang, C. R. Martin *J. Am. Chem. Soc.* **1990**, *112*, 9666: f) C.-G. Wu, T. Bein *Science*, **1994**, *264*, 1757; g) S. Feng, T. Bein *Science* **1994**, *265*, 1839; h) C.-G. Wu, T. Bein *Science*, **1994**, *266*, 1013;

60 a) M. G. Kanatzidis, L. M. Tonge, T. Marks, H. O. Marcy, C. R. Kannewurf *J. Am. Chem. Soc.* **1987**, *109*, 3797. b) L. Wang, J. Schindler, J. Albritton Thomas, C. R. Kannewurf, M. G. Kanatzidis *Chem. Mater.* **1995**, *7*, 1753.

61 a) A.-H. Bae, T. Hatano, M. Numata, M. Takeuchi, S. Shinkai *Macromolecules*, **2005**, *38*, 1609. b) X. Zhang, J. Zhang, R. Wang, T. Zhu, Z. Liu *ChemPhysChem* **2004**, *5*, 998; c) G. Wegner, J. Ruehe *J. Faraday Discuss. Chem. Soc.* **1989**, *88*, 333.

62 a) Y. Yang, J. Liu, M. Wan *Nanotechnology* **2002**, *13*, 771; b) J. Liu, M. Wan *J. Mater. Chem.* **2001**, *11*, 404; c) Y. Yang, M. Wan *J. Mater. Chem.* **2001**, *11*, 2022.

63 a) M. J. Winokur, P. Wamsley, J. Moulton, P. Smith, A. J. Heeger *Macromolecules* **1991**, *24*, 3812; b) D. D. C. Bradley, R. H. Friend, H. Linderberger, S. Roth *Polymer* **1986**, *27*, 1709.

64 a) K. M. McGrath, C. J. Drummond *Coll. Polym. Sci.* **1996**, *274*, 316; b) K. M. McGrath *Coll. Polym. Sci.* **1996**, *274*, 399; c) K. M. McGrath *Coll. Polym. Sci.* **1996**, *274*, 499; d) K. M. McGrath, C. J. Drummond *Colloid Polym. Sci.* **1996**, *274*, 612.

65 a) Y. Chen, C. T. Imrie, K. S. Ryder *J. Mater. Chem.* **2001**, 990; b) Y. Chen, C. T. Imrie, K. S. Ryder *J. Mater. Sci. Lett.* **2002**, *231*, 595.

66 a) P. Ibison, P. J. S. Foot, J. W. Brown *Synth. Met.* **1996**, *76*, 297; b) H. Hasegawa, M. Kijima, H. Shirakawa *Synth. Met.* **1997**, *84*, 177; c) M. Kijima, H. Hasegawa, H. Shirakawa *J. Poly. Sci. A* **1998**, *36*, 2691; d) F. Vincentini, J. Barrouillet, R. Laversanne, M. Mauzac, F. Bibonne and J. P. Parneix *Liquid Crystals* **1995**, *19(2)*, 235; e) P. J. Langley, F. J. Davis, G. R. Mitchell *J. Chem. Soc., Perkin Trans.* **1997**, *2*, 2229; f) B. Faye, M. Mauzac, J. P. Parneix *Synth. Met.* **1999**, *99*, 115; g) P. J. Langley, F. J. Davis, G. R. Mitchell *Mol. Cryst. Liq. Cryst.* **1993**, *234*, 765; h) D. Melamed, C. Nuckols, M. A. Fox *Tet. Lett.* **1994**, *35*, 8329; i) C. Jego, E. Dupart, P. A. Albany, C. Mingotand *Thin Solid Films* **1998**, *329*, 1; j) M. Kijima, S. Abe, H. Shirakawa *Synth. Met.* **1999**, *101*, 61.

67 K. Nakaya, K. Funabiki, K. Shibata, M. Matsui *Bull. Chem. Soc. Jpn.* **2001**, *74*, 549.

68 a) F. Wuerthner, Z. Chen, F. J. M. Hoeben, P. Osswald, C.-C. You, P. Jonkheijm, J. v. Herrikhuyzen, A. P. H. J. Schenning, P. P. A. M. van der Schoot, E. W. Meijer, E. H. A. Beckers, S. C. J. Meskers, R. A. J. Janssen *J. Am. Chem. Soc.* **2004**, *126*, 10611. b) J. v. Herrikhuyzen, A. Syamakumari, A. P. H. J. Schenning, E. W. Meijer *J. Am. Chem. Soc.* **2004**, *126*, 10021.

69 A. P. H. J. Schenning, J. v. Herrikhuyzen, P. Jonkheijm, Z. Chen, F. Wuerthner, E. W. Meijer *J. Am. Chem. Soc.* **2002**, *124*, 10252.

70 R. Allmann, *Roentgenpulverdiffraktometrie*, Verlag Sven von Loga, Koeln, 1994.

71 W. L. Bragg *Nature* **1912**, *90*, 410.

72 Literature on circular dichroism spectroscopy and its applications: a) A. Rodger, B. Norden, *Circular Dichroism and Linear Dichroism*, Oxford University Press, Oxford, 1997; b) N. Greenfield, G. D. Fasman *Biochemistry* **1996**, *8*, 4108; c) W. C. Johnson *Proteins: Structure, Function, and Genetics* **1990**, *7*, 205.

73 a) E. Collett, *Polarized Light: Fundamentals and Applications*, Marcel Dekker Inc., New York, 1993. b) R. Stoiber, S. Morse, *Crystal Identification with the Polarizing Microscope*, Chapman and Hall, New York, 1994.

74 L. Coche-Guerente, A. Deronzier, B. Galland, J.-C. Moutet, P. Labbé, G. Reverdy, Y. Chevalier, J. Amhrar *Langmuir* **1994**, *10*, 602.

75 I. Berlot, P. Labbé, J.-C. Moutet, M. Turmine *J. Electronanal. Chemistry* **1997**, *431*, 57.

76 I. Berlot, Y. Chevalier, P. Labbé, J.-C. Moutet *Langmuir* **2001**, *17*, 2639.

77 C. Tanford *J. Phys. Chem.* **1972**, *176*, 21.

78 D. Fennel Evans, H. Wennerström, *The Colloidal Domain Where Physics, Chemistry, Biology, and Technology Meet*, Wiley, New York, 1999, Chapter 2.4.

79 T. Sasaki, M. Hattori, J. Sasaki, K. Nukina *Bull. Chem. Soc. Jpn.* **1975**, *48*,1397.

80 E. A. Simister, R. K. Thomas *J. Phys. Chem.* **1992**, *96*, 1383.

81 K. Kalyanasundaram, J. K. Thomas *J. Am. Chem. Soc.* **1997**, *99*, 2039.

82 K. Bijma, J. B. F. N. Engberts *Langmuir* **1997**, *13*, 4843.

83 K. Bijma, E. Rank, J. B. F. N. Engberts *J. Colloid Interface Sci.* **1998**, *205*, 245.

84 G. Friedel, *Colloid Chemistry*, Vol I, The Chemical Catalog Co., New York, 1926, p 102-125.

85 F. B. Rosevear *J. Am. Oil. Chem. Soc.* **1954**, *31*, 628.

86 C. Hall C, G. J. T. Tiddy *Surfactants in solution*, Vol. VIII, Plenum Press, New York, 1988, p 9-23.

87 Y. Bouligand in D. Demus, J. Goodby, G. W. Gray, H.-W. Spiess, V. Vill (Eds.), *Handbook of Liquid Crystals,* Vol I, Wiley, Weinheim, 1998, p 409-410.

88 P. Becher, *Emulsions: Theory and Practice,* American Chemical Society*, 2001, Chapter 1 and ref. therein.

89 P. Ekwall, *Advances in Liquid Crystals*, Vol. I, Academic Press, New York, 1975, p 1-142.

90 M. J. Schick (Ed.), *Nonionic Surfactants, Physical Chemistry*, Marcel Dekker Inc., New York, 1987.

91 J. P Conroy, C. Hall, C. A. Leng, K. Rendall, G. J. T. Tiddy, J. Walsh, G. Lindblom *Prog. Colloid. Polym. Sci*. **1990**, *82*, 253.

92 K. W. Herrmann, J. G. Brushmiller, W. L. Courchene *J. Phys. Chem*. **1966**, *70*, 2909.

93 a) R. G. Laughlin in G. H. Brown (Ed.), *Advances in Liquid Crystals*, Vol. III, Academic Press, New York, 1978, p 42-98. b) R. G. Laughlin in G. H. Brown (Ed.), *Advances in Liquid Crystals*, Vol. III, Academic Press, New York, 1978, p 99-148. c) R. G. Laughlin, *The Aqueous Phase Behaviour of Surfactants*, Academic Press, London, 1994.

94 S. A Buckingham, C. J. Garvey, G. G. Warr *J. Phys. Chem.* **1993**, *97*, 10236.

95 P. G. Nilsson, W. F. Pacynko, G. J. T. Tiddy *Curr. Opin. Colloid Interface Sci.* **2004**, *9*, 117.

96 B. Smarsly, C. G. Göltner, M. Antonietti, W. Ruland, E. Hoinkis *J. Phys. Chem.* **2001**, *105*, 831.

97 D. Pressner, C. Goeltner, H.-W. Spiess, K. Muellen *Ber. Bunsen-Ges. Phys. Chem.* **1993**, *97*, 1362.

98 C. A. Hunter, J. K. M. Sanders *J. Am. Chem. Soc.* **1990**, *112*, 5525.

99 a) R. G. Snyder, H. L. Strauss, C. A. Elliger *J. Phys. Chem.* **1982**, *86*, 5145. b) N. Nakashima, N. Yamada, T. Kunitake, J. Umemura, T. Takenaka *J. Phys. Chem.* **1986**, *90*, 3374. c) R. G. Nuzzo, F. A. Fusco, D. L. Allara *J. Am. Chem. Soc.* **1987**, *109*, 2358.

100 R. M. Silverstein, F. X. Webster, *Spectrometric Identification of Organic Compounds*, 6th Ed., Wiley, New York, 1998.

101 K. J. Wynne, G. B. Street *Macromolecules* **1985**, *18*, 2361.

102 D. Mecerreyes, R. Stevens, C. Nguyen, J. A. Pomposo, M. Bengoetxea, H. Grande *Synth. Met.* **2002**, *126*, 171.

103 a) B. Tian, G. Zerbi *J.Chem. Phys.* **1990**, *92*, 3886. b) B. Tian, G. Zerbi *J.Chem. Phys.* **1990**, *92*, 3892.

104 N. Costantini, S. Capacciolo, M. Geppi, G. Ruggeri *Poly. Adv. Technol.* **2000**, *11*, 27.

105 a) T. Iyoda, M. Ando, T. Kaneko, A. Ohtani, T. Shimidzu, K. Honda *Langmuir* **1987**, *3*, 1169. b) T. Iyoda, M. Ando, T. Kaneko, A. Ohtani, T. Shimidzu, K. Honda *Tet. Lett.* **1986**, *27*, 5633.

106 a) A. F. Diaz, J. Castillo, K. K. Kanazawa, J. A. Logan, M. Salmon, O. Fajardo *J. Electroanal. Chem.* **1982**, *133*, 233. b) S. Cosnier, A. Deronzier, J.-C. Moutet *J. Mol. Catalysis*, **1988**, *45*, 381.

107 I. Berlot, P. Labbé, J.-C. Moutet *Langmuir* **2000**, *16*, 5814.

108 G. E. Barr, C. N. Sayre, D. M. Connor, D. M. Collared *Langmuir* **1996**, *12*, 1395.

109 a) X.-G. Li, R.-F. Chen, M.-R. Huang, M.-F. Zhu, Q. Chen *J. Poly. Sci. A* **2004**, *42*, 2073. b) E. M. Peters, J. D. van Dyke *J. Poly. Sci. A* **1992**, *30*, 1891. c) G. Koeckelberghs, L. De Cremer, W. Vanormelingen, T. Verbiest, A. Persoons, C. Samyn *Macromolecules*, **2005**, *38*,4545.

110 a) G. Zotti, S. Zecchin, G. Schiavon, B. Vercelli, A. Berlin, E. Dalcananle, L. 'Bert' Groenendaal *Chem. Mater.* **2003**, *15*, 4642. b) D. M. Collard, M. A. Fox *J. Am. Chem. Soc.* **1991**, *113*, 9414.

111 a) R. Gvishi, R. Reisfeld, Z. Burshtein *Chem. Phys. Lett.* **1993**, *213*, 338. b) F. Wurthner, C. Thalacker, A. Sautter, W. Schartl, W. Ibach, O. Hollricher *Chem. Eur. J.* **2000**, *6*, 3871.

112 M. Kasha, H. R. Rawls, M. A. El-Bayoumi *Pure Appl. Chem.* **1965**, *11*, 371.

113 J. Mizuguchi, K. Tojo *J. Phys. Chem. B* **2002**, *106*, 767.

114 B. M. W. Langeveld-Voss, D. Beljonne, Z. Shuai, R. A. J. Janssen, S. C. J. Meskers, E. W. Meijer, J.-L. Brédas *Adv. Mater.* **1998**, *10*, 1343.

115 N. Harada, K. Nakanishi, *Circular Dichroism Spectroscopy*, Oxford University Press, Oxford, 1983.

116 (a) F. D. Lewis, X. Liu, Y. Wu, X. Zuo *J. Am. Chem. Soc.* **2003**, *125*, 12729. (b) F. D. Lewis, Y. Wu, L. Zhang, X. Zuo, R. T. Hayes, M. R. Wasielewski *J. Am. Chem Soc.* **2004**, *126*, 8206. (c) Y. Zheng, H. Long, G. C. Schatz, F. D. Lewis *Chem. Commun.* **2005**, 4795.

117 J. J. L. M. Cornelissen, J. J. J. M. Donners, R. de Gelder, W. S. Graswinckel, G. A. Metselaar, A. E. Rowan, N. A. J. M. Sommerdijk, R. J. M. Nolte *Science* **2001**, *293*, 676.

118 a) A. Mülller *Proc. R. SOC. London, Ser. A* **1932**, *138*, 514 b) For a more recent reference: R. Montenegro, K. Landfester *Langmuir* **2003**, *19*, 5996.

119 Polarized optical microscopy did not yield any textures typical for chiral phases. Further efforts to identify lyotropic liquid-crystalline phases for complexes **13** and **14** in THF, CHCl$_3$, DMF, DMSO and NMP using a penetration scan technique were met without success.

120 Cerius2, version 4.6, Accelrys Inc., 2001.

121 a) E. H. A. Beckers, S. C. J. Meskers, A. P. H. J. Schenning, Z. Chen, F. Würthner, R. A. J. Janssen *J. Phys. Chem. A* **2004**, *108*, 6933. b) A. Herrmann, T. Weil, V. Sinigersky, U.-M. Wiesler, T. Vosch, J. Hofkens, F. C. De Schryver, K. Müllen *Chem. Eur. J.* **2001**, *7*, 4844.

122 K. Schwetlick *et al. Organikum*, Wiley, Weinheim, **1999,** p 606.